Effect of Thickness and Ply Orientation on the Flexural Bending Behaviour of Thick Composite Laminates

Jeffrey Fortin-Simpson

A Thesis

In

The Department

Of

Mechanical and Industrial Engineering

Presented in Partial Fulfillment of the Requirements

For the Degree of

Master of Applied Science in Mechanical Engineering at

Concordia University

Montreal, Quebec, Canada

June 2019

CONCORDIA UNIVERSITY

School of Graduate Studies

This is to certify that the thesis prepared

By: Jeffrey Fortin-Simpson

Entitled: Effect of Thickness and Ply Orientation on the Flexural Bending Behaviour of Thick Composite Laminates

and submitted in partial fulfillment of the requirements for the degree of

Master of Applied Science in Mechanical Engineering

complies with the regulations of the University and meets the accepted standards with respect to originality and quality.

Signed by the final Examining Committee:

_____ Chair

Dr. Alex De Visscher

_____ Examiner

Dr. Farjad Shadmehri

_____ Examiner

Dr. Lan Lin

_____ Supervisor

Dr. Suong Van Hoa

_____ Co-Supervisor

Dr. Wen-Fang Xie

Approved by _____

Dr. Martin Pugh, Chair of Department

_____

Dr. Amir Asif, Dean of Gina Cody School of Engineering and Computer Science

Date: _____

ABSTRACT

The growing trend of fibre reinforced composite laminates in highly loaded structural applications has created a need for better analytical tools to provide quick estimates of predicted laminate performance, faster computational tools for more detailed laminate analysis, and more experimental data for validation of higher order theories. The production of experimental data requires significant capital investment. As such, the majority of research being conducted is focused on developing higher order theories and reducing computational effort to be able to more accurately simulate composite laminates in various load cases. However, due to the lack of available experimental data, the theoretical research being conducted is most often validated against the 3D elasticity theory, which itself is very computationally intensive, albeit highly accurate. One example of a highly loaded composite structure with a thick cross-section is a helicopter's main rotor yoke. Industry experience has determined that the thick section of such a laminate is the most critical, especially around the area of load introduction due to a bolted joint connection. This study aims to provide reliable experimental data against which a higher-order monodimensional beam theory is compared, and that can be used to validate other higher order theories. Rectangular laminates of 20, 40, 60, and 80 unidirectional layers along with 80 cross-ply layers are tested in quasi-static cantilever bending at 5 mm/min, where the fixed end of the laminate is clamped between steel plates and the loaded end is clamped between the cylindrical faces a cantilever loading fixture. Laminates of 80 unidirectional layers are also tested in cantilever bending where the loaded end is also clamped between steel plates to represent a bolted connection at both ends of the specimen. Digital image correlation and strain gauges were used to collect surface strain measurements which were used to validate a fully parametric ANSYS model that could predict failure based on Hashin failure criteria. The train data showed that digital image correlation is a valid technique for full-field surface strain measurement up to very high displacement and strain levels. The load-displacement data was compared to higher-order monodimensional beam theory calculations and showed the limitations of this theory as specimen thickness increased, as well as the accuracy it can provide for thinner laminates, even when including secondary bonded components such as buffer pads. A simplified

method for using the monodimensional beam theory is presented for the quick calculation of the shear correction coefficient of a $[0/90]_{\Omega s}$ laminate, where Ω can be any integer. The failure displacements of each specimen configuration are charted against laminate thickness to illustrate the size effect, which is the principle of decreasing component strength with increasing thickness, as it relates to composite plates in bending.

ACKNOWLEDGEMENTS

This work is part of the framework of the CRIAQ COMP 509-INTL project, entitled “Bell flex beam flappability optimization”. This project is funded and supported by Bell Helicopter Textron Canada Ltd., the Natural Sciences and Engineering Research Council of Canada (NSERC), and the Consortium for Research and Innovation in Aerospace in Quebec (CRIAQ). It is an international collaboration work with the Indian Institute of Science (IISc). I would like to acknowledge Bell Helicopter for their material support and technical instructions.

I would also like to especially thank Dr. Hoa for his encouragement and support throughout this project. His guidance has been invaluable to this experience and has helped make it a success. It is an honour to work alongside someone of such knowledge and expertise. I would also like to thank my fellow students involved in this project. They have been a great help, providing advice and assistance whenever possible. Particularly Wen Xiong and Alireza Gorjipoor who’s assistance with manufacturing samples and planning test procedures was instrumental in making this project a success.

My gratitude also goes out to Dr. Daniel Rosca and Mr. Heng Wang, along with the students in our Concordia Centre for Composites research group. They have been a source of great support, assistance, and friendship.

Last, but not least, my deepest appreciation goes to my parents for supporting me through all my life’s decisions and always encouraging me to do what is right and meaningful. Their endless love and support have pushed and guided me through this incredible journey as a graduate student.

TABLE OF CONTENTS

LIST OF FIGURES

LIST OF TABLES

LIST OF EQUATIONS

CHAPTER 1 INTRODUCTION AND LITERATURE REVIEW

Fiber reinforced plastic composite (FRPC) parts are continually gaining popularity in various industries due to their highly desirable characteristics of high specific strength and moduli, improved environmental resistance, and stable dynamic performance. Particularly in aerospace, where weight is always a dominating point of consideration, the appeal of a material that can reduce the weight of a structural part without the expense of performance, is easily understood. As such, there is much research being performed to properly understand the behaviour and phenomena associated with FRPCs to better predict the stresses, strains, and failure resulting from expected load cases. Today, much of the theory surrounding the analysis of FRPCs applies to thin laminates. For the purposes of this thesis, a thin laminate corresponds to one with a thickness less than 6 mm. The behaviour of thin laminates is very well understood and can often be predicted analytically. The same does not apply to thick laminates due to the increasing effect of interlaminar shear properties with increasing thickness. This has limited our ability to properly predict and model the behaviour of thick laminates. The phenomena associated with increased thickness of FRPCs also results in the necessity for added considerations during manufacturing.

1.1 Manufacturing of Thick Composite Laminates

The growing use of composite materials in structural applications that require parts with a thickness greater than 6 mm is creating a need to properly understand how existing composite theory must be modified to accommodate the increased importance of the effects related to greater thickness. As it pertains to thermosetting composites, the increased thickness renders the manufacturing of laminates more difficult, most notably the autoclave curing process, which is the most common composite manufacturing technique in aerospace. The effect of increased thickness on the temperature distribution must be accounted for. The heat generation and, more importantly, dissipation in thick laminates is different than that of thin laminates, requiring significant modification to the manufacturer's recommended cure cycles. Failure to do so results in matrix degradation, nonuniform cure and consolidation, and residual stresses [1].

Throughout his experience working with autoclave curable composite laminates, Stringer [2] made several advancements in autoclave processing steps that result in minimum void content and high fibre volume fractions. It is well known that voids reduce resin dominated properties, such as compression and interlaminar shear strengths. He found that a void content above 2.5% can reduce the interlaminar shear strength by as much as 45%. He surmised that voids appear due to three factors: retained solvent and entrapped air, which are inherent to the layup process and can usually be mitigated by proper degassing or vacuum debulking, and excess bleeding of the resin during curing. High viscosity resins were created to address this third factor, but they require careful control of the gelling process through timely application of pressure and temperature. The addition of a dwell period at a temperature far below the final cure temperature can increase the minimum viscosity of the resin before full pressure is applied. The principles employed by Stringer were applied to thin laminates. However, their consideration becomes even more important with thick laminates. Thick laminates also require additional consideration due to the propensity for exothermal spikes. Due to the low thermal conductivity of composite materials, a substantial amount of temperature lag and thermal overshoot are often seen in the autoclave curing of thick laminates. If the temperature lag is not accounted for, consolidation does not occur simultaneously throughout the volume of the part, giving rise to a nonuniform degree of cure.

With regards to void growth, Kardos *et al*. [3] reported that voids tend to grow during cure while the resin is at low viscosity and the pressure inside the void exceeds that of the resin. Therefore, controlling resin pressure, vacuum pressure, and resin flow are essential to mitigating void formation and growth. If the resin pressure is high enough, the moisture or gas entrapped in the resin cannot form voids of significant size. Additionally, if the resin pressure is high enough while the resin is at low viscosity, some of the existing voids may be squeezed out of the laminate [1]. However, if too much resin flows out of the laminate, the fibre network can become load bearing and the resin pressure decreases, increasing the possibility of void formation and growth. Koushyar *et al*. [4] studied the effect of various autoclave parameters, including vacuum application, and found that the void content of carbon/epoxy laminates increased significantly when the vacuum was held throughout the entire cure cycle as compared to venting

the vacuum at the onset of consolidation pressure. This increase was more notable at the centre of the laminate. They concluded that, if the vacuum is maintained at elevated curing temperatures while the resin is at low viscosity, excessive bleeding of the resin may occur because the combined effect of autoclave pressure and full vacuum squeezes the low viscosity resin towards the vacuum inlet. This leads to the autoclave pressure being supported by the fibre bed, as described in [1]. Additionally, at this stage, the volatiles in the resin boil, pushing more resin away from the fibres and creating voids. As such, it is now common practice to vent the vacuum to atmosphere when consolidation pressure and temperature are applied.

Bogetti and Gillespie [5] investigated the two-dimensional cure simulation of thick thermosetting composites. They employed an incremental transient finite difference solution scheme to solve the boundary conditions and governing equations. They introduced a heat generation term to account for the heat released during curing and formulated the boundary conditions such that an arbitrary temperature boundary condition could be enforced. They were able to accurately predict complex gradients in temperature and degree of cure, as compared to through-thickness experimental measurements, and demonstrated the influence of the tool on the curing process. The spatial gradients in degree of cure, which are responsible for introducing warpage and residual stress, were shown to be strongly dependent on part geometry, thermal anisotropy, cure kinetics, and temperature cure cycle.

Young [6] carried out an investigation on the effect of compaction forces and cure cycle on the degree of consolidation. Proper control of the applied temperature and consolidation pressure is necessary to allow the resin to flow before it gels. This resin flow is critical in achieving proper fibre volume fraction and removing excess voids. Their simulation found that the compaction pressure was the dominant factor in the final degree of consolidation, as it was necessary to achieve full through-thickness compaction. The cure cycle temperature was only capable of controlling the thermal response and resin reaction of the laminate, it had no effect on the proper compaction of the plies. It was found to be simple enough to modify the cure cycle to mitigate temperature overshoot, but proper control of the compaction pressure was required to provide an acceptable degree of consolidation. Since the prevailing consensus in the aerospace

industry is to employ a zero-bleed curing process for thermoset composites, and certain laminate characteristics are determined by resin flow, it is important to ensure uniform resin pressure distribution during the curing process. To this aim, Xin *et al*. [7] developed an online resin pressure measuring system. Their experiments proved that resin pressure is uniformly distributed in-plane and through-thickness during zero-bleeding autoclave curing process. They also showed that the relationship between applied pressure, resin pressure, and pressure carried by the fiber bed conforms to the spring and piston model, and the resin pressure is independent of the vacuum condition. A drop in resin pressure is caused by resin flow, which itself may be exacerbated by constant vacuum application. Hojjati and Hoa [8] developed model laws based on dimensionless parameters for the curing of thermosetting composites. They used these laws to successfully predict the temperature and degree of cure distributions of a thick composite laminate.

By using finite difference analysis and experiments, Kim and Lee [9] developed an autoclave curing cycle with cooling and reheating steps that successfully mitigated temperature overshoot. Oh and Lee [10] furthered this by using a three dimensional finite element analysis (FEA) of 20 mm thick glass/epoxy laminates, while including the tool and vacuum bag assembly, to determine an optimized cure cycle with cooling and reheating steps. Permeability along the fibre direction can be as much as one order of magnitude greater than that in the transverse direction. As such, they found that a one-dimensional flow simulation assumed a much longer time to complete consolidation. This proved the value of a three-dimensional model. Olivier and Cavarero [11] demonstrated the importance of an optimized cure cycle for thick laminates. They compared the tensile performance of thin laminates with that of thick laminates that were cured using the manufacturer's recommended cure cycle. They then compared these results to thick laminates cured using an optimized cure cycle that resulted in characteristics identical to thin laminates.

Much of the research surrounding the cure analysis of thermosetting composites involved the use of simulations to help determine acceptable cure cycles. However, the process of optimizing these cure cycles using numerical simulation was very computationally intensive. Towards this effort of reducing simulation time, Rai and Pitchumani [12] presented the use of advanced artificial neural networks (ANNs) trained using experimentally validated physical models as a substitute for rigorous numerical simulations.

This was shown to increase computational speed by several orders of magnitude. Zhang and Friedrich [13] provided a detailed review of the various applications of ANNs with regards to polymer composites. ANNs are inspired by the biological nervous system. Similarly to their biological counterpart, the success of an ANN is determined by the interconnection of artificial neurons. As it pertains to polymer composites, sufficient experimental results are required to properly train an ANN. Once the ANN has learned to solve the material problems, new data can be predicted without the need for performing many long experiments. ANNs also allow for faster systematic parameter studies, which are required for optimization.

To manufacture high quality thick composite parts, such as helicopter rotor yokes and flex beams, cavity molding has become a popular manufacturing method in the aerospace industry. This process involves the application of heat and pressure via a platen press to rigid tooling, which entices the part within to cure into the shape of the cavity. To this regard, Bheemreddy *et al*. [14] developed two-dimensional cure and flow models for glass/epoxy prepreg to simulate resin flow, heat transfer, consolidation and curing during the cavity molding process. They were able to accurately calculate the temperature distribution and degree of cure of a flex beam part. They noticed that the centre of the thick cross-section held heat for a longer period of time, which could embrittle the resin and result in uneven cure. Bheemreddy *et al*. [15] further developed this study by coupling a three-dimensional thermo-mechanical model with an ANN based procedure for extracting the cure kinetic parameters from differential scanning calorimetry (DSC) tests, in order to optimize the cure cycle for cavity molded composite flex-beams.

Ruiz and Trochu [16] predicted the residual stresses and resulting warpage of thick resin transfer molded (RTM) parts by numerical analysis. They presented a reaction kinetics model of the resin, then applied a linear model to predict volume changes. They used a finite difference model to simulate the effects of thermal and rheological changes during processing and used classical laminate theory (CLT) to calculate the internal stresses. Finally, they applied a thermal optimization algorithm to demonstrate the advantages of transient heating and cooling to minimize residual stresses and avoid thermal degradation. Mamani and Hoa [17] developed a finite difference formulation of the one-dimensional transient heat transfer problem, including internal heat generation, to simulate the heat transfer during autoclave curing of vacuum-bagged

thick glass/epoxy laminates. They were able to accurately predict the temperature profiles as compared to experimental results. These temperature gradients give rise to non-uniform curing through the thickness of the laminate and consequently lead to process-induced residual stresses that should be accounted for as initial conditions to a finite element stress analysis model.

1.2 Quasi-Static Testing of Thick Composite Laminates

The effects of interlaminar shear stress due to increased thickness of FRPCs under a bending load have been known for some time. However, physical testing of composite samples can be prohibitively expensive and time consuming. As such, the focus of much of the research surrounding the bending behaviour of thick composites has been on developing higher-order shear deformation theories and three-dimensional modeling techniques. Reddy and Chao [18] first proposed a shear deformable theory accounting for the transverse shear and large rotations of thick rectangular composite plates. They compared their numerical results with other approximate results available in literature. Kapania and Raciti [19] performed a detailed literature review of the advances in shear deformable theory for laminated plates and beams up to 1989. More recently, Kant and Swanminathan [20], and Mittelstedt and Becker [21], performed comprehensive literature surveys of the research done towards more accurately calculating interlaminar stresses with a focus on numerical methods. Plagianakos and Saravanos [22] proposed a higher-order layerwise theory for predicting interlaminar stresses in thick composite plates and sandwich structures. Their theory employs kinematic assumptions that satisfy a priori the in-plane displacement field continuity through the thickness of the laminate. Although much progress has been made towards reducing computational efforts in modeling the behaviour of thick composite laminates, many of the references mentioned in this paragraph lack experimental verification, and instead, compare their results to the computationally intensive, albeit widely accepted as highly accurate, three-dimensional elasticity solution provided by Whitney and Pagano [23], which is often cited as a benchmark reference for thick composite modeling.

The versatility of composites toward the tailoring of part properties for specific requirements, such as strength, stiffness, or dynamic characteristics has led to increasing use of composites in the manufacturing of highly loaded structural aerospace components. One such component is the Bell Helicopter M407 main rotor yoke, a four-bladed single piece glass/epoxy structure, which is the main load bearing part of the main rotor hub, shown in Figure 1.1, with the yoke identified. Each of the four blades of the yoke starts with a thick section near the motor shaft for load introduction, which tapers into a thinner section to allow flapping of the blades, finally increasing back to a thick section to fasten to the rotor blades. Lalonde [24] performed a comprehensive analysis on the delamination failure of this main rotor yoke. She investigated the static and fatigue response to beam-wise bending loads and used experimental data from tapered specimens cut from an actual yoke to validate a finite element model of a tapered laminate. The model was able to predict the location of initial static failure, which corresponds to the interlaminar shear stress concentration as predicted by the stress analysis, however, the experimental failure load was found to be about 45% higher than the model prediction. The primary mode of failure, from fatigue experiments, was delamination driven by interlaminar shear. It is also known, from industry experience, that the damage created by load introduction at the thick section is more critical than the damage occurring in the tapered section. As such, this study is focused on thick section composite plates of uniform thickness with bolted join connections. As part of this project, the fatigue behaviour of thick composite laminates is investigated by W. Xiong in [25].

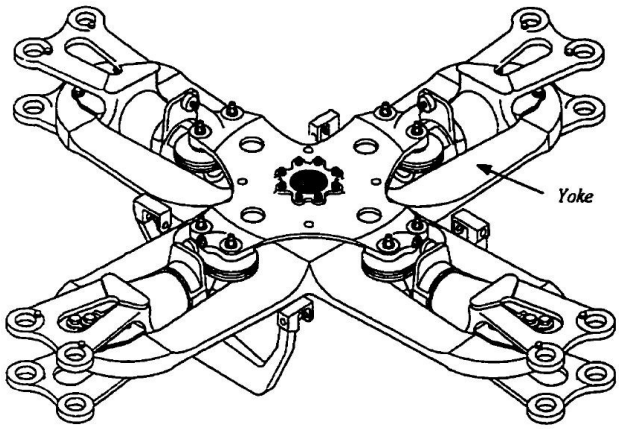

Figure 1.1: Bell Helicopter M407 main rotor hub [24]

1.3 Theoretical Deflection of a Cantilever Composite Beam

It has long been theorized [26] that there exists a size effect when it comes to composites, meaning that strength properties tend to decrease with increasing specimen size. However, a review of available literature [27] on the size effect of composites shows that much of the research is inconclusive and sometimes contradictory, often with a great deal of scatter in experimental results. Wisnom [28] discussed the extent of size effect relative to the fundamental failure mechanisms of fibre tension, fibre compression, matrix dominated transverse tension and shear. A size effect was found for all failure mechanisms, with matrix dominated failures modes exhibiting the greatest effect.

When it comes to composite beams in flexure, this size effect is characterized by the increase in dominance of the interlaminar shear properties. In theory, to compensate for this increased influence from interlaminar shear properties, classical laminate theory for a composite beam in flexure is extended to include a shear correction factor in the analytical expression relating load and deflection [18]. Let us assume a beam of width *b* and thickness *H*, with one end clamped, and the other end free, as shown in Figure 1.2.

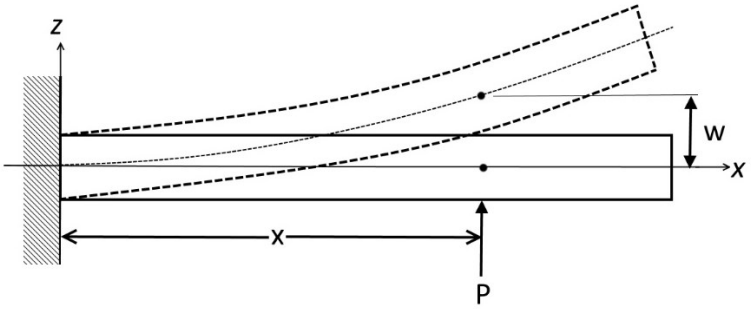

Figure 1.2: Schematic of a cantilever beam

The *X*-axis is along the midplane, the *Z*-axis upwards, and the *Y*-axis going into the page. If a load per unit width of magnitude *P* is applied at a distance *x* from the clamped end, then according to classical beam theory as explained by Reddy [29], the transverse deflection of the midplane of the beam, w_c, at the point of load application, can be written as:

$$w_C = \frac{Pbx^3}{3E_x I_y} \tag{1.1}$$

Equation 1.1: Transverse deflection of a cantilever beam, as per classical beam theory [29]

where E_x is the longitudinal stiffness of the laminate in the X-direction, and I_y is the second moment area of the beam cross-section about the Y-axis. When first-order shear deformation theory is applied to the equation for transverse deflection of a beam, as per Timoshenko beam theory, a second term is added to account for the effect of shear, which introduces a shear correction coefficient, k:

$$w_T = \frac{Pbx^3}{3E_x I_y} + k\frac{Pbx}{G_{xz}bH} \qquad 1.2$$

Equation 1.2: Transverse deflection of a cantilever beam including shear factor, as per Timoshenko beam theory [29]

where G_{xz} is the laminate shear modulus in the XZ-plane. For a homogenous beam of constant rectangular cross-section, such as the one defined in Figure 1.2, the shear correction coefficient is defined as the ratio of the strain energy, as calculated by first order shear deformation theory (FSDT), divided by that as calculated by 3D elasticity theory. This results in a shear correction coefficient $k = 6/5 = 1.2$.

For non-homogenous beams, such as a cross-ply symmetric laminate, the evaluation of k is more complex. As an extension to first order shear deformation theory, Gay *et al.* [30] presented a monodimensional approach to analyzing composite beams in flexure, part of which involves the definition of a warping function and, subsequently, calculation of the shear correction coefficient, which will be discussed here. In this theory, D symbolizes the domain occupied by the cross-section in the YZ-plane, which is symmetric about the XY-plane. The external frontier is denoted as ∂D. The internal interface which limits two contiguous phases i and j, is denoted by l_{ij}. The area of phase i is denoted as S_i, and its longitudinal and shear moduli of elasticity are denoted as E_i and G_i, respectively. Figure 1.3 shows such a cross-section, for which the equivalent stiffnesses are described as in Equation 1.3.

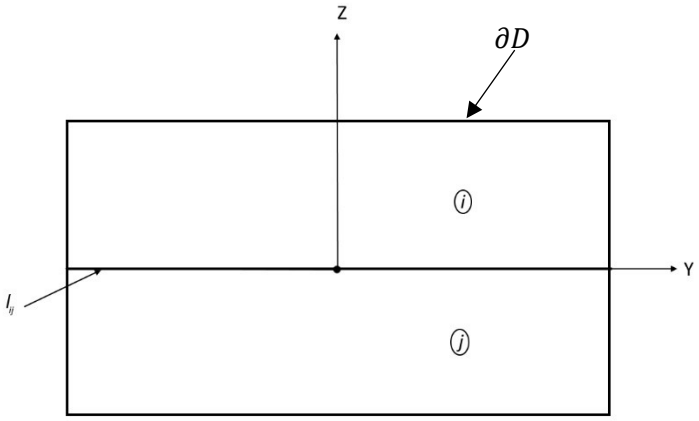

Figure 1.3: Arbitrary rectangular cross-section of a composite beam

$$\langle GS \rangle = \int_D G_i dS = \sum_i G_i S_i \quad \text{(a)}$$

$$\langle EI_y \rangle = \int_D E_i z^2 dS = \sum_i E_i I_{yi} \quad \text{(b)} \qquad 1.3$$

Equation 1.3: Equivalent stiffnesses of a composite beam [30]

A longitudinal warping function, g_o, is introduced such that it is the solution to the problem:

$$\begin{cases} \nabla^2 \mathrm{g}_o = -\dfrac{E_i}{G_i}\dfrac{\langle GS \rangle}{\langle EI_y \rangle} \times z \text{ in the domain } D \\ \dfrac{\partial \mathrm{g}_o}{\partial n} = 0 \text{ on the boundary } \partial D \end{cases} \qquad 1.4$$

Equation 1.4: Problem for which the longitudinal warping function is the solution

It is assumed that the warping function does not vary with *y*. Once obtained, the longitudinal warping function is used to determine the shear correction coefficient using:

$$k = \frac{1}{\langle EI_y \rangle} \int_D E_i \mathrm{g}_o z dS \qquad 1.5$$

Equation 1.5: Shear correction coefficient

1.3.1 Equivalent Stiffness of a $[0/90]_{\Omega S}$ Laminate

The derivation of the simplified monodimensional beam theory (MBT) from [30] that will be presented in sections 1.3.1 to 1.3.3 can be found in APPENDIX A. For a composite beam, such as the one in Figure 1.2, if we assume that it is composed of plies of equal thickness, *h*, and has a layup sequence in

the form $[0/90]_{\Omega S}$, where Ω can be any integer, resulting in a total number of plies, $N = 4\Omega$, then the equivalent stiffnesses can be reduced to polynomial form. Since the beam consists of alternating plies of 0° and 90°, the material properties of interest are E_1, E_2, and G_{12} of the lamina. First, understanding that each layer has the same shear stiffness, G_{12}, and cross-sectional area, $S_i = bh$, the summation from Equation 1.3a can be expanded as follows:

$$\langle GS \rangle = \sum_{i}^{N} G_i S_i = G_{12}S_1 + G_{12}S_2 \ldots + G_{12}S_{N-1} + G_{12}S_N = NbhG_{12} \tag{1.6}$$

Equation 1.6: Equivalent shear stiffness of a symmetric cross-ply laminate

The reduction of the equivalent longitudinal stiffness to polynomial form is a little more involved and requires some understanding of how I_{yi} is calculated for symmetric plies. For every ply i, it's second moment area, I_{yi}, can added to the second moment area of the symmetric ply, $I_{y(N-i+1)}$, to make the simplified expression seen in Equation 1.7, where I_i is the combined second moment area of two symmetric plies.

$$I_{yi} + I_{y(N-i+1)} = I_i = \frac{bh^3}{12}[(N - 2i + 2)^3 - (N - 2i)^3], \qquad 1 \leq i \leq \frac{N}{2} \tag{1.7}$$

Equation 1.7: Combined second moment area of two symmetric plies

Where $i = 1$ corresponds to the top ply, and $i = N$ corresponds to the bottom ply of the laminate. Now, if we expand the summation of Equation 1.3b while understanding and applying Equation 1.7, we get:

$$\langle EI_y \rangle = \sum_{i} E_i I_{yi} = E_1 I_{y1} + E_2 I_{y2} + E_1 I_{y3} \ldots + E_2 I_{y(N-1)} + E_1 I_{yN}$$

$$= E_1 \left(I_1 + I_3 \ldots + I_{\frac{N}{2}-1} \right) + E_2 \left(I_2 + I_4 \ldots + I_{\frac{N}{2}} \right)$$

$$= \frac{2bh^3}{3}[C(N)E_1 + D(N)E_2]$$

where *C(N)* and *D(N)* are functions of *N* that result in integer values. By calculating the values of *C(N)* and *D(N)* for various values of *N* (*N* = 4, 8, 12, 16, etc.), a pattern begins to emerge, and a polynomial can be derived to express $\langle EI_y \rangle$ as a function of N. The resulting expression is shown in Equation 1.8.

$$\langle EI_y \rangle = \frac{2bh^3}{3}\left[E_1\left(\frac{N^3+3N^2}{16}\right)+E_2\left(\frac{N^3-3N^2}{16}\right)\right] \quad 1.8$$

Equation 1.8: Equivalent longitudinal stiffness of a symmetric cross-ply laminate

1.3.2 Warping Function of a $[0/90]_{\Omega S}$ Laminate

To find g_{oi} for each ply, beginning with Equation 1.4, it is understood that internal continuity of the warping function must be maintained at the interface of two layers. In other words:

$$\left.\begin{aligned} g_{oi} &= g_{oj} \\ G_i\frac{\partial g_{oi}}{\partial n} &= G_j\frac{\partial g_{oj}}{\partial n} \end{aligned}\right\} \text{ along internal boundaries } l_{ij}$$

Then, taking into account the antisymmetry of the function g_o with respect to z, the general solution for g_{oi} is

$$g_{oi} = -\frac{E_i}{G_i}\frac{a}{6}z^3 + A_i z + B_i \quad \text{(a)}$$

where

$$a = \frac{\langle GS \rangle}{\langle EI_y \rangle} \quad 1.9$$

$$B_{\frac{N}{2}} = 0 \quad \text{(b)}$$

$$B_{N-i+1} = -B_i$$

Equation 1.9: General solution of the warping function

Now, if we introduce variable $X = \frac{N}{2}$, and calculate g_{oi} along with the corresponding coefficients A_i and B_i for various values of X, we see a pattern emerge with the coefficients. It was therefore possible to derive a polynomial function, $A_i(X)$, which allows for the simple calculation of A_i for any applicable value of X for a $[0/90]_{\Omega s}$ laminate. The derived expression is described in Equation 1.10 and is valid for $1 \leq i \leq X$.

$$A_i(X) = \frac{ah^2}{2G_{12}}\{E_1[Q(i)X^2 + R(i)X + S(i)] + E_2[T(i)X^2 - Q(i)X - R(i)]\} \quad \text{(a)}$$

where

$$Q(i) = \frac{1 + (-1)^{i-1}}{2} \quad \text{(b)}$$

$$R(i) = (-1)^i i + \left[\frac{1 + (-1)^{i-1}}{2}\right] \quad \text{(c)}$$

$$S(i) = (-1)^{i-1}\left[\frac{i(i-1)}{2}\right] \quad \text{(d)}$$

$$T(i) = \frac{1 + (-1)^i}{2} \quad \text{(e)}$$

1.10

Equation 1.10: Polynomial expression for calculating A_i for any applicable value of X

In simpler terms, the coefficients A_i can be expressed as A_{X-j}, where $0 \leq j \leq X - 1$. We define the function $A_{X-j}(X)$ such that,

$$A_{X-j}(X) = \frac{ah^2}{2G_{12}}\left[E_1\left(\frac{X^2}{2} + \frac{X}{2} + S(j)\right) + E_2\left(\frac{X^2}{2} - \frac{X}{2} - S(j)\right)\right] \quad \text{(a)}$$

where

$$S(j) = (-1)^{j+1}\left[\frac{j}{2}(j+1)\right] \quad \text{(b)}$$

1.11

Equation 1.11: Polynomial expression for calculating A_{X-j} for any applicable value of X

Using a similar procedure, by calculating B_i for various values of X, a pattern emerges. However, despite best efforts, the pattern could not be reduced to a polynomial expression. Regardless, for ease of calculation, the expression described in Equation 1.12 can be used to calculate B_{X-j} for any applicable value of X.

$$B_{X-j} = \left(\sum_{1}^{j}(-1)^j j^3\right)\frac{ah^3}{3G_{12}}(E_1 - E_2) \quad 1.12$$

Equation 1.12: Expression for calculating B_{X-j} for any applicable value of X

1.3.3 Shear Correction Coefficient for a $[0/90]_{\Omega S}$ Laminate

Once all the necessary warping function coefficients are calculated, we can proceed to calculating the shear correction coefficient, k, according to Equation 1.5. With respect to the problem of a symmetric cross-ply laminate with a rectangular cross-section, the expression for k can be rewritten as:

$$k = 2\sum_{i=1}^{X} k_i \qquad \text{(a)}$$

where:

$$k_i = \frac{1}{\langle EI_y \rangle}\int_{z_{i-1}}^{z_i} E_i g_{oi} z dz$$

$$= \frac{1}{\langle EI_y \rangle}\left\{E_i\left[-\frac{E_i}{G_{12}}\frac{a}{30}({z_i}^5 - {z_{i-1}}^5) + \frac{A_i}{3}({z_i}^3 - {z_{i-1}}^3) + \frac{B_i}{2}({z_i}^2 - {z_{i-1}}^2)\right]\right\} \qquad \text{(b)} \qquad 1.13$$

and

$$z_i = (X - i + 1)h \qquad \text{(c)}$$

Equation 1.13: Shear correction coefficient, *k*, for a symmetric cross-ply laminate

The value of k was calculated using Equation 1.6 to Equation 1.13 for various values of Ω. The resulting values are shown in Table 1.1 and charted in Figure 1.4, illustrating the asymptotic nature of the value of k for increasing values of Ω, approaching the homogenous beam value of $k = 1.2$. It is interesting to note that the value of k for $\Omega = 1$ is higher than that for $\Omega = 2$. This occurs because k of the laminate is the sum of k_i of each layer, and at the same time, k_i is inversely proportional to z^3, which is the distance from the laminate midplane to the layer in question. Therefore, when Ω increases from 1 to 2, the increase in number of layers causes a sharp decrease in k_i of the outermost layer which is not quite offset by the addition of k_i's from more layers. However, as Ω increases, the decrease in k_i of the outermost layer itself becomes less significant. After Ω increases beyond 2, the increase in k from the addition of more k_i from more layers offsets the reduction in k_i of the outermost layer and begins to increase k of the laminate asymptotically.

Table 1.1: Values of k for various values of Ω for a $[0/90]_{\Omega s}$ laminate

Ω	N	k
1	4	1.161444013
2	8	1.146531803
3	12	1.156262852
4	16	1.164123799
5	20	1.1698198
6	24	1.174028134
7	28	1.177235835
8	32	1.179751969
9	36	1.181774321
10	40	1.183433342
11	44	1.184817894
12	48	1.185990347
13	52	1.186995658
14	56	1.187867
15	60	1.18862936
16	64	1.189301902
17	68	1.189899562
18	72	1.190434152
19	76	1.190915128
20	80	1.191350153
21	84	1.191745497
22	88	1.192106344
23	92	1.192437012
24	96	1.192741129
25	100	1.193021765
26	104	1.193281536
27	108	1.193522681
28	112	1.193747134
29	116	1.193956566
30	120	1.194152437

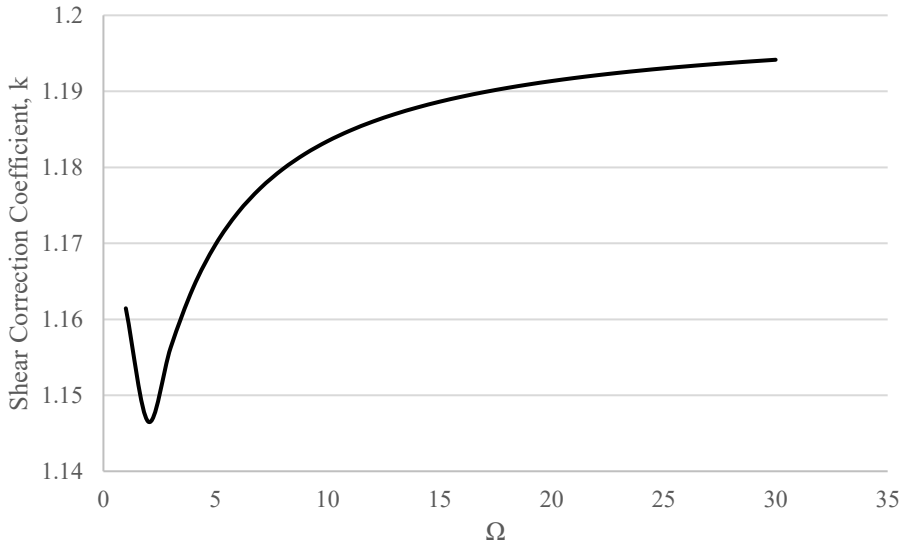

Figure 1.4: Shear correction coefficient, k, versus Ω for a $[0/90]_{\Omega s}$ laminate

1.4 Stress Concentration in Composite Laminates Due to Bolted Joints

A preferred method of fastening and joining composite components in aerospace applications involves the use of rivets or bolted joints. Such is the case for fastening the main rotor yoke to the helicopter blades. Previous work focused on composite bolted joints [31] has found that the complex stress field in the vicinity of the joint gives rise to the following typical types of composite failure, which are illustrated in Figure 1.5: (a) net-tension failure of the material across the bolt hole, (b) shear-out failure, and (c) bearing failure of the material, or combinations thereof. Net-tension failure is the tension failure of the matrix and fibres due to stress concentration. Shear-out failure propagates tangent to the bolt hole. In unidirectional and cross-ply laminates, shear-out failure results from the shear stress between fibers and matrix, while in plies that are not 0° or 90°, the fibres may be cut. Bearing failure of the material, resulting from compressive stress, can be subdivided into fiber micro-buckling, matrix cracking, fiber-matrix shearing and delamination.

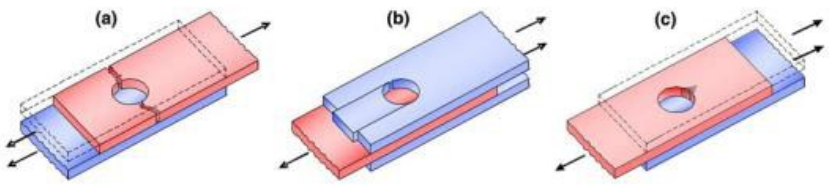

Figure 1.5: (a) Net-tension, (b) shear-out, and (c) bearing failure modes of composite bolted joints [31]

Kashaba *et al*. [32] examined the effect of washer outer diameter and clamping torque on the performance of composite bolted joints for quasi-isotropic glass/epoxy laminates with a layup sequence of $[0/\pm45/90]_s$. They found that, for the same tightening torque, the slope of the load-displacement curves of bolted joints (i.e. stiffness) increases with decreasing washer size. Additionally, in the range of tested parameters, for a given washer size, the bearing strength of the joint increased with increasing tightening torque. The observed failure developed with initial delamination between 0°, ±45°, and 90° plies due to the mismatch in strains under the compressive bearing load, followed by tension failure of the 90° plies, shear-out failure of the 0° plies, and finally, nearly catastrophic bearing failure of the ±45° plies.

Gorjipoor *et al*. [33] investigated numerically and experimentally the strain distribution in a thick composite plate in the vicinity of a bolted joint subjected to various clamping torques. A three-dimensional finite element model, validated with strain gauge and digital image correlation (DIC) results, was developed and used to analyze the effect of plate thickness on the development of interlaminar stresses. It was found that interlaminar shear strain values and their variation through the thickness of the laminate became more significant with increasing thickness. Additionally, the effect of clamping force propagated further from the bolt hole in thicker laminates.

1.5 Thesis Motivation and Objectives

As described in the above literature survey, composite structures are steadily gaining popularity in highly loaded, often dynamic applications where a relatively large thickness is required of the part. This increased thickness gives rise to additional concerns regarding manufacturing and performance prediction. Optimization of the cure cycle has been discussed, and important considerations for proper thick composite manufacturing have been explained. As it pertains to the quasi-static testing of thick laminates, most work has been theoretical in nature, with the aim of reducing computational effort. Owing to the tapered nature of many of the thick sectioned composite structures currently used in load bearing aerospace applications, a lot of research has been done to predict how tapered laminates perform in flexural fatigue. However, industry experience with composite structures in bending shows that the load introduction area of the thick

section is most critical, with little research work being made available in this regard. Some interest has been shown towards bolted joint connections, which are a preferred method of fastening composite parts. Although, most research is focused on the effect of bolted joint connections in thin laminates loaded in tension, compression, or in-plane shear. All this considered, more research is needed to study uniformly thick composite plates subjected to flexural bending with bolted joint connections.

This study is part of a group project encompassing several branches: process-induced temperature distribution and residual stresses of thick laminates, quasi-static flexural bending behaviour of thick laminates with bolted-joint connections, and fatigue behaviour of said thick laminates. The end goal of this project is to be able to predict the fatigue failure of thick composite beams with bolted-joint connection using finite element analysis software. The focus of this thesis is on the flexural bending behaviour of uniformly thick laminated composite plates with a bolted joint connection to represent the critical area of a helicopter's main rotor yoke. The specific objectives of this study can be broken down as follows:

- Manufacture glass/epoxy laminates to be tested in cantilever bending. Samples with bolted joint connections on the fixed and loaded ends have a stacking sequence of $[0]_{80}$. Samples with bolted joint connections only on the fixed end have stacking sequences of $[0]_{20}$, $[0]_{40}$, $[0]_{60}$, $[0]_{80}$, and $[0/90]_{20s}$.
- Provide ultimate strength data to design flexural fatigue tests.
- Provide surface strain measurements, load vs. deflection data, and failure crack images for validating a theoretical model.
- Observe the effect of changing layup sequence and specimen thickness on the flexural behaviour of rectangular composite beams.

CHAPTER 2 MANUFACTURING OF SAMPLES

The experiments carried out under the scope of this thesis examine the flexural bending behaviour of glass/epoxy laminates. The results of the experiments are used to validate an ANSYS model that is developed by Gorjipoor [38] to predict the stresses and strains due to cantilever loading, as well as failure displacements and crack formation. To obtain the necessary results, 80-layer samples of unidirectional and cross-ply layup sequences were tested, along with unidirectional samples of 20, 40, and 60 layers. Three specimens were fabricated for each sample type. The full-thickness test specimens were labeled FS#, where # corresponds to the order in which the sample was made (1, 2, 3, 4, …), irrespective of layup sequence and whether the specimen was used for quasi-static or fatigue testing. The 20-layer samples were labeled F20_x, the 40-layer samples F40_x, and the 60-layer samples F60_x, where x (x = 1, 2, or 3).

2.1 Material

The samples were manufactured using unidirectional layers of CYCOM E773-S2 glass/epoxy prepreg from CYTEC, with a cured ply thickness of 0.009 inches. The material was provided by the industrial partner and the samples were cured according to a cure cycle also obtained from the industrial partner, which was designed to minimized temperature overshoot at the centre of the laminate and provide a uniform degree of cure. After curing and machining the samples, buffer pads made of 1/16-inch thick G-7 Garolite were bonded to the surface, as will be described in section 2.4 (Sample Preparation for Flexural Bending Test) using 163-2 adhesive film by 3M.

2.2 Specimen Fabrication

The specimens were fabricated to meet the design specifications set out by the industrial partner. The specimen dimensions required by the industrial partner are shown in Figure 2.1. This configuration, with buffer pads and bolt holes on both ends of the sample, is referred to as the ‘clamped’ configuration. For the purpose of this thesis, it was deemed insufficient to limit the experiments to samples with 80 unidirectional layers and bolted joint connections on both ends. As such, 80-layer cross-ply samples were

manufactured along with unidirectional samples of 20, 40, 60, and 80 layers that had buffer pads and bolt holes only on the loaded end of the samples. This specimen configuration, shown in Figure 2.2, is referred to as the 'cantilever' configuration. These were chosen to better represent pure cantilever-type loading by limiting the loading constraints to a line load application, as opposed to clamping a significant portion of the laminate. After cutting the prepreg plies, the laminate was laid up by hand, vacuum bagged, then cured in an autoclave. After curing, the edges of the laminate were trimmed and kept for inspection and quality assurance (QA), then the laminate was machined to the final specimen dimensions and the bolt holes were drilled. Finally, the buffer pads were bonded to the sample. Figure 2.3 shows images of the laminate at each process step. A zero-bleed vacuum bag assembly was used to minimize resin bleeding.

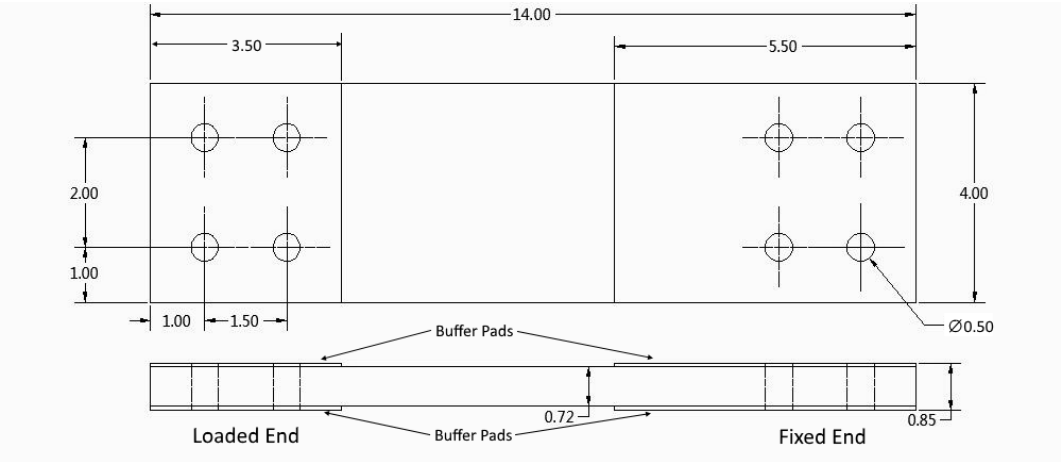

Figure 2.1: Clamped specimen configuration

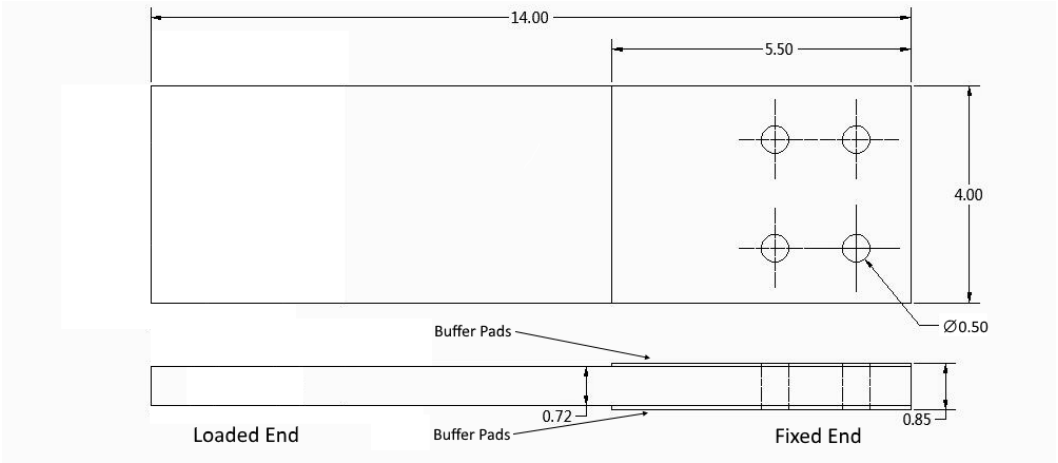

Figure 2.2: Cantilever specimen configuration

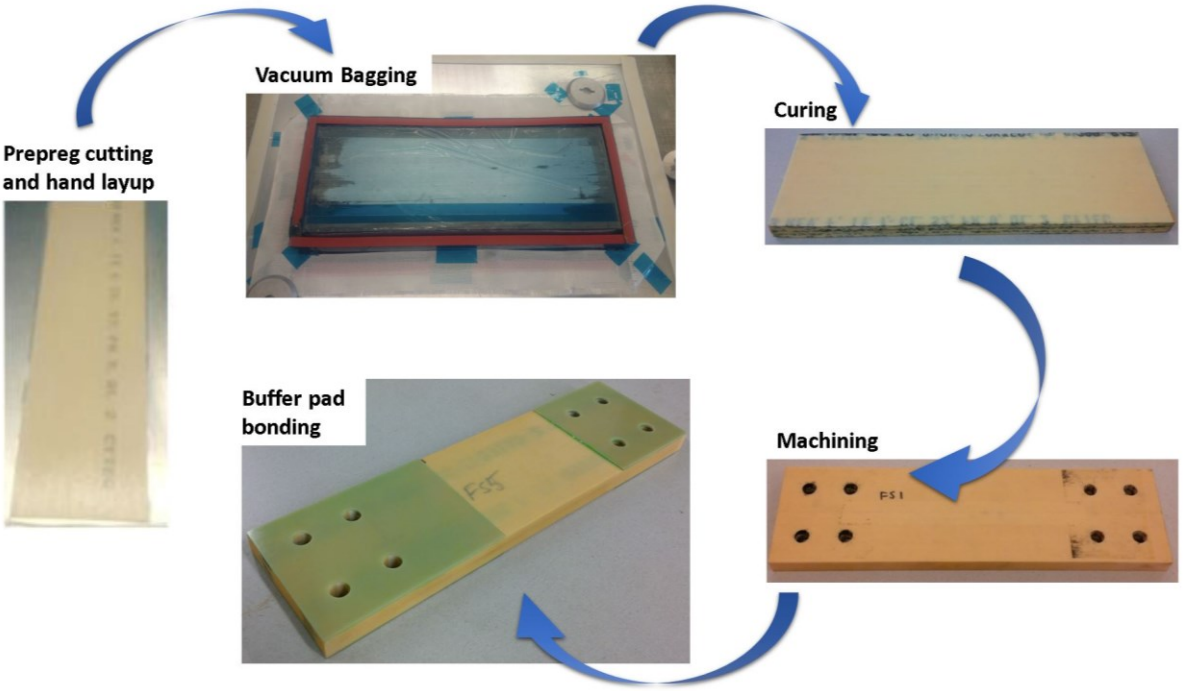

Figure 2.3: Flex beam fabrication process

After bagging, the laminate stack is ready for curing. This was done in an ASC autoclave, capable of 800 °F and 300 psi of pressure. The cure cycle is shown graphically in Figure 2.4 and followed the following sequence, controlled using a lagging thermocouple placed at the mid thickness of the long edge of the laminate:

- Apply full vacuum
- Ramp temperature to 170 °F at 2 °F/min and apply 10 psig of pressure
- Hold for 80 minutes
- Vent vacuum to atmosphere
- Ramp temperature to 275 °F at 2 °F/min and increase pressure to 90 psig
- Hold for 90 minutes
- Cool to 125 °F at 3 °F/min
- Relieve pressure when temperature is below 125 °F

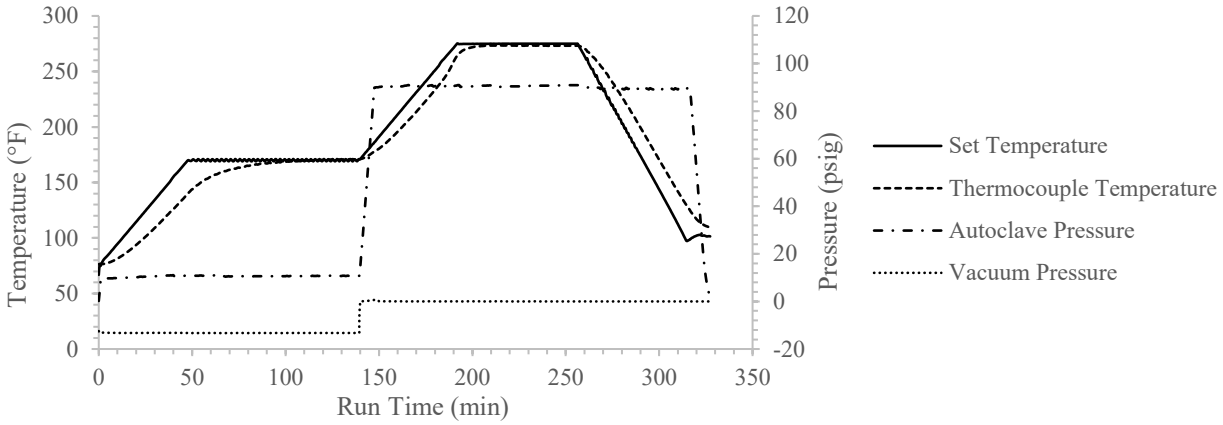

Figure 2.4: E773-S2 glass fibre Flex Beam autoclave cure cycle

After curing, the samples were trimmed to near net shape using a water-cooled diamond saw and the edges were kept, to perform QA checks. The trimmed samples were then machined to net shape and had the bolt holes drilled using a ½" diameter end mill.

2.3 Quality Assurance (QA)

To ensure that the cure cycle in Figure 2.4 results in a satisfactory laminate, the temperature profile in an 80-ply laminate resulting from the cure cycle was investigated in [17]. The maximum recorded temperature of 325 °F expectedly occurred at the direct centre of the laminate. This 50 °F overshoot did not bring the resin temperature high enough to cause matrix degradation, which begins at 437.5 °F. To confirm that the cure cycle resulted in a high-quality part, thermo-gravimetric analysis (TGA) and differential scanning calorimetry (DSC) were performed on samples of sections cut from one full-thickness specimen. When the cure cycle was deemed satisfactory, the remaining test samples were made and the thickness distribution in the gauge area was verified. Additionally, fibre volume fraction and void content measurements were taken from most full-thickness samples. These QA processes are described in the following subsections. The fibre volume fraction and void content QA checks were not performed on samples of 20, 40, or 60 layers as they were deemed unnecessary due to the consistency of previous QA checks proving the repeatability of the manufacturing process.

2.3.1 Thermo-Gravimetric Analysis (TGA) and Differential Scanning Calorimetry (DSC)

To perform TGA and DSC tests, Texas Instrument Q50 and Q10 machines were used, respectively. Samples were taken from sections of a sacrificial full-size specimen that was cured using the cure cycle in Figure 2.4. From each section, 20 mg samples were cut from the top, mid-thickness, and bottom. The approximate locations of the sections are shown in Figure 2.5. The TGA test determined the thermal degradation point of the epoxy in the samples. A typical TGA test result is shown in Figure 2.6. It can be seen that the epoxy begins to degrade at 437.5 °F (225.3 °C).

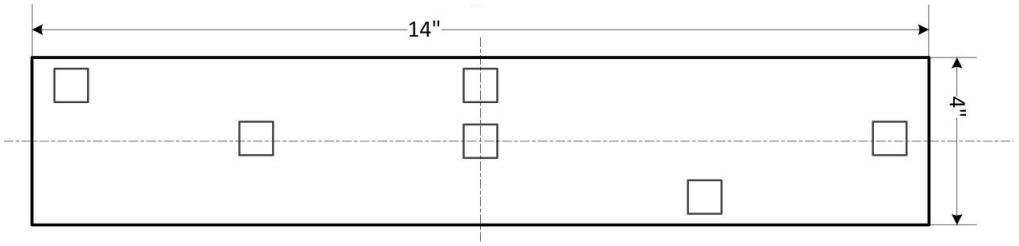

Figure 2.5: Locations of sections used for TGA and DSC tests

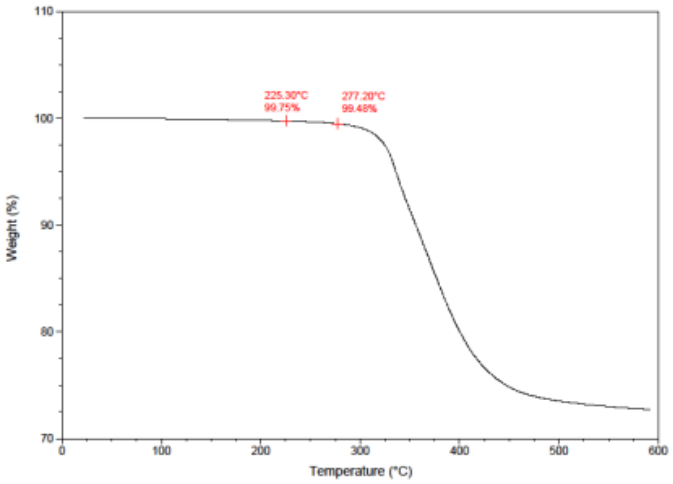

Figure 2.6: Typical TGA test result

The DSC test determined the degree of cure of the samples taken from the specimen. The samples were placed in a hermetically sealed aluminum pan and were run through a heat-cool-heat cycle. Each sample tested followed a profile like that of the DSC results shown in Figure 2.7. The resulting graph shows the heat flow through the sample and aluminum pan versus the temperature applied to the pan. Since uncured epoxy undergoes an exothermic reaction when the temperature goes above the cure initiation

temperature, the heat flow increases due to the excess heat generated by the reaction. Therefore, in a heat-cool-heat DSC test, the first heat line records any exothermic spike as the small sample becomes fully cured. The second heat line is then used as a base line for the heat flow profile of a fully cured sample. The difference between the exothermic spike and the baseline is inversely proportional to the degree of cure. It is clear from this graph that there was no exothermic spike measured and the heat flow profile of the first heat line matches that of the second heat line, meaning the sample was fully cured.

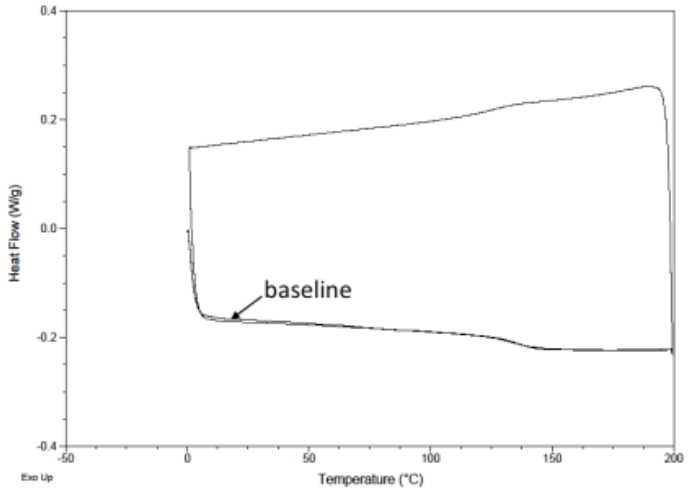

Figure 2.7: Typical DSC test results

2.3.2 Thickness Measurements

After the cure cycle was verified, the remaining test specimens were manufactured. To verify the surface geometry, 15 measurements were taken of the thickness by micrometer at various locations in the gauge area of each specimens. The average thicknesses of each specimen configuration are listed in Table 2.1 along with the standard deviation and coefficient of variation of the measurements.

Table 2.1: Thickness distribution of each sample configuration

	80-Layer Clamped	80-Layer Cantilever	80-Layer Cross-Ply	60-Layer	40-Layer	20-Layer
Average (in)	0.7164	0.7130	0.7399	0.5462	0.3696	0.1860
Std Dev. (in)	0.0142	0.0120	0.0052	0.0053	0.0051	0.00316
CV (%)	1.9796	1.6820	0.6961	0.9782	1.3679	1.9153

2.3.3 Fibre Volume Fraction

To ensure that each full-thickness test specimen did not maintain an excess amount of resin, nor that it lost too much resin due to bleeding, the fibre volume fraction was measured according to ASTM D2584-11 "Standard Test for Ignition Loss of Cured Reinforced Resins" [34]. To execute this test, full-thickness samples of about 0.75" x 0.5" were cut from the trimmed edges of the sample at the locations shown in Figure 2.8. To complete the test, the following equipment was needed: porcelain crucible (Fisherbrand 965-L, 50 ml capacity), electric muffle furnace (Thermolyne 1400 Furnace, capable of 1200 °C), thermocouple, and desiccator. To obtain the fibre volume fraction, it is necessary to know the corresponding weight percentages of fibres and resin contained in the sample sections. These were obtained by the following procedure:

1. Clean the porcelain crucible with acetone and heat it in the muffle furnace at 600 °C for 2 hours.
2. Allow the crucible to cool down to room temperature in a desiccator and record weight to nearest 0.1 mg.
3. Clean a sample section with alcohol and place inside a desiccator for one whole day before ignition test, then record weight as W_1.
4. Heat sample in furnace to 600 °C for 7 hours.
5. Place sample remnants in a desiccator to cool overnight and record weight as W_2.

The ignition loss (resin weight %) of each sample is then calculated using the following equation:

$$Ignition\ loss, weight\ \% = \frac{(W_1 - W_2)}{W_1}, \qquad 0 \leq Ignition\ loss \leq 1$$

Where,

W_1 = weight of sample before ignition test, g

W_2 = weight of sample remnants after ignition test, g

The fibre volume fraction can then be calculated using:

$$V_f = \frac{(D \times W_{fibre,\%})}{(D \times W_{fibre,\%}) + (d \times W_{resin,\%})}, \qquad 0 \leq V_f \leq 1$$

Where,

D = density of reinforcement from material supplier, g/cm^3 = 2.49 g/cm^3 for glass

d = density of resin from material supplier, g/cm^3 = 1.28 g/cm^3 for epoxy

$W_{resin,\,\%}$ = Ignition loss, weight % = resin weight fraction, $0 \leq W_{resin,\,\%} \leq 1$

$W_{fibre,\,\%} = 1 - W_{resin,\,\%}$ = fibre weight fraction

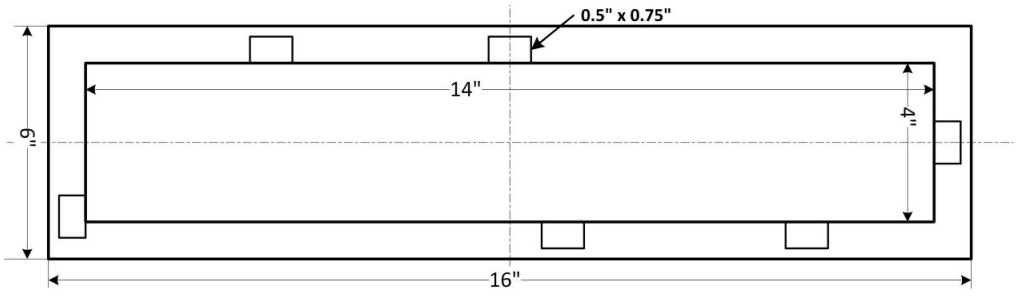

Figure 2.8: Locations of sample sections used for resin weight fraction tests

2.3.4 Void Content

The void content was measured for each of the same samples used in the ignition loss test by the density measurement method, as described in ASTM D2734-09 "Standard Test Methods for Void Content of Reinforced Plastics" [35]. The void content can be obtained by comparing the measured density of the samples to the theoretical density according to:

$$V_{void} = \frac{D_T - D_M}{D_T}, \qquad 0 \leq V_{void} \leq 1$$

Where D_T is the theoretical composite density, and D_M is the measured composite density. The theoretical density is calculated using the following equation, where the variables are as described in section 2.3.3 (Fibre Volume Fraction):

$$D_T = \frac{100}{\left(\frac{W_{fibre,\%}}{D} + \frac{W_{resin,\%}}{d}\right)}$$

The measured composite density was determined using a Sartorius density determination kit and balance (max 220 g, d=0.1 mg), which can be seen in Figure 2.9. This device makes use of the Archimedean principle to determine an object's specific gravity. This was done for each sample cut from the specimens

before the ignition loss test was performed. When an object is immersed in a fluid, the resulting buoyancy force is equal to the weight of the fluid that is displaced by the volume of the object in the fluid. Therefore, with the density determination kit, the weight of an object in air, as well as in water, can be determined. Distilled water was used as the liquid for submersion, since the density of the fluids involved must be accurately known.

Due to the very high accuracy needed to calculate void content, the following errors were considered and mitigated according to the troubleshooting steps outlined in [36]. First, the density of distilled water varies with temperature. Therefore, a thermometer was placed in the water to get the exact temperature, and the density was chosen accordingly. Second, the sample is subject to buoyancy forces from the air while being weighed. Therefore, the specific gravity of the solid sample was corrected to allow for air buoyancy. The resulting equation is as follows:

$$\rho = \frac{W_a[\rho_{fl} - \rho_a]}{W_a - W_{fl}} + \rho_a \qquad [36]$$

Where,

ρ = specific gravity of sample

W_a = weight of the sample in air, g

W_{fl} = weight of the sample in water, g

ρ_a = density of air under standard conditions, g/cm^3 = 0.0012 g/cm^3

ρ_{fl} = density of water, g/cm^3

One cubic centimetre of air at standard conditions weighs approximately 1.2 mg. Third, while submerged in water, the wires attached to the pan hanger assembly displace additional water. A correction factor is provided based on the size of the beaker in which the sample is immersed in water. The large beaker was used for this test, with a diameter of 76 mm. As such, the correction factor is added to the previous equation to yield:

$$\rho = \frac{W_a[\rho_{fl} - \rho_a]}{0.99983[W_a - W_{fl}]} + \rho_a \qquad [36]$$

Fourth, air bubbles adhere to the surface of the sample, which skews the volume measurements. To prevent bubbles from sticking to the sample surface, the samples were polished to reduce surface tension.

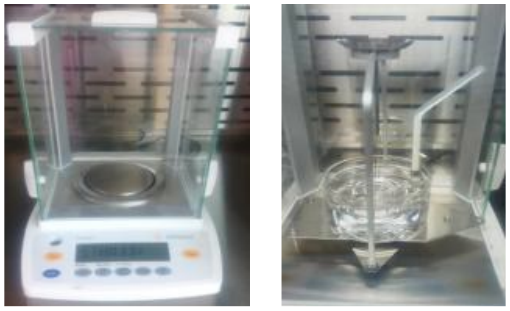

(a) (b)

Figure 2.9: Sartorius (a) balance and (b) density determination kit

2.3.5 Results of QA Tests and Discussion

The spread of data for resin weight fraction, fibre volume fraction, void content, and density measurements was checked. These results are summarized in Table 2.2. The results in the $[0]_{80}$ row show the averages from 12 specimens, while the results in the $[0/90]_{20s}$ row are the averages taken from 8 specimens. It should be noted that some specimens of each specimen type were used for quasi-static testing, and the others were used for fatigue testing. It can be seen from the spread of data that the chosen manufacturing procedure repeatedly and consistently resulted in quality laminates.

Table 2.2: QA test results summary

Sample Type	Resin Weight Fraction (Experimental Results)	Fibre Volume Fraction (Calculated Results)	Void Content (Calculated Results)	Measured Density (g/cm^3) (Experimental Results)
$[0]_{80}$	32.33 ± 0.72%	51.83 ± 0.80%	1.0 ± 0.1%	1.90 ± 0.01
$[0/90]_{20s}$	32.34 ± 0.85%	51.82 ± 0.98%	1.1 ± 0.1%	1.89 ± 0.01

As discussed in section 1.1 (Manufacturing of Thick Composite Laminates), laminate quality is dependent on proper vacuum debulking, a well-made vacuum bag setup, and appropriate autoclave curing cycle. The autoclave cure cycle has been discussed previously. In the early stages of this study, the vacuum bag assembly went through a few iterations before being finalized. Initial attempts at vacuum bagging

resulted in far too much resin bleeding, reducing the uncured laminate thickness of 0.72” to as low as 0.60” after curing. This resin bleeding caused the edges of the laminate to slope away from the centre and gave rise to higher void content and lower resin weight fraction, otherwise interpreted as a higher fibre volume fraction. Initially, aluminum dams were used, which left large gaps from which the resin can flow out. These were subsequently replaced with rubber dams, which dramatically improved resin loss. However, another source of resin bleeding and void formation was due to the difficulty in cutting so many prepreg sheets to the exact same size, then placing the sheets exactly one on top of the other and maintaining parallel surfaces after debulking. None of these two issues was resolved and they led to imperfect contact between the dams, caul plate, and laminate. This imperfect contact left room for air pockets that could allow resin to flow. This seemed to have more of an effect on the thickness distribution than anything else, yet the laminates were still satisfactory. Figure 2.10 shows a schematic of the initial bagging procedure. Figure 2.11 shows the excessive resin bleeding from this initial vacuum bagging compared to a typical result of the modified bagging procedure.

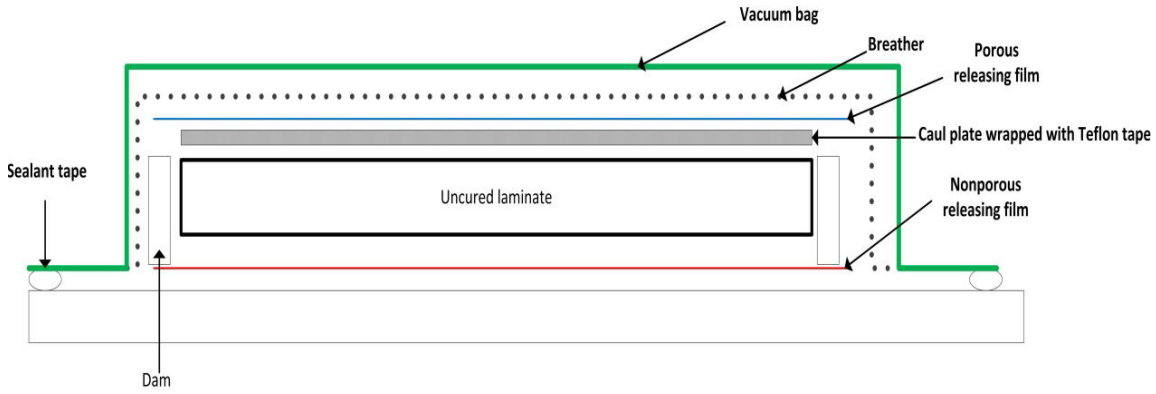

Figure 2.10: Schematic of initial vacuum bagging setup

(a) (b)

Figure 2.11: Resulting resin bleeding from (a) initial and (b) modified vacuum bagging setup

Aside from the vacuum bagging assembly, the vacuum debulking process during hand layup also underwent a few iterations. Proper vacuum debulking is necessary to remove entrapped air before curing. In this study, three vacuum debulking conditions were tested: debulking (a) every 8 plies for 10 minutes, (b) every 4 plies for 10 minutes, and (c) every 3 plies for 5 minutes. The first condition could not properly remove the entrapped air as the pressure did not penetrate through all 8 layers of prepreg. This resulted in large irregularly shaped voids appearing in the cured laminate. The second and third debulking conditions resulted in similarly small and sparse voids, which was adequate for a good quality laminate. In the interest of saving on manufacturing time, the third debulking condition was chosen as the final one. Micrographs of cured samples prepared with each of the three vacuum debulking conditions are shown in Figure 2.12.

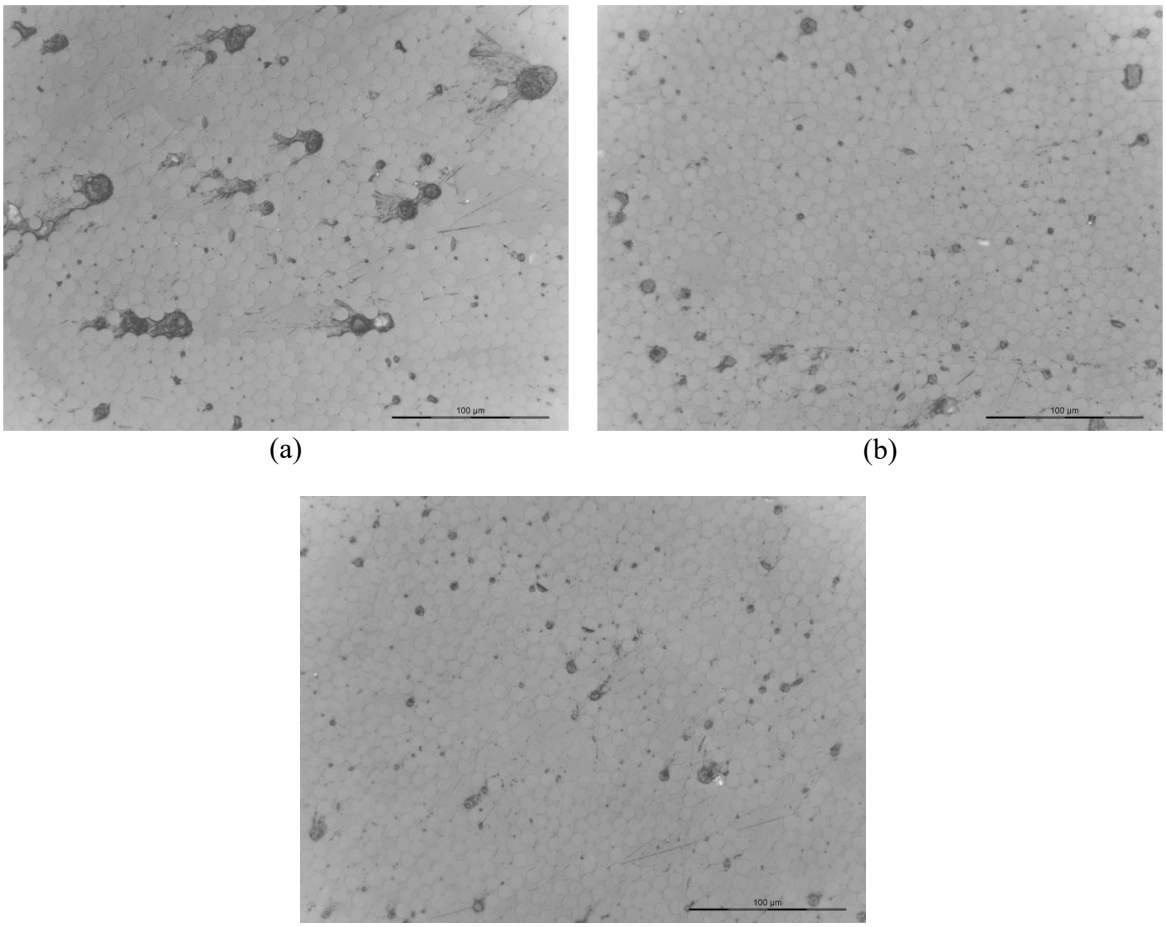

(a) (b)

(c)

Figure 2.12: Cured specimen micrographs at 50x magnification with vacuum debulking (a) every 8 plies for 10 minutes, (b) every 4 plies for 10 minutes, and (c) every 3 plies for 5 minutes

2.4 Sample Preparation for Flexural Bending Test

In order to limit the effect of stress concentration from the sharp edges of the testing machine against which the sample is loaded, buffer pads were bonded to the fixed and loaded ends, as applicable, according to the dimensions shown in Figure 2.1 and Figure 2.2. This process step occurred after the samples were machined to net shape. The buffer pad bonding procedure went as follows:

1) Premade glass fiber laminates (McMaster-Carr, grade G-7 ultrahigh temperature Garolite 1/16" thick) were cut to slightly larger dimensions than required.
2) Using an electric sheet sander and sand paper (120 grit), the matting surfaces of the sample and Garolite were roughened, then cleaned with alcohol and allowed to air dry thoroughly.
3) Sheets of adhesive film (3M 163-2M) were cut to the required dimensions and placed on the laminate, followed by the Garolite sheets.
4) The prepared laminate and buffer pads were placed on an aluminum tool and bagged according to the schematic in Figure 2.13, where the bagging materials used are the same as described in section Specimen Fabrication).
5) The vacuum bag assembly was cured according to the manufacturer's recommended cure cycle shown in Figure 2.14, using the autoclave thermocouple for control.
6) Once the adhesive film was cured, the buffer pads were trimmed to net shape and had the bolt holes drilled using a ½" end mill.

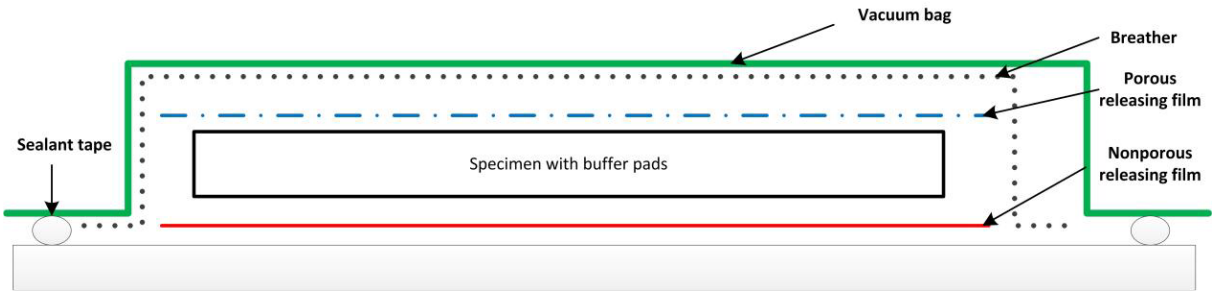

Figure 2.13: Vacuum bag assembly for buffer pad bonding

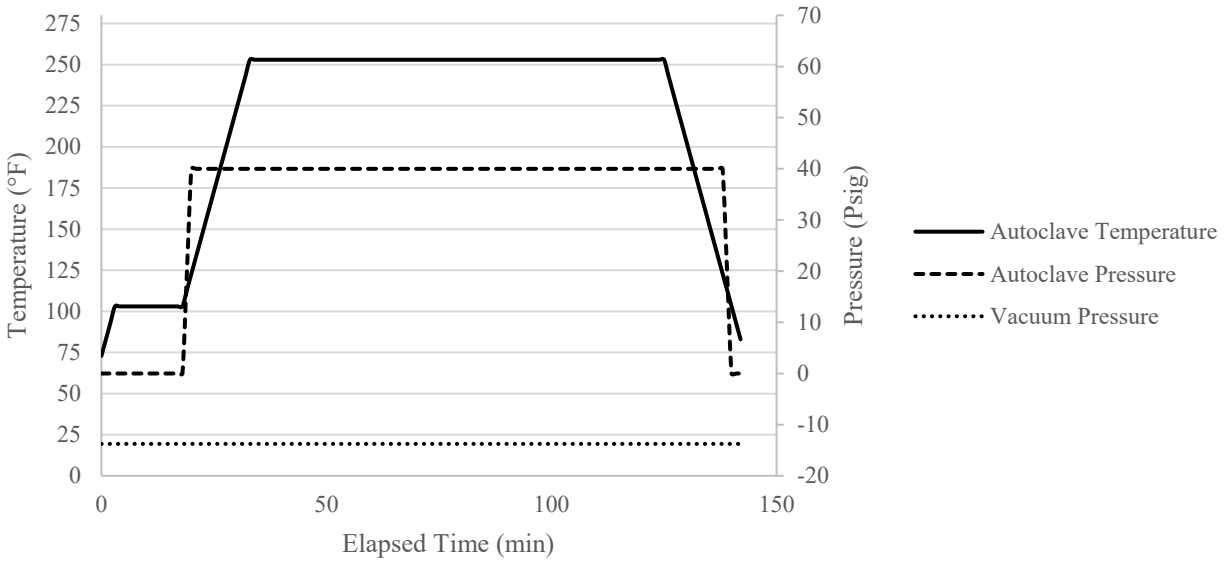

Figure 2.14: Autoclave cure cycle for buffer pad bonding

Following the buffer pad bonding, the samples either had strain gauges applied or had to be prepared for digital image correlation (DIC), which would be used for full field surface strain measurements that would then be compared to FEA results. Initially, tests were carried out on samples with an array of strain gauges mounted to the top and side surfaces of the sample. The top surface had linear gauges (Micromeasurements EA-06-031CE-350 linear gauge) for axial and transverse strain measurements, while the side surface had stacked T-gauges (Micromeasurements C2A-06-031WW-120 stacked T-gauge) for shear strain measurement. Figure 2.15 shows a schematic of a strain gauge array on the (a) top and (b) side surfaces of the sample, where the location through the thickness of the gauge is indicated in %thickness rather than absolute thickness due to the minor differences in thickness between specimens. In this figure, the 3.5-inch portion of the fixed end that is labeled as the "Clamped Region" represents the part of the specimen that is clamped in place in the test fixture. During the early stages of this study, there were several issues encountered while using a strain gauge array. These issues will be discussed in greater detail in section 3.2.1 (Experimental Procedure). After a few samples had been tested with a strain gauge array, DIC was found to be a more efficient and effective method for surface strain measurement. As such, DIC replaced the strain gauge array for most of the samples tested.

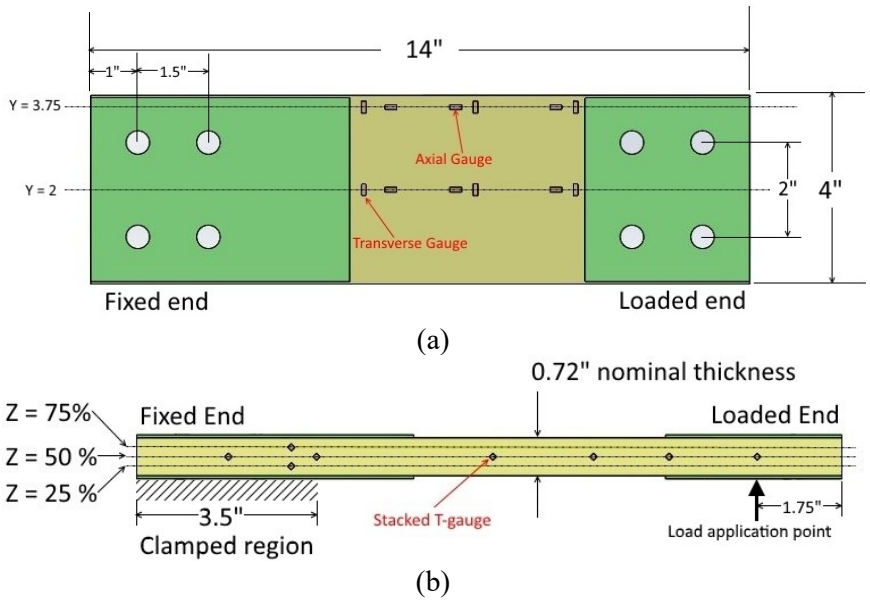

Figure 2.15: Example strain gauge array on a full-thickness sample

DIC was employed on the top surface between the edge of the buffer pad and the loading point, and on the side surface around the location of ultimate shear strain as predicted by initial trials with FEA. These areas are highlighted in Figure 2.16, while Figure 2.17 shows a typical speckle pattern for the (a) top and (b) side surfaces of a specimen. To achieve the desired speckle pattern, the areas of interest were first sanded using 180 grit sandpaper and cleaned with isopropyl alcohol. Then, they were painted with matte finish white acrylic paint (Liquitex Professional Acrylic Artistic Colour Titanium White) using a nylon brush to minimize brush marks. Once dried, the paint was sanded smooth using 600 grit sandpaper. This coating of white paint provided the background for the speckle pattern. The speckles were subsequently applied using an airbrush (Master Airbrush Model E91 airbrush set with compressor) and matte black ink (Liquitex Professional Acrylic Ink! Carbon Black). As a rule of thumb, once the DIC cameras are setup and focused, the average speckle should appear at least 5 pixels in size. The pressure of the airbrush can be regulated to achieve the desired speckle size.

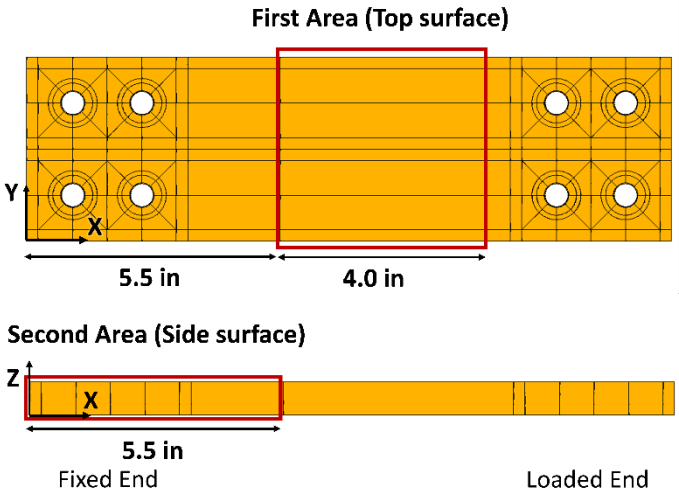

Figure 2.16: Areas of interest for DIC

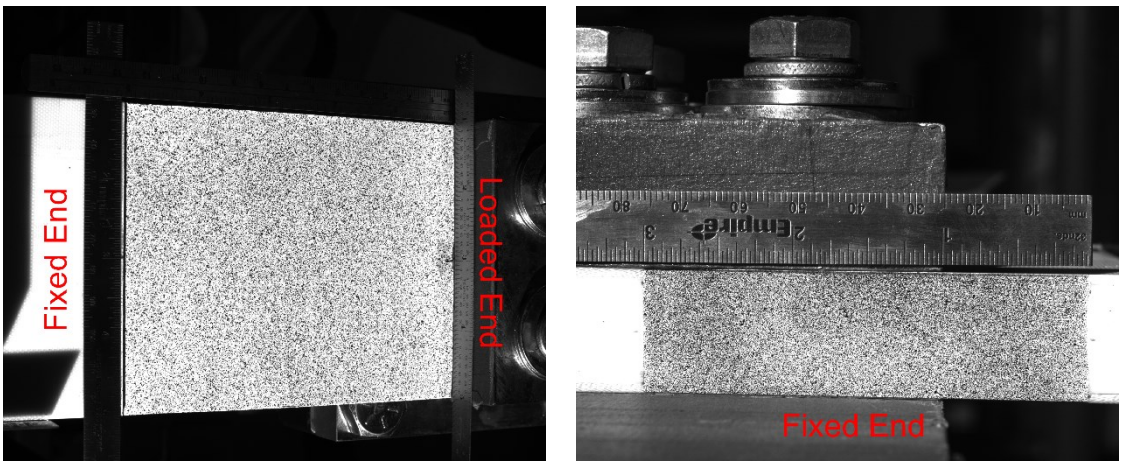

(a) (b)

Figure 2.17: Typical DIC speckle pattern on the (a) top and (b) side surfaces of a specimen

CHAPTER 3 EXPERIMENTAL METHOD

Considering the thick plate as a simplification of the blade of a helicopter main rotor yoke, the testing machine was designed to apply a bending moment to the laminate via a bolted joint connection. In addition, a fixture that clamps the loaded end of the specimen between two cylindrical faces was designed to change the bolted connection at the loading end to a cantilever-type boundary condition for a greater depth of analysis. This study was conducted in conjunction with experimental fatigue tests and theoretical finite element analysis using commercially available ANSYS software and a user generated code for failure prediction that was developed in house at the Concordia Center for Composites (CONCOM). The results from the quasi-static tests were used to determine the limits of the fatigue tests. Also, the quantitative experimental results were used to validate the ANSYS model, while the qualitative results from ANSYS were used to determine the critical areas of interest for observation during quasi-static testing in an iterative process. Some notes about the test setup, test specifications and finite element analysis are discussed in this chapter.

3.1 Test Setup

Figure 3.1 shows a CAD model and a picture of the test setup which was used to perform the flexural bending tests. The machine was designed as part of the report by Heer [37] and was installed in the CONCOM material characterization lab. A displacement-controlled MTS 244 Series hydraulic actuator was used to apply force at the loading end, with maximum displacements of +78 mm and -53 mm. This actuator is equipped with MTS Series 249G2 swivel ball joints at both ends to allow it the freedom to pivot and ensure axial loading of the actuator during operation. What is not shown in the CAD model of Figure 3.1a are the two Teflon guide rails that are mounted on the two large I-beams adjacent to the actuator to prevent lateral motion. These can be seen in the picture in Figure 3.1b along with retaining blocks and a collar in place for when the actuator is not securely fastened to the sample. These retaining blocks prevent the actuator from pivoting away from the sample and the collar prevents the actuator from descending when the hydraulic pump is not activated. The fixed end of the sample is clamped to the heavy steel cross-beam

under a 1-inch thick steel block using four ½-13UNC-2A bolts. There are two clamping fixtures for the loaded end of the sample which are attached to the top swivel ball joint of the actuator. Figure 3.1a shows the clamped configuration which fixes the loaded end of the sample to the actuator by clamping it with a 1-inch thick steel block and four ½-13UNC-2A bolts. Figure 3.1b shows the cantilever configuration which clamps the end of the sample between two cylindrical faces which are fastened together using two 5/16-18UNC-2A bolts. Figure 3.2 shows a close-up of the loaded end for each loading configuration with associated dimensions, along with a CAD model of the cantilever loading fixture to better illustrate the cylindrical surfaces. As can be deduced by the boundary conditions imposed by the ball joints of the actuator, the orientation of the actuator and clamping fixture changes throughout loading. As such, it was important to find a relationship between the actuator displacement, and the resulting displacement of the specimen. Therefore, the sample and fixture were modeled in the commercially available CAD software SolidWorks, and a geometric deflection analysis was conducted to obtain an approximation of this relationship. This process is discussed in greater detail in section 4.1 (Relationship Between Actuator Displacement and Specimen Deflection).

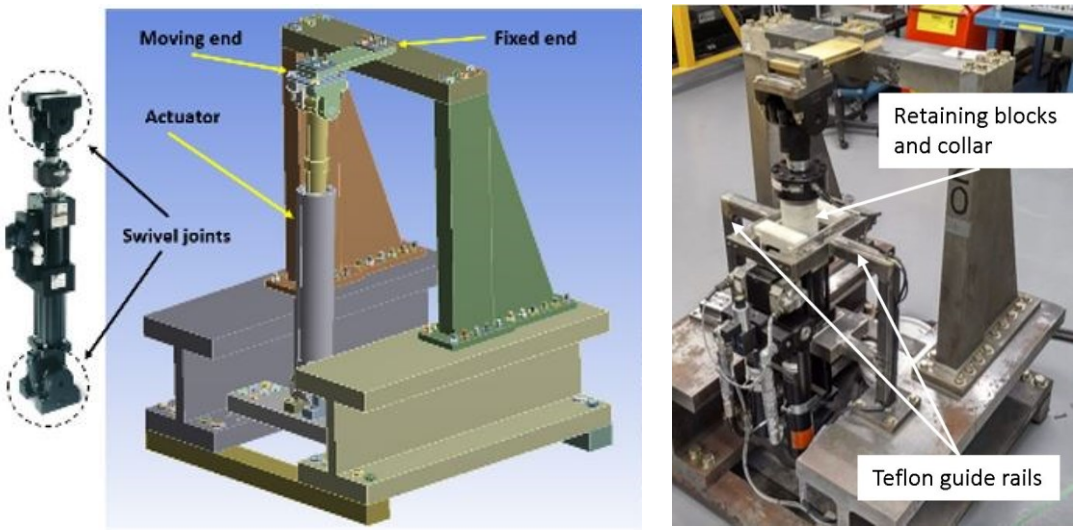

(a) (b)

Figure 3.1: Flexural bending test machine (a) CAD model and (b) picture

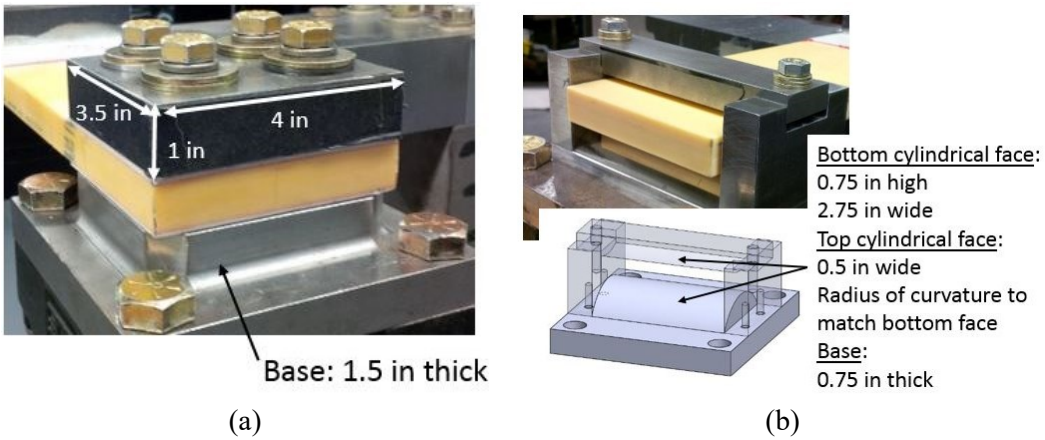

Figure 3.2: Loading fixtures for (a) clamped and (b) cantilever configurations

3.2 Test Specifications and Procedure

To validate the ANSYS model, experiments were carried out for each 80-layer specimen configuration: three samples each for unidirectional clamped, unidirectional cantilever, and cross-ply cantilever. The study was then rounded out by examining the effect of thickness by testing three cantilever samples each of 20, 40, and 60 unidirectional layers. Initially, strain gauges were employed to measure the surface strains on the specimens. This method was subsequently replaced by digital image correlation (DIC) for full-field surface strain measurements on the top and side surfaces of the specimens. Figure 3.3 shows the coordinate system used for describing locations on the sample, along with nomenclature used for describing the strain gauges applied to the specimen. Table 3.1 summarizes the gauges used for each applicable specimen and indicates the loading conditions for the failure test.

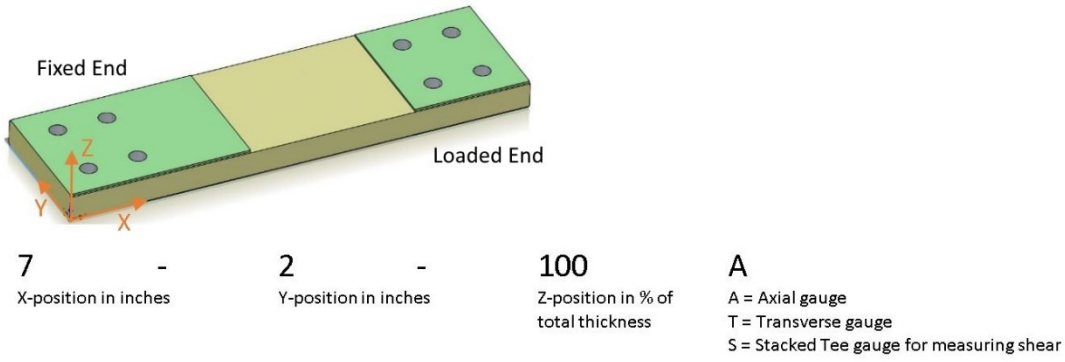

Figure 3.3: Coordinate system and strain gauge code description

Table 3.1: Summary of sample type, loading condition, and strain gauges used

Sample Configuration	Sample Number and Layup	Loading Conditions	Strain Gauges/DIC
Unidirectional Clamped	FS3 $[0]_{80}$	2 mm/min	Axial: 6.25-2-100A, 6.25-3.75-100A, Transverse: 5.75-3.75-100T, 10.25-2-100T Shear: 1.75-0-50S, 2.5-0-75S, 3.5-0-50S, 9-0-50S
	FS5 $[0]_{80}$	2 mm/min	Axial: 6.25-2-100A, 6.25-3.75-100A, 7.5-2-100A, 7.5-3.75-100A, 9.75-2-100A, 9.75-3.75-100A Transverse: 5.75-2-100T, 5.75-3.75-100T, 8-2-100T, 8-3.75-100T, 10.25-2-100T, 10.25-3.75-100T Shear: 1.75-4-50S, 2.5-0-50S, 3.025-0-50S, 3.025-4-25S, 3.025-4-75S, 10.5-4-50S
	FS22 $[0]_{80}$	5 mm/min	Shear: 3.025-4-50S and DIC
Unidirectional Cantilever	FS17 $[0]_{80}$	5 mm/min	Axial: 6.25-2-100A, 6.25-3.75-100A, 7.5-2-100A, 7.5-3.75-100A, 9.75-2-100A, 9.75-3.75-100A, 11.5-2-100A, 11.5-3.75-100A, 13.25-2-100A, 13.25-3.75-100A Transverse: 5.75-2-100T, 5.75-3.75-100T, 8-2-100T, 8-3.75-100T, 10.25-2-100T, 10.25-3.75-100T, 12-2-100T, 12-3.75-100T, 12.75-2-100T, 12.75-3.75-100T, 13.75-2-100T, 13.-75-3.75-100T Shear: 1.75-4-50S, 2.5-4-50S, 3.025-0-50S, 3.025-4-25S, 3.025-4-75S, 3.5-0-50S, 7-0-50S, 10.5-4-50S, 12.25-4-50S, 13.5-0-50S
	FS18 $[0]_{80}$	5 mm/min	Axial: 6.25-2-100A, 6.25-3.75-100A, 7.5-2-100A, 7.5-3.75-100A, 9.75-2-100A, 9.75-3.75-100A, 11.5-2-100A, 11.5-3.75-100A, 13.25-2-100A, 13.25-3.75-100A Transverse: 5.75-2-100T, 5.75-3.75-100T, 8-2-100T, 8-3.75-100Tm 10.25-2-100T, 10.25-3.75-100T, 12-2-100T, 12-3.75-100T, 12.75-2-100T, 12.75-3.75-100T, 13.75-2-100T, 13.-75-3.75-100T Shear: 1.75-4-50S, 2.5-4-50S, 3.025-0-50S, 3.025-4-25S, 3.025-4-75S, 3.5-0-50S, 7-0-50S, 10.5-4-50S, 12.25-4-50S, 13.5-0-50S
	FS23 $[0]_{80}$	5 mm/min	DIC Only
	F60_1 $[0]_{60}$	5 mm/min	DIC Only
	F60_2 $[0]_{60}$	5 mm/min	DIC Only
	F60_3 $[0]_{60}$	5 mm/min	DIC Only
	F40_1 $[0]_{40}$	5 mm/min	DIC Only
	F40_2 $[0]_{40}$	5 mm/min	DIC Only
	F40_3 $[0]_{40}$	5 mm/min	DIC Only
	F20_1 $[0]_{20}$	5 mm/min	DIC Only
	F20_2 $[0]_{20}$	5 mm/min	DIC Only
	F20_3 $[0]_{20}$	5 mm/min	DIC Only
Cross-ply Cantilever	FS24 $[0/90]_{20s}$	5 mm/min	DIC Only
	FS25 $[0/90]_{20s}$	5 mm/min	DIC Only
	FS26 $[0/90]_{20s}$	5 mm/min	DIC Only

Notes:
1. The samples are not listed in the order in which they were tested.
2. The loading rate was increased from 2 mm/min to 5 mm/min in the interest of saving time, as it was found that the rate increase did not affect the results.

The quasi-static flexural bending tests were originally designed to apply an upward displacement until the samples failed. However, due to the limitation on actuator displacement, the 40- and 20-layer samples could not fail, allotting to their increased flexibility. As such, the load-displacement data for these samples does not reach failure, however, the data can still be used to draw conclusions, as will be discussed in CHAPTER 4 (Results and Discussion) and CHAPTER 5 (Conclusions).

3.2.1 Experimental Procedure

The first several samples tested made use of a strain gauge array to capture the strain field on the surface during loading. This procedure did not come without complications. First, the small grid size required for accurately capturing the strains in regions of sharp strain gradients resulted in much difficulty properly applying the gauges. Second, due to stock limitations from the strain gauge supplier, it was not possible to obtain linear gauges with lead wires pre-attached. These would have to be soldered on after bonding the gauges to the sample. Due to the small size of the solder pads, this resulted in much difficulty soldering the lead wires. Third, the number of gauges required to obtain a reasonable representation of the strain field made it such that there were upwards of 30 gauges on some samples, again rendering the gauge application process very difficult and time consuming. These difficulties meant that, when the samples were tested, some gauges debonded, had broken lead wires, or malfunctioned. Therefore, it was decided to investigate DIC for full field strain measurement. This proved to be a more effective and efficient way of measuring strains. Once the gauges or speckle pattern were applied to the sample surface, the following general procedure steps were followed for running the test:

1. The power to the hydraulic pump was powered on and the collar was removed from the actuator.
2. The sample was placed on the test setup with steel clamping plate in place and the bolts at the fixed end were tightened until finger tight.
3. With the actuator low enough so that the loading fixture was not in contact with the sample, the strain gauges were zeroed or a reference DIC image was taken, as applicable. At the same time, the load cell of the actuator was zeroed.
4. With the help of a square to ensure proper alignment of the sample to the test setup, the bolts at the fixed end were then torqued in a cross pattern to 110 ft-lbs. Another DIC image or strain gauge reading was taken at this point. For samples employing DIC, the previous images were analyzed to verify that no rotation of the sample occurred during the tightening of the bolts.
5. The actuator was moved up until the fixture barely contacted the sample. The steel clamping block (for clamped) or top part of the cantilever fixture was placed on top of the sample and the bolts

were tightened on the loaded end. For the clamped sample, the bolts were torqued to 110 ft-lbs. For the cantilever sample, the bolts were torqued to 42 ft-lbs.

6. At this point the retaining blocks were removed. Then, if the load cell read a non-zero value, the position of the actuator was adjusted until the load was as close to zero as possible, then the displacement transducer of the actuator was zeroed.
7. Another DIC image or strain gauge reading was taken and the corresponding data acquisition system (DAQ) was set to take continuous readings/images during testing.
8. A 5 mm/min loading rate was applied to the sample until the maximum specimen or actuator displacement was reached.

Some important things should be noted about the above procedure. First, for the samples with a strain gauge array, due to the high number of gauges used and a limited number of ports available on the DAQ, not all the gauges were able to be connected at the same time. In these cases, half of the gauges were connected to the DAQ and the sample was loaded to an actuator extension of 10 mm. Then the load was removed, the other half of the gauges were connected, and the sample was loaded to 10 mm a second time. Finally, gauges which had the highest strain readings were connected for the failure test. The second consideration is that the actuator loading program was setup to end the test if at any point the recorded load dropped below 50% of the maximum recorded load. This was the failure criteria of the test program. Third, since the cantilever fixture clamps the sample between two cylindrical faces, it had the ability to roll around the sample if the bolts were not tightened properly. As will be discussed in more detail in section 4.2.2 (80-Layer Unidirectional Cantilever Configuration), this was the case for samples FS17 and FS18, but was only discovered after these samples failed. Due to the improper tightening of the bolts, the ball joint underwent excessive rotation during loading, skewing the actuator displacement results. This was subsequently corrected for sample FS23. Fourth, as mentioned previously, there was a lot of difficulty in applying some strain gauges due to their small size and the requirement to solder wires to the gauge terminals. This resulted in some malfunctioning gauges. That being said, certain inferences can still be made based on the resulting strain gauge results. This will be discussed further in the following chapter. Finally, once DIC was

employed, is was found that the specimens underwent a slight rotation about the Z-axis while tightening the bolts at the fixed end. This rotation was not visible to the naked eye as it was on the order of an equivalent lateral displacement at the tip of the specimen of a few hundredths of an inch. This resulted in a slight twisting of the sample about the Y-axis while being loaded because the supporting edge of the test fixture did not rest perfectly perpendicular to the X-axis of the sample. This was only discovered after some samples had already been tested. Despite best efforts to mitigate this rotation for subsequent samples, it was not completely avoidable. As such, this may have contributed to some of the discrepancies that will be discussed later between ANSYS predictions and DIC results.

Once the samples were failed, dye penetrant inspection was performed to view the resulting failure cracks. To achieve this, the buffer pads were removed, and the adhesive residue was sanded off to expose the surface cracks. After cleaning the sample surface with alcohol, a low viscosity ink was applied to the surface to enhance visualization of the cracks, and the excess ink was wiped clean. Dye penetrant inspection works through capillary action, where the low surface tension between the ink and the sample surface allows the ink to de drawn into the crack, while the alcohol used to clean the surface does not. When the surface cracks were catalogued, the samples were then sectioned widthwise at 0.75-inch intervals along the length, and the same dye penetrant inspection process was used to visualize the internal cracks. Finally, the failure cracks were modeled in CATIA by extrapolating the crack patterns from one section to the next as surfaces. These will be discussed in section 4.5 (Failure Analysis).

3.2.2 Digital Image Correlation (DIC)

Digital image correlation (DIC) is a non-destructive noncontact method to find in-plane and out-of-plane deformations at the surface of a structure. It is possible to estimate normal and shear strain fields once the full-field deformations are available. DIC is based on the comparison between images which are taken before and after loading. Therefore, the accuracy of the results is highly influenced by the quality of the images. In order to effectively use DIC, an appropriate high contrast speckle pattern should be applied to the target surface. In general, a good speckle pattern has evenly distributed speckles, but the speckle shapes and sizes must be random. To achieve this, an airbrush was used to spray black ink on a white

background that was painted on the target surface. Once the speckle pattern is properly applied, a fixed set of stereo cameras, that are carefully calibrated to each other's position and relative to the target surface, are used to capture images of the speckle pattern. An image of the DIC setup is shown in Figure 3.4.

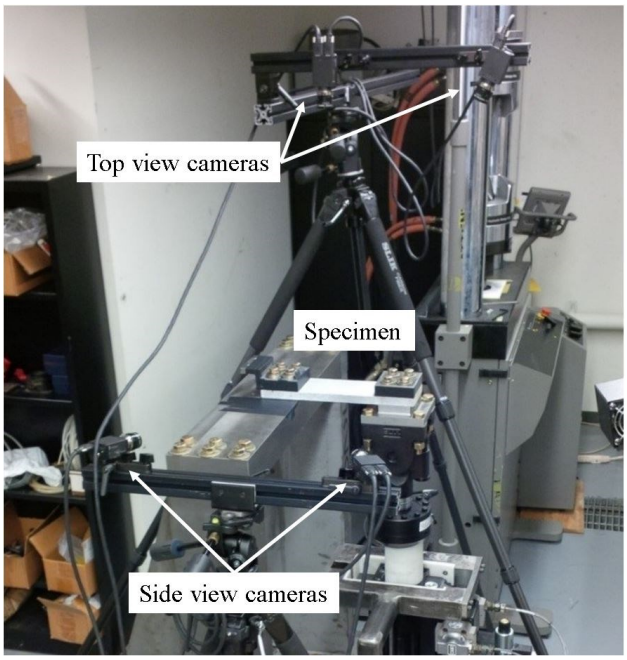

Figure 3.4: Digital image correlation camera setup

To begin capturing data, first, a reference image is taken with no load applied on the sample, then more images are taken at desired load levels. The images are then transferred to an analysis software, where the reference image is divided into square subsets of pixels to keep track of the displacement of the speckles through the series of images. The subset should be just large enough such that an average speckle can be fully contained within the area of the subset square. A step (in terms of number of pixels) is also defined to determine the number of pixels between each displacement calculation point. This is synonymous to the distance between nodes in FEA. The smaller the step size, the finer the strain resolution, but the higher the noise level. Finally, a filter size can be set that dictates the number of steps over which the software averages the strain values for smoothing out noise. The step number multiplied by the filter size determines the diameter (in pixels) of a circle over which the strain is averaged, usually using a 90% weighted Gaussian average. This circle area is synonymous to the mesh size in FEA. Similarly to FEA, where a larger mesh gives a smoother strain calculation, albeit at the expense of strain resolution, a larger circle diameter (step

number multiplied by filter size, in pixels) will also give smoother results with lower strain resolution. For the purpose of this project, there was not enough time to verify if there is a correlation that can be obtained between the circle diameter in DIC and the mesh size used in the FEA of [38]. For the sake of brevity, the best practices in setting up the DIC system and obtaining strain results will not be discussed in this report. Several documents are available through Correlated Solutions in this regard.

3.3 Finite Element Model

A three-dimensional finite element model was created using ANSYS 16.2 software as is described in [38]. The model was made fully parametric using APDL language programming. Therefore, it provides the ability to define and establish further parametric studies, which is a critical asset in the design process. Simulation components and related characteristics were defined to correspond closely to the experimental testing setup in order to predict the structural behavior of the plate (i.e. strain and stress distributions). In this section, some details of the modeling and defined parameters will be reviewed.

3.3.1 Model Geometry

Since the experimental tests consist of the clamped and cantilever configurations, two different models were simulated during finite element analysis. Table 3.2 summarizes the number the components modeled for each of the configurations.

Table 3.2: FEA components of clamped and cantilever models

	Clamped model	**Cantilever model**
1. Bolts	Four at each end (eight total)	Four at fixed end only
2. Washers	Four at each end (eight total)	Four at fixed end only
3. Steel Plate	One at each end (two total)	One at fixed end only
4. Big Buffer Pad	Two at fixed end	Two at fixed end
5. Laminate	One	One
6. Small Buffer Pad	Two at loading end	None

Note: The steel cross-beam at the fixed end of the sample and the adapter for bolting the loaded end of the sample to the actuator were modeled as rigid plates in ANSYS.

Figure 3.5 illustrates the different components created in ANSYS and compares the clamped model with the cantilever one. In simulation, each part was modeled according to the corresponding component in the experimental setup. For the clamped model, two rigid plates were created instead of modeling the whole fixed end cross-beam of the machine and the clamping plate at the top of the actuator to reduce the number of elements, the simulation complexity and running time. For the cantilever model, the fixture at the loading end was not modeled and the displacement was applied directly to the plate. The mechanism of loading will be discussed in section 3.3.5 (Loading Mechanisms). As can be seen in Figure 3.5, the parts were partitioned following a specific pattern, which provides full control on mesh sizing and pattern in different regions. Creating a mesh with overlapping nodes for areas which are in contact with each other improves the accuracy of contact modeling and helps the nonlinear contact analysis to converge faster. Two layup sequences were tested during the experiments and finite element simulation. As a first step, a laminate with a layup sequence of $[0]_{80}$ was considered. For the second case, a laminate with a symmetric cross-ply layup sequence of $[0/90]_{20s}$ was considered.

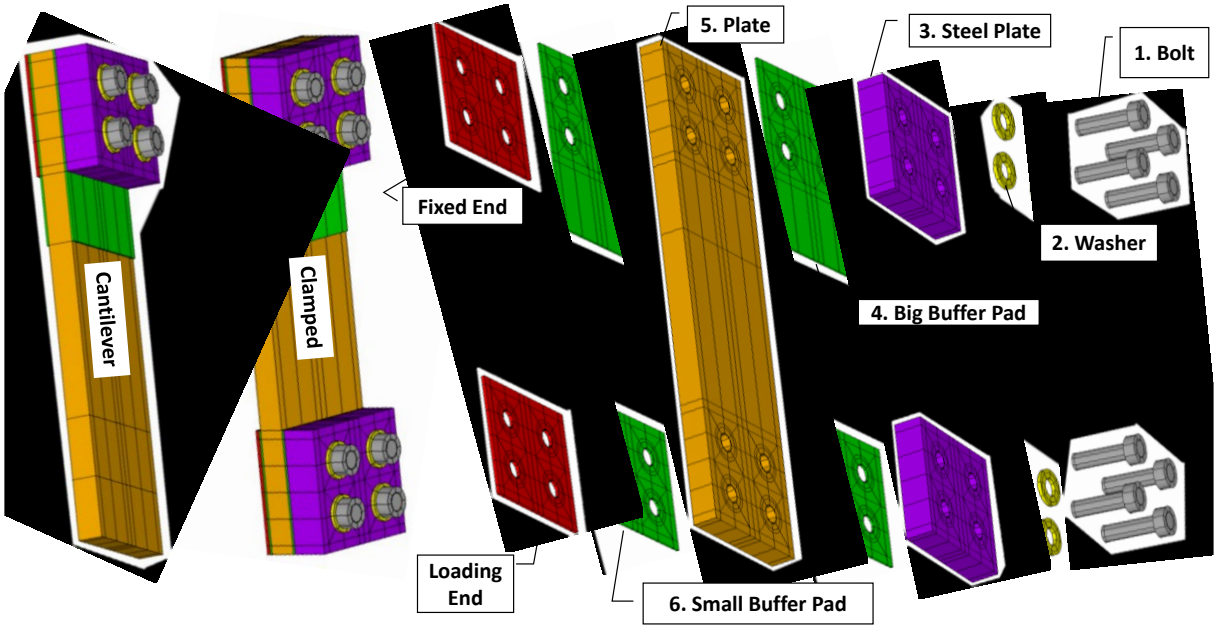

Figure 3.5: Illustration of FEA components [39]

3.3.2 Material Properties

During the first ANSYS iterations, the laminate material properties were not readily available. Experimental tests were performed as part of this project to obtain more precise values [40]. Table 3.3 shows the laminate material properties obtained experimentally compared to those in the ANSYS 16.0 material library and the material supplier's data sheet. The FEA used the experimentally obtained properties wherever possible. The two laminate properties that were not obtained experimentally were taken from the ANSYS 16.0 material library. Table 3.3 also shows the material properties of the washer, bolts, and steel clamping plates, which have the common properties of steel, as well as the properties of the G-7 Garolite buffer pads. In order to model the end plates as rigid, a fictitious material with a stiffness 100 times that of steel was associated with these parts. Solid 186 elements were used to model the washers, bolts, and steel clamping plates. Since the solid element does not have the rotational degrees of freedom, it is not possible to apply the clamping torque directly to the bolt head. As such, the bolt preload was applied as described in the following section.

Table 3.3: FEA material properties

<table>
<tr><th colspan="2" rowspan="2"></th><th colspan="6">Glass/Epoxy</th></tr>
<tr><th>E_1
GPa (Msi)</th><th>$E_2 = E_3$
GPa (Msi)</th><th>ν_{23}</th><th>$\nu_{12} = \nu_{13}$</th><th>G_{23}
GPa (Msi)</th><th>$G_{12} = G_{13}$
GPa (Msi)</th></tr>
<tr><td rowspan="3">Laminate</td><td>ANSYS [41]</td><td>50 (7.25)</td><td>8 (1.16)</td><td>0.4</td><td>0.3</td><td>3.8 (0.56)</td><td>5 (0.73)</td></tr>
<tr><td>Experiment [40]</td><td>47.9 - 51.8
(6.95 - 7.52)</td><td>11.9 - 13.9
(1.73 - 2.01)</td><td>N/A</td><td>0.28</td><td>N/A</td><td>4.27
(0.62)</td></tr>
<tr><td>Data Sheet [42]</td><td>48 - 62
(7 - 9)</td><td>7 - 14
(1 - 2)</td><td colspan="4">N/A</td></tr>
<tr><td colspan="2" rowspan="2">Washer, Bolt and Steel plate</td><td colspan="6">Steel</td></tr>
<tr><td colspan="3">E
GPa (Msi)</td><td colspan="3">v</td></tr>
<tr><td colspan="2" rowspan="2"></td><td colspan="3">200 (29)</td><td colspan="3">0.30</td></tr>
<tr><td colspan="2" rowspan="2">Buffer pads [43]</td><td colspan="6">Garolite (G-7)</td></tr>
<tr><td colspan="3">E
GPa (Msi)</td><td colspan="3">v</td></tr>
<tr><td colspan="2"></td><td colspan="3">11 (1.6)</td><td colspan="3">0.25</td></tr>
</table>

3.3.3 Bolted Joint Considerations

In order to apply the clamping force of the bolts, a pretension section was created in the middle section of the bolt shaft. Element PRETS179 is used in ANSYS to define a pretension section within a meshed structure. The PRETS179 element has one translation degree of freedom which is the defined as pretension direction. At the pretension section, the nodes of the adjacent elements can collapse into each other. Since both sides of the bolt are constrained in the axial direction, the pretension section will provide tension force through the whole shaft. Figure 3.6 illustrates the mechanism of pretension section.

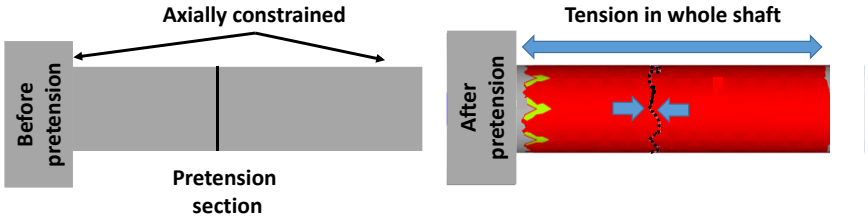

Figure 3.6: Pretension section mechanism

During experimentation, it is more convenient to measure and control the clamping torque (i.e. by torque wrench) instead of the pretension force in the shaft. Therefore, a method should be utilized to convert the clamping torque that was used during experiments to the defined pretension force for the simulation. A very simple method has been introduced by Speck [44]. The proposed relationship between clamping torque and tension force is shown in the following equation:

$$F = T/KD$$

Where T is clamping torque, F is tension force, D is thread pitch diameter and K is a coefficient which depends on the joint characteristics. For steel bolt joints, K can be roughly assumed to be equal to 0.2, but further experiments were required to find the exact value of K for a specific joint. As the bolt joints play the most significant role in the loading and boundary conditions of the aforementioned configurations, finding the proper relation between clamping torque used for experiments and bolt pretension force was a matter of great importance. In addition, because of the flexural deflection of the plate, all bolts do not experience the same tension force throughout the test, even if they were initially torqued to the same value. Therefore, a separate set of experimental tests were performed to find K and to characterize the effect of

the joint position on the bolt tension force after applying flexural bending. For this investigation, a bolt with a force transducer in its shaft was utilized. This special bolt, shown in Figure 3.7, was able to read the tension force in the shaft of the bolt during experiment. To obtain the necessary results, a specimen was fixed to the test setup with one of the bolts replaced by the bolt in Figure 3.7. The sample was then loaded to 10 mm of actuator displacement, and the force readings were recorded. The sample was unloaded, the force transducer bolt was moved to another of the four bolt holes, and the experiment was repeated for each bolt hole. A relationship was acquired between the displacement of the actuator and the load recorded in the bolt. This relationship served as the basis for the load introduced in the bolt during FEA.

Figure 3.7: Bolt equipped with force transducer

3.3.4 Contact Considerations

The buffer pads were made of ultra-high temperature G-7 Garolite. They were made in two different sizes. The big buffer pads (5.5 in x 4 in) were attached to the plate on the fixed end and the small ones (3.5 in x 4 in) were installed only for the clamped configuration at the loading end. The material properties used to model the buffer pads were presented in Table 3.3. Similar to the laminate, the modeled buffer pads were partitioned in a way that full manual control on mesh sizing and meshing pattern would be provided during simulation. In order to reduce the complexity of the model and number of elements, the fixed cross-beam of the testing machine was replaced with a rigid plate in the model. Figure 3.8 illustrates the mesh pattern for different parts of the model. It can be seen that for the areas which are in contact with each other, similar meshes were created with overlapping nodes. The steel and rigid plates are not shown in Figure 3.8, although they were made with the same mesh pattern as the buffer pads and laminate.

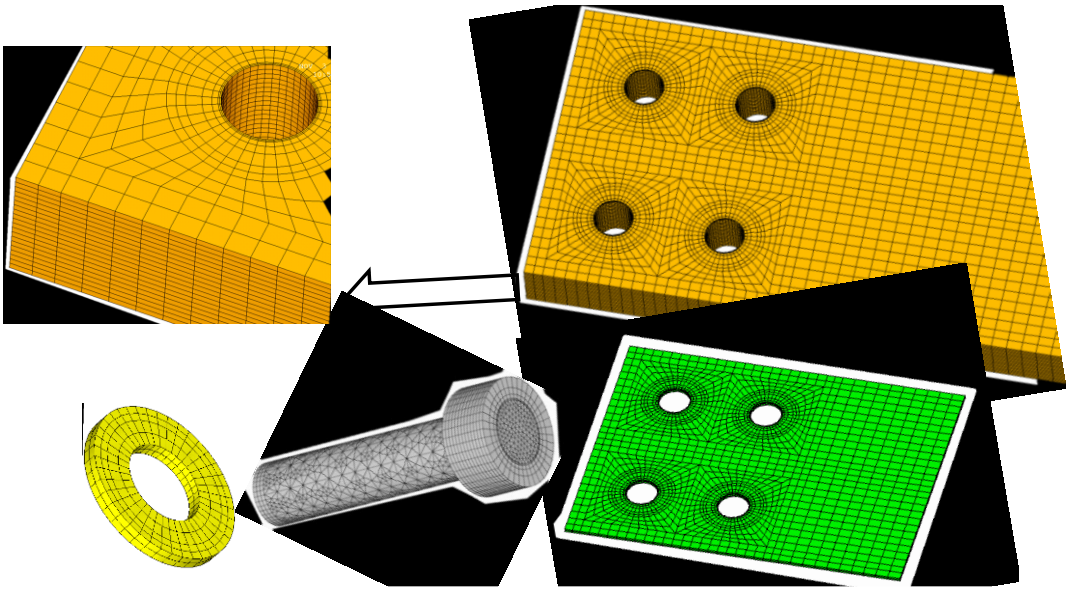

Figure 3.8: Mesh pattern for laminate, buffer pads, washers and bolts (not to scale) [39]

Contact in different regions was defined using surface to surface contact modeling. In this case, it is required to define a contact surface and a target surface. Stiffer and bigger surfaces are normally chosen as target surfaces. In ANSYS, the CONTA174 element is used to simulate contact behavior. Sliding happens between a target surface and a deformable surface defined by contacts elements. The TARGE170 element is used to represent various three-dimensional target surfaces for the associated contact elements [41]. Different contact behaviours can be defined between surfaces. In this simulation, two different contact behaviours were defined according to the characteristics of the existing contact. Between certain parts, a bonded contact was defined, where the nodes of the target and contact surfaces are glued to each other, so no separation or sliding can happen between parts. The other type of contact behavior utilized in this simulation was frictional contact. In frictional contact, separation, collapsing and sliding of contacted surfaces (contact and target) are allowed. Table 3.4 summarizes the type of contact defined between different matting parts.

Table 3.4: Contact behavior definition

	Bolt	Washer	Steel Plate	Buffer Pad	Plate	Rigid Stand
Bolt	-	bonded	-	-	frictional	-
Washer	bonded	-	frictional	-	-	-
Steel Plate	-	frictional	-	frictional	-	frictional
Buffer Pad	-	-	frictional	-	Bonded	frictional
Plate	frictional	-	-	Bonded	-	-
Rigid stand	-	-	-	frictional	-	-

3.3.5 Loading Mechanisms

Modeling the loading mechanism was a challenging endeavor during simulation. As previously described, the actuator has two swivel ball joints at each end. As the hydraulic pressure increases, the piston will extend in the axial direction. As the end of the sample rotates under deflection, the linkage between the specimen and actuator, which remains perpendicular to the sample, causes rotation of the whole actuator around the joint located at the bottom. This interaction for the clamped model is illustrated in Figure 3.9. The simulation of the loading mechanism in the clamped model includes the extension of the piston and rotation of the swivel joints at each end of the actuator.

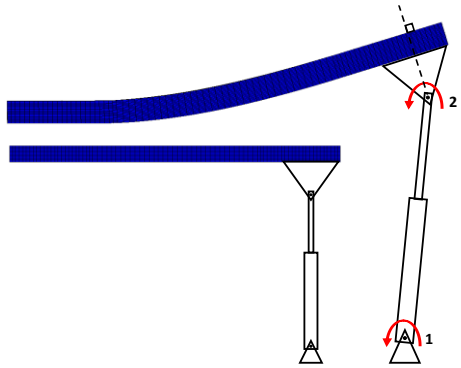

Figure 3.9: The movement mechanism of actuator for the clamped model (not to scale) [39]

Link180 is a three-dimensional spar element that was utilized to simulate the above mechanism. Four rigid links connect the plate's loaded end to the point of the swivel ball joint that is represented as point 2 in Figure 3.9. The triangular part at point 2 in this figure represents the ball joint and adapter plate. As is shown in this figure, the dashed line that passes through the triangle center remains perpendicular to the plate because this region is clamped to the plate by bolted joints and a steel plate. This connection is

shown isometrically in Figure 3.10. The length of the above links was selected to accurately represent the distance between the pivot point of the swivel ball joint and the base of the specimen. To model the actuator's axial extension, a link element was defined with the initial length of the actuator. The material properties of the actuator link, between points 1 and 2 in Figure 3.9 and Figure 3.10, contain only a specific thermal expansion coefficient, acting axially. In this case, by applying an appropriate temperature increment on the actuator link, it is possible to control its axial elongation. It should be mentioned that in real test conditions, the system can control the axial displacement of the piston. In Figure 3.9 and Figure 3.10, point 1 is fixed for translation in all three directions but the actuator link can rotate at both ends.

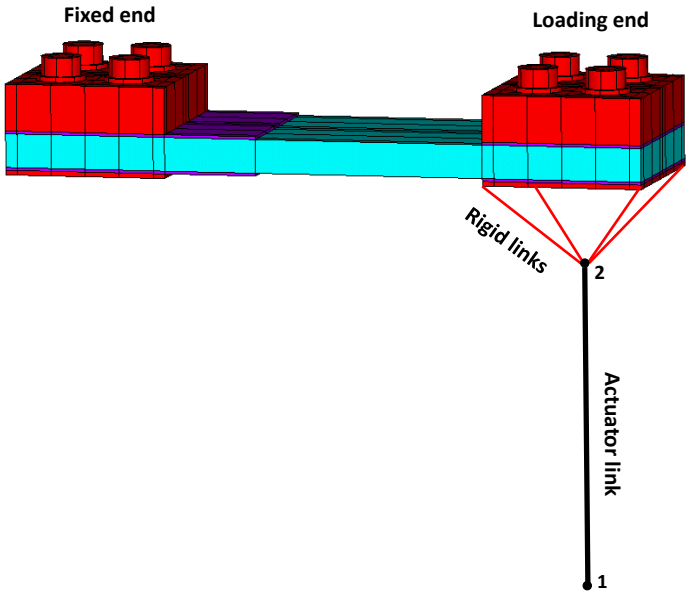

Figure 3.10: Loading mechanism simulation for the clamped model (not to scale) [39]

When modeling the cantilever sample, the configuration of the loaded end was changed. Due to the complexity of the interaction between the cylindrical surfaces of the cantilever test fixture and the surface of the sample, it would be too computationally intensive to model this interaction exactly. Therefore, to reduce the complexity of the model, the loading mechanism at the actuator end was not considered in the finite element simulation and the displacement was applied directly to the sample along a line representing the contact between the bottom cylindrical surface and the specimen. The location of the load line at which the displacement was applied in the cantilever model is shown in Figure 3.11, however, the displacement was in fact applied on the bottom surface of the specimen.

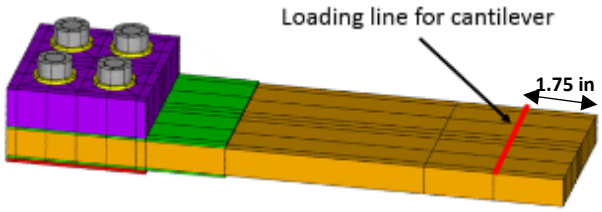

Figure 3.11: Loading line position in cantilever model [39]

3.3.6 Failure Analysis Considerations

A preliminary failure analysis was carried out on a reduced specimen model. Due to the intensive computational requirements for failure analysis, as well as the revelation from experiments that the fixed end is far more critical to failure, the model was reduced to contain the bolted joints and steel clamping plate along with the specimen only up to the edge of the large buffer pads, as shown in Figure 3.12. The deflection of the specimen at the edge of the buffer pads was subsequently input in increments as the displacement in ANSYS. At each load step, the Hashin failure criteria was employed to determine whether an element has failed and by what failure mechanism. If an element failed, its properties were degraded depending on the failure mechanism, and the analysis continued onto the next load step. It should be noted that certain simplifications had to be made due to time constraints. As such, the failure of the ANSYS model does not occur as catastrophically as it did in experiments; it is much more progressive. Therefore, it is not possible to determine the exact displacement where the ANSYS model will fail as it would experimentally. These simplifications and their ramifications are discussed in greater detail in section 4.5 (Failure Analysis).

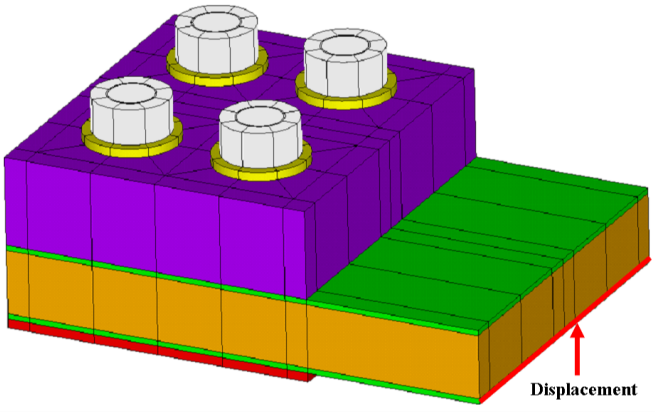

Figure 3.12: Reduced cantilever model for failure analysis

CHAPTER 4 RESULTS AND DISCUSSION

Since the displacement of the actuator is controlled but the displacement of the specimen is of interest, it was important to define a relationship between these two values. The method used for this purpose is described below. It should be noted that this relationship is still just an approximation since it is purely based on geometry. Despite this, the relationship is still required to be able to compare the data to theoretical calculations, ANSYS results, and to be sure that the data that is being analyzed is the most relevant. The remainder of this chapter will present the load vs. specimen displacement data, strain measurements and failure results, while comparing the corresponding data to theoretical estimates and ANSYS model predictions.

4.1 Relationship Between Actuator Displacement and Specimen Deflection

Due to the swivel ball joints and significant rotation of the end of the specimen, the actuator does not remain vertical throughout testing, as illustrated in Figure 3.9. The extent of this rotation is only up to about 2.5 degrees and does not warrant a correction of measured force. However, the deflection of the specimen does not correspond directly to the displacement of the actuator. As such it was necessary to obtain a relationship between actuator displacement and the displacement of a point on the midplane of the specimen at the location of load application. To obtain an approximation of this relationship, the sample was modeled in commercially available CAD software SolidWorks, and a geometric deflection analysis was performed. A schematic representing this relationship is shown in Figure 4.1. The sample was modeled to have 3.5 inches of its length fixed, with the curved portion maintaining tangency to the fixed portion. In the case of the clamped model in Figure 4.1, the last 3.5 inches of the specimen length at the loaded end was made to be straight and remain tangent to the curved portion. The total length of the specimen was fixed at 14 inches. A 4.5-inch link representing the loading fixture and swivel ball joint linkage was made to remain perpendicular to the straight portion of the specimen at the loaded end. In the case of the cantilever model, since the loaded end of the specimen is curved, the line representing the ball joint linkage was made to remain perpendicular to a line tangent to the midplane of the specimen at the location of load application.

Finally, a line representing the actuator was attached to the ball joint linkage, with the bottom point of this line fixed according to the actual dimensions of the machine. In Figure 4.1, *D* corresponds to the zero-position length of the actuator (977.9 mm for clamped, 979.4 mm for cantilever), Δ is the applied actuator displacement (in mm), *a* is the resulting angle of rotation from vertical of the actuator, *b* is the resulting angle of rotation from vertical of the ball joint linkage, *h* is the resulting displacement (in mm) of a point on the midplane of the specimen at the location of load application, and *H* is the resulting displacement (in mm) of a point on the midplane at the tip of the specimen. To obtain the relationship, Δ was incrementally increased, and the remaining variables values were recorded. Then the values of *h* were plotted versus Δ in Excel and a polynomial of best fit was obtained such that the R^2 value was 1. The resulting empirical relationship between Δ and *h*, for $\Delta \geq 0$, is shown in Equation 4.1 for (a) the clamped and (b) the cantilever specimen configurations. All displacements mentioned in this chapter refer to the midplane displacement at the point of load application, *h*, as calculated using Equation 4.1, unless otherwise specified.

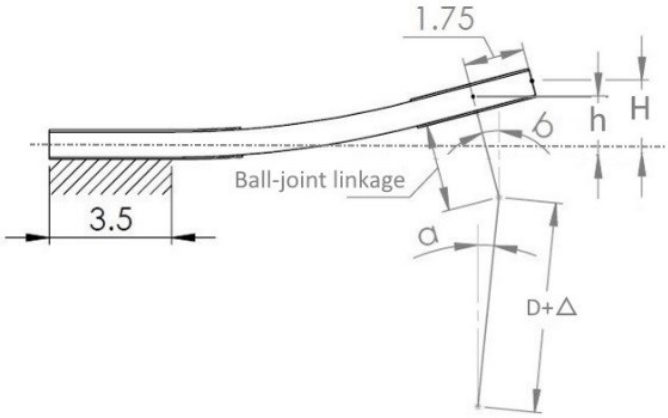

Figure 4.1: Deflected clamped specimen schematic

$$h_{clamped} = (-2.303 \times 10^{-3})\Delta^2 + 0.9738\Delta \quad \text{(a)}$$

$$h_{cantilever} = (1.581 \times 10^{-5})\Delta^3 - (4.1575 \times 10^{-3})\Delta^2 + 0.9847\Delta \quad \text{(b)}$$

for $\Delta \geq 0$ 4.1

Equation 4.1: Empirical relationship for (a) clamped and (b) cantilever configurations between upward actuator displacement, Δ, and specimen midplane deflection at load line, *h*

4.2 Load-Displacement Analysis

As mentioned previously, the actuator is displacement-controlled and equipped with a load cell to measure the axial force in the actuator. It is therefore useful to compare the load-displacement curves between samples to observe the effect of sample configuration and layup sequence on sample behaviour. These results are discussed in the following subsections.

4.2.1 80-Layer Unidirectional Clamped Configuration

The first sample configuration tested was 80-layer unidirectional clamped, as this is the configuration provided initially by the industrial partner, and the testing machine was designed for this purpose. Samples FS3, FS5, and FS22 have this configuration. Figure 4.2 shows the load-displacement curves to failure of these three samples. It should be noted that sample FS3 was made with undersized buffer pads (3.5 inches long instead of 5.5 inches) on the fixed end of the sample as this sample was manufactured before receiving the final configuration from the industrial partner. Table 4.1, below, compares the failure loads and displacements, and slopes of best fit for specimens FS3, FS5, and FS22 to the corresponding average values. The slopes of best fit encompass the entire data set and were not made to pass through the origin, due to the lack of linearity of the data. The equations of the slopes and R^2 values are shown below the corresponding legend entries. Despite the undersized buffer pads on FS3, it is clear from Table 4.1 that the specimens behaved very similarly with little variance in the values shown. Some important things to note about the curves are that, first, there is a slight load drop around the 12-mm mark. This corresponds to the portion of the buffer pads that were not under the clamping block debonding from the sample, resulting in a slight decrease in stiffness. This load drop is not seen in the curve for FS3 due to the lack of buffer pads to debond. Second, the resulting stress concentration at the edge of the fixed support is expected to have caused the progressive failure beginning near the 32-mm mark of the load-displacement curve for FS3. The other samples failed more catastrophically, and as such, do not show the failure load drop as it occurred too quickly for the data acquisition system to capture it before ending the test. However, cracks were heard before final failure in the 25- to 32-mm displacement range for all three samples. Figure

4.2 shows load drops in this range. These cracks likely correspond to the formation of transverse cracks in the XZ-plane, shear out cracks originating from the bolt holes, and/or delamination between the bolt holes. These failure cracks will be discussed further in section 4.5 (Failure Analysis).

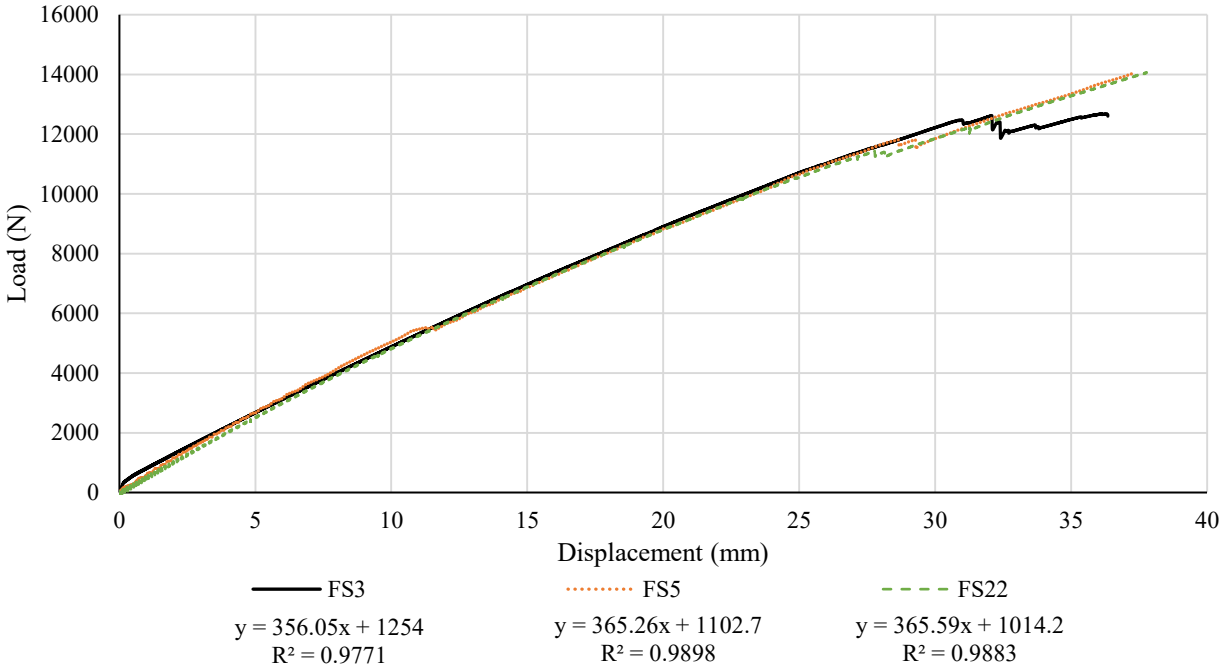

Figure 4.2: Load-displacement curves to failure of 80-layer unidirectional clamped specimens

Table 4.1: Failure loads, displacements, and slopes of best fit for 80-layer unidirectional clamped specimens

		Value	% Difference from Average
FS3	**Load (N)**	12669.9	-6.83
	Displacement (mm)	36.32	-2.20
	Slope (N/mm)	356.05	-1.73
FS5	**Load (N)**	14056.5	3.37
	Displacement (mm)	37.31	0.47
	Slope (N/mm)	365.26	0.82
FS22	**Load (N)**	14068.3	3.46
	Displacement (mm)	37.78	1.73
	Slope (N/mm)	365.59	0.91
Average	**Load (N)**	13598.3	N/A
	Displacement (mm)	37.14	N/A
	Slope (N/mm)	362.30	N/A

An important restriction of classical laminated plate theory, and by extension first-order shear deformation theory, is that the strains and displacements must be small for the calculations to be considered relevant. Also, as can be seen from the relatively low R^2 and high intercept values of the slopes of best fit, the data does not trend linearly. This is mainly due to the increasing effect of shear with increasing thickness causing a nonlinear response in the load-displacement curve of thicker specimens. To better correlate with theoretical calculations, Figure 4.3 shows the average load-displacement curve to 5 mm displacement of the 80-layer unidirectional clamped configuration along with the theoretical load-displacement slopes for an 80-layer unidirectional cantilever specimen, calculated using the modified monodimensional beam theory (MBT) presented in section 1.3 (Theoretical Deflection of a Cantilever Composite Beam), and employing a piecewise approach to account for the discontinuity at the end of the buffer pads. Also included in the graph is the theoretical stiffness calculated by classical laminate theory (CLT), again using the equations from section 1.3, albeit without the shear correction factor. It can be seen from the R^2 value for the experimental results that the data is much more linear when limited to small displacements. The difference in stiffness of the theoretical MBT calculations compared to the experimental results is 35%. When compared to theoretical CLT calculations, the error grows to 104.3%. The oscillation seen in the data of Figure 4.3 is due to the accuracy of the load cell, which is ±50 N. Therefore, over small displacement and low load ranges, the data appears noisy.

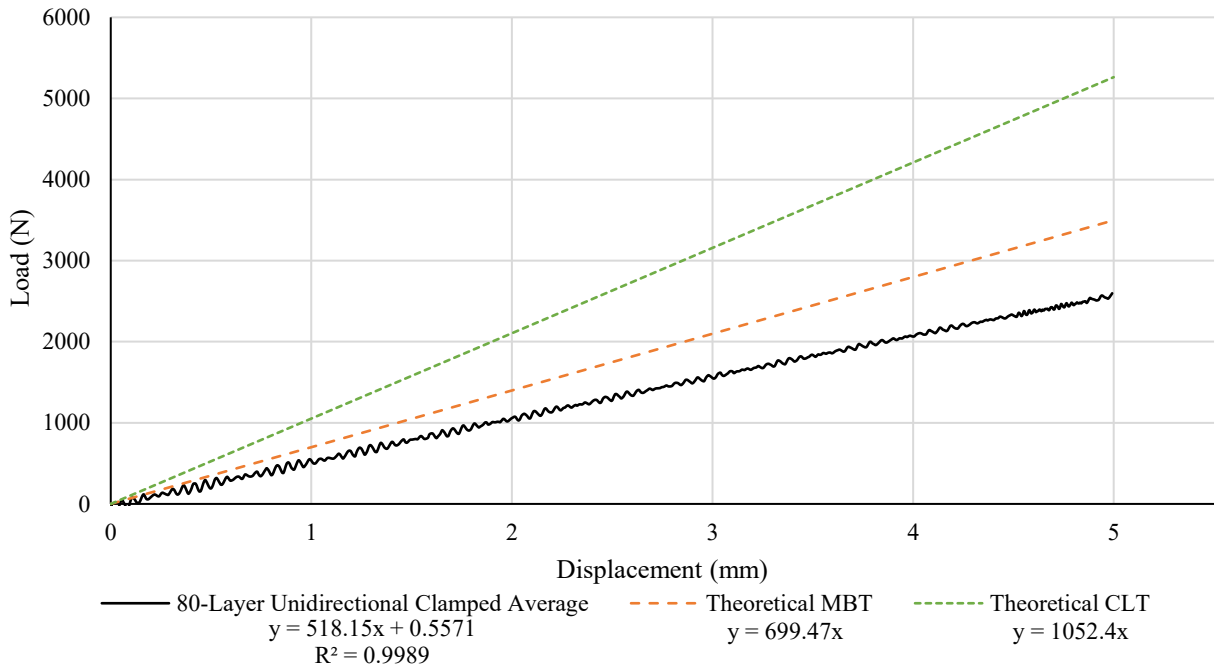

Figure 4.3: Theoretical and average load-displacement curves to 5 mm of 80-layer unidirectional clamped configuration

4.2.2 80-Layer Unidirectional Cantilever Configuration

After testing the unidirectional clamped specimens, and since the clamping of the loaded end makes a mathematical analysis of such a sample very difficult, it was decided that it would be valuable to test unidirectional cantilever samples to assess the influence of clamping the loaded end. Figure 4.4 shows the load-displacement curves to failure for 80-layer unidirectional cantilever samples FS17, FS18, and FS23. Table 4.2 compares their failure loads and displacements, and slopes of best fit to the corresponding averages. It is evident that there is far more variance between these specimens than with the unidirectional clamped specimens. As mentioned in section 3.2.1 (Experimental Procedure), samples FS17 and FS18 did not have the bolts of the loading fixture tightened to the required torque value. As such, the loading fixture underwent excessive rotation during loading, causing the actuator displacement values to be higher than they should for a given load. Despite the slight increase in stiffness expected from clamping the loaded end, the stiffness of the clamped specimens should still be fairly close to that of a unidirectional cantilever specimen. This is seen in Figure 4.5, showing the average load-displacement curve of the unidirectional clamped specimens and that of sample FS23. As such, it is assumed that the data collected for FS23 is

representative of the 80-layer unidirectional cantilever configuration and will be used as the "average" values for this specimen configuration in discussions about results. During the testing of FS23, cracks were heard in the displacement range of 23 to 32 mm.

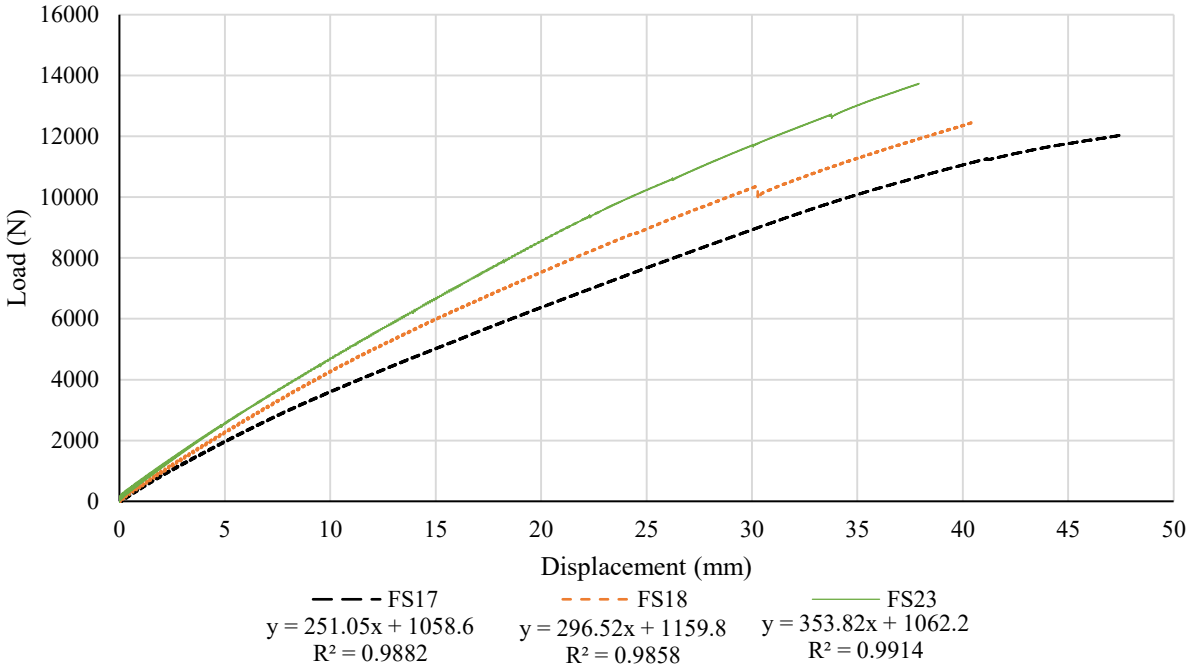

Figure 4.4: Load-displacement curves to failure of 80-layer unidirectional cantilever specimens

Table 4.2: Failure loads, displacements, and slopes of best fit for 80-layer unidirectional cantilever specimens

		Value	% Difference from Average
FS17	**Load (N)**	12036.6	-5.56
	Displacement (mm)	47.42	13.13
	Slope (N/mm)	251.05	-16.45
FS18	**Load (N)**	12458.05	-2.25
	Displacement (mm)	40.41	-3.60
	Slope (N/mm)	296.52	-1.31
FS23	**Load (N)**	13741.2	7.81
	Displacement (mm)	37.92	-9.53
	Slope (N/mm)	353.82	17.76
Average	**Load (N)**	12745.3	N/A
	Displacement (mm)	41.92	N/A
	Slope (N/mm)	300.46	N/A

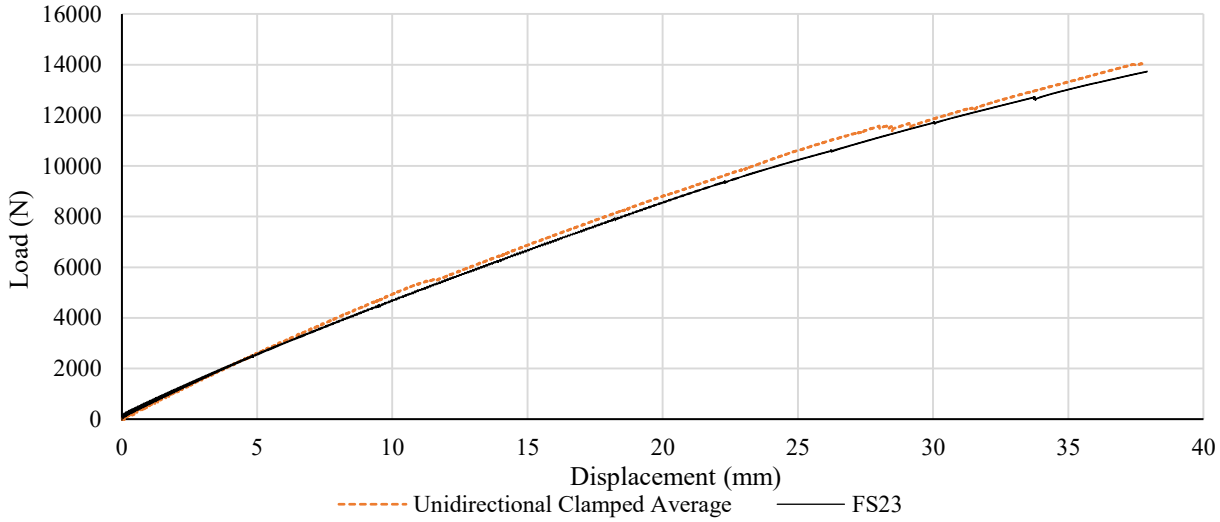

Figure 4.5: Load-displacement curves to failure of FS23 and the average of unidirectional clamped configuration

The load-displacement curve to 5 mm of specimen deflection for FS23 is compared to the theoretical stiffness curves in Figure 4.6. It is clear from the slope values between the clamped configuration in Figure 4.3 and the cantilever configuration in Figure 4.6 that the clamping of the loading end of the specimen results in a slight increase in stiffness (12.35%) at low displacement levels. However, as can be seen in Figure 4.5, this influence seems to reduce at greater displacements as the two specimen configurations approach failure. When comparing the cantilever specimen stiffness at small displacement to the theoretical MBTT and CLT stiffnesses, the difference becomes 51.7% and 128.2%, respectively.

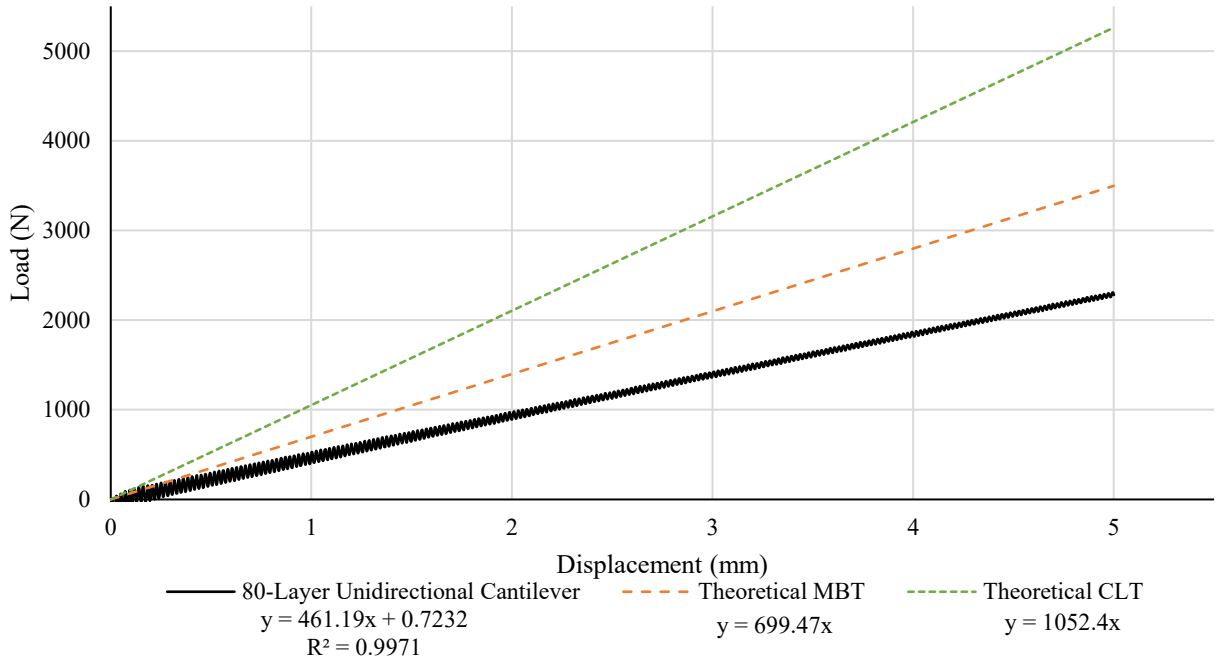

Figure 4.6: Theoretical and average load-displacement curves to 5 mm of 80-layer unidirectional clamped and cantilever configurations

4.2.3 80-Layer Cross-Ply Configuration

To further validate the ANSYS model and for a greater depth of analysis, cross-ply cantilever specimens FS24, FS25, and FS26 were tested. The corresponding load-displacement curves to failure are shown in Figure 4.7. While observing these curves, one might perceive some inconsistent waviness in the data. This waviness is only a result of plotting every 30th data point in an attempt to reduce some of the noise from the load cell data. This noise is clearly shown in the 80-Layer Unidirectional Cantilever curve of Figure 4.6, above. As mentioned previously, the accuracy of the load cell is ±50 N, which results in significant noise over small displacement ranges and at low load levels. If all data points were plotted, all the lines would appear solid, regardless of the line type chosen for visualization, and would be virtually indistinguishable. The failure loads and displacements, and slopes of best fit are compared to the corresponding averages in Table 4.3. During testing, all three samples had the buffer pads debond around the 13-mm mark as evidenced by an audible crack sound. This correlates with the load drop seen in the curve for FS24 in Figure 4.7, although the load drop isn't as evident for the other two samples, partially due to the post-process smoothing of the data. After this, no more cracks were heard until final failure. All

three samples performed almost identically, showing the robustness of the experimental procedure once it was finalized.

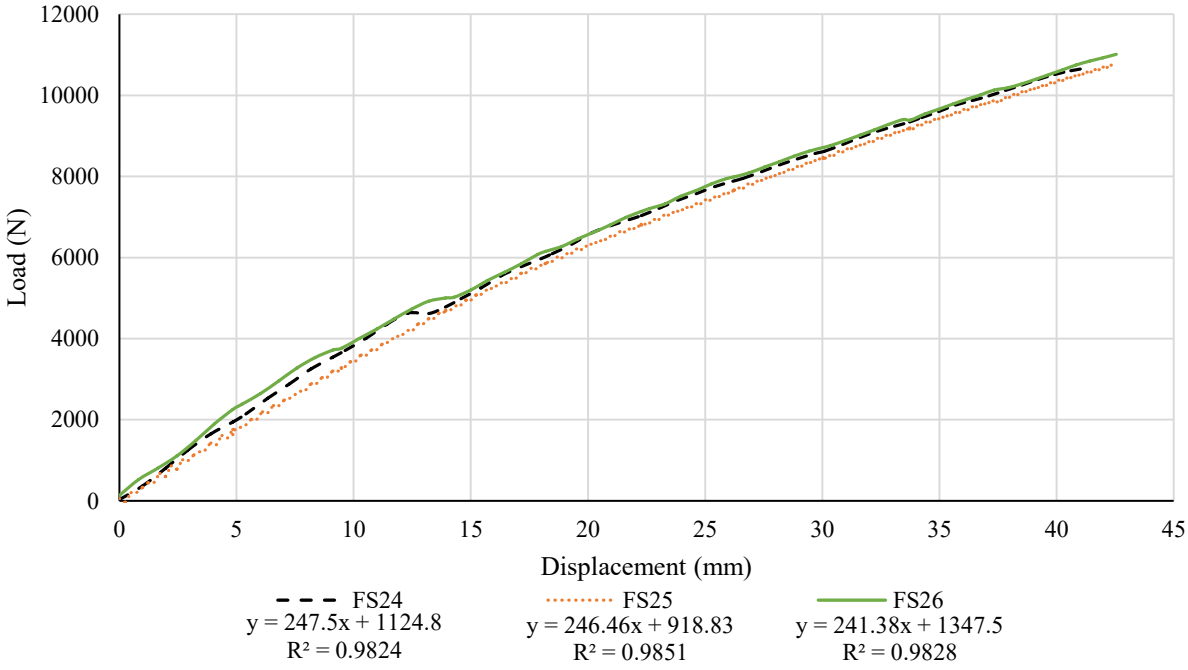

Figure 4.7: Load-displacement curves to failure of 80-layer cross-ply specimens

Table 4.3: Comparison of failure load, displacement, and slope of best fit for 80-layer cross-ply specimens

		Value	% Difference from Average
FS24	**Load (N)**	10769.2	-1.17
	Displacement (mm)	41.63	-1.82
	Slope (N/mm)	247.5	0.974
FS25	**Load (N)**	10797.2	-0.918
	Displacement (mm)	42.6	0.455
	Slope (N/mm)	246.46	0.549
FS26	**Load (N)**	11125.34	2.09
	Displacement (mm)	42.99	1.37
	Slope (N/mm)	241.38	-1.52
Average	**Load (N)**	10897.2	0
	Displacement (mm)	42.41	0
	Slope (N/mm)	245.11	0

Using the equations and method described in section 1.3 (Theoretical Deflection of a Cantilever Composite Beam), it can be shown that a rectangular beam with a layup sequence of $[0/90]_{20S}$ requires a shear correction coefficient k = 1.2973 when also considering the buffer pads. The resulting theoretical MBT stiffness is shown in Figure 4.8 alongside the theoretical CLT stiffness and the average experimental results for the 80-layer cross-ply cantilever configuration up to 5 mm of specimen deflection. Looking at the slopes of the data, the difference between theoretical calculations and experimental results is 17.4% for MBT and 71.8% for CLT. This demonstrates a marked improvement over the 51.7% error in theoretical MBT calculations for the 80-layer unidirectional cantilever configuration.

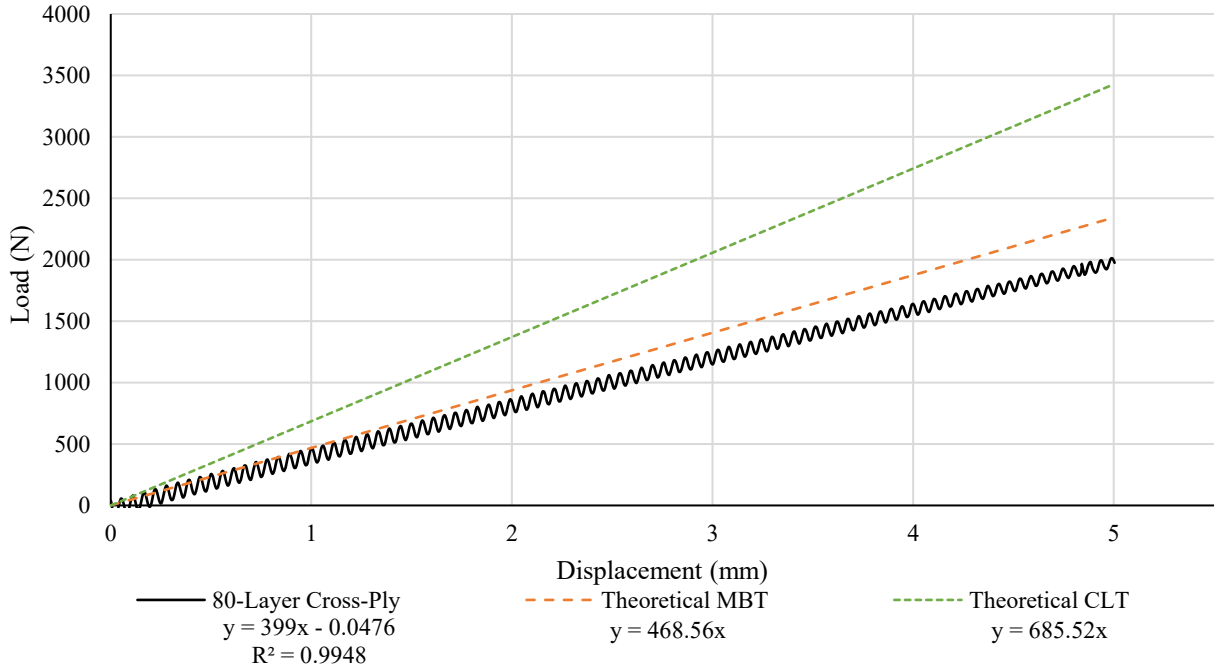

Figure 4.8: Theoretical and average load-displacement curves to 5 mm of 80-layer cross-ply configuration

4.2.4 60-Layer Unidirectional Configuration

To round out this study, unidirectional cantilever samples of 20, 40, and 60 layers were tested to observe the effect of increasing thickness. Figure 4.9 shows the load-displacement curves to failure of the 60-layer unidirectional specimens. Table 4.4 compares the failure loads and displacements, and slopes of best fit to the corresponding average values of these specimens. It is interesting to note that these samples did not fail as catastrophically as the 80-layer samples, as demonstrated by the multiple load drops seen in

Figure 4.9 after the 40-mm mark. Because of this, the slopes of best fit include only the data up to the first significant load drop around the 41-mm mark. Although F60_2 and F60_3 were able to continue carrying some load after this point, the load drop signifies the formation of a large internal crack, which can be considered final failure of the specimen. As such, this load and displacement are reported in Table 4.4 as the ultimate values. Therefore, ignoring the progressive-type failure of these two specimens, all three 60-layer specimens performed very similarly. As mentioned previously, the perceived waviness in the data is a result of attempting to smooth out the load cell noise to make the curves distinguishable.

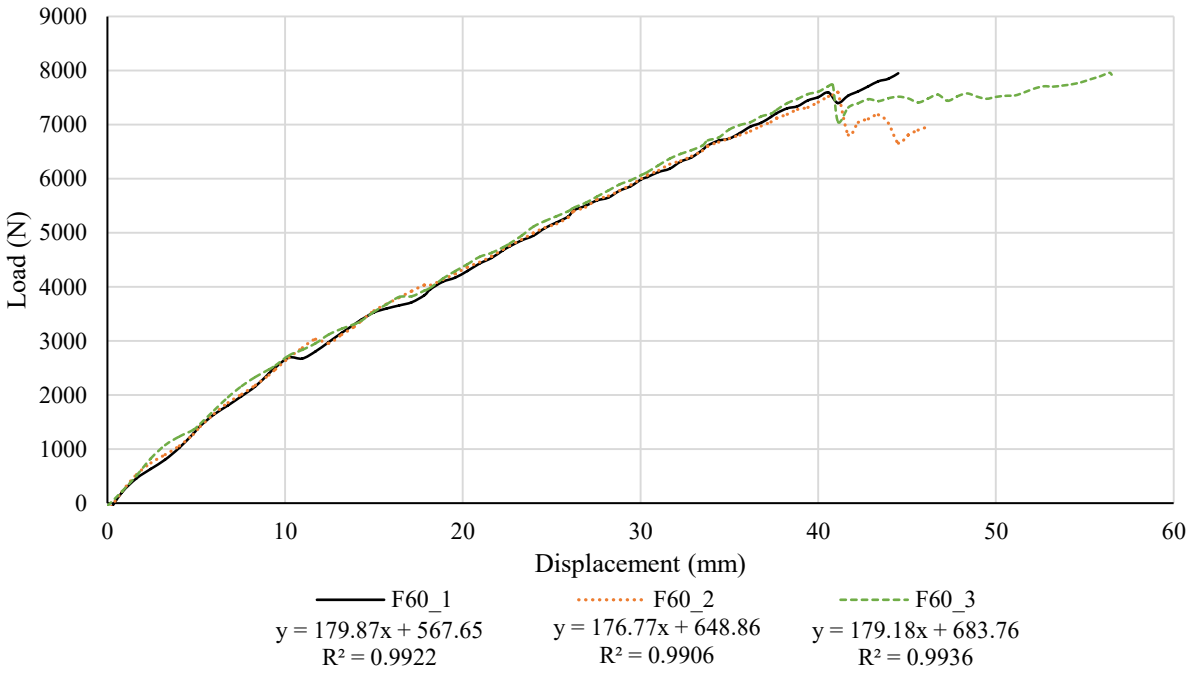

Figure 4.9: Load-displacement curves to failure of 60-layer unidirectional specimens

Table 4.4: Comparison of failure load, displacement, and slope of best fit for 60-layer unidirectional specimens

		Value	% Difference from Average
F60_1	**Load (N)**	8008.8	2.52
	Displacement (mm)	44.85	5.61
	Slope (N/mm)	179.87	0.707
F60_2	**Load (N)**	7660.8	-1.93
	Displacement (mm)	41.60	-2.05
	Slope (N/mm)	176.77	-1.03
F60_3	**Load (N)**	7765.5	-0.592
	Displacement (mm)	40.96	-3.56
	Slope (N/mm)	179.18	0.321
Average	**Load (N)**	7811.7	N/A
	Displacement (mm)	42.47	N/A
	Slope (N/mm)	178.61	N/A

Figure 4.10 shows the average load-displacement curve to failure of the 60-layer unidirectional configuration compared to the theoretical stiffnesses. What is interesting to note in this figure is the 'elbow' signifying a sudden change in stiffness around the 12-mm mark that did not appear in the data for the 80-layer configurations. This is where the buffer pads debonded from the sample. All samples tested exhibit this elbow to varying degrees, signifying the change in stiffness in the sample after the influence of the buffer pads is relieved. However, it is most apparent in the thinner samples for two reasons. First, the portion of the load-displacement curve after buffer pad debonding is more linear for the thinner samples due to reduced influence from shear properties. Second, the added stiffness of the buffer pads represents a greater portion of the total stiffness of the sample for thinner specimens. Figure 4.11 shows the average load-displacement curve to 5 mm of the 60-layer unidirectional configuration compared to the theoretical stiffnesses calculated by MBT and CLT. No data smoothing was implemented in Figure 4.11, so the load cell noise is very apparent. The resulting difference between experimental results and MBT calculation is 10.2%. The difference becomes 61.6% when comparing experimental results to CLT calculation.

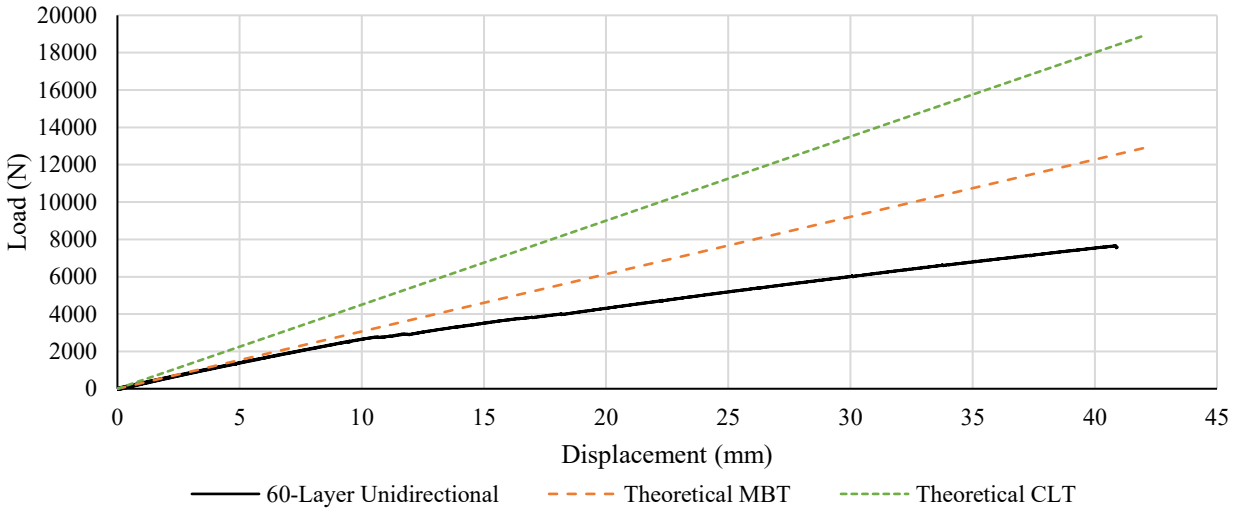

Figure 4.10: Theoretical and average load-displacement curves to failure of 60-layer unidirectional configuration

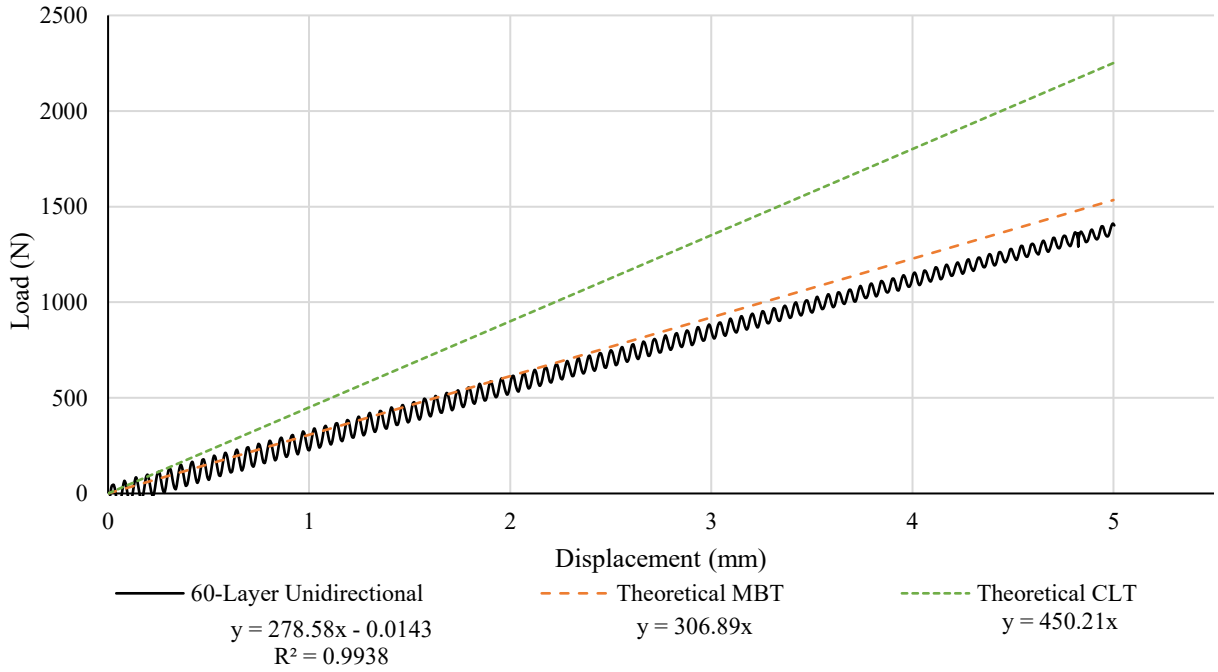

Figure 4.11: Theoretical and average load-displacement curves to 5 mm of 60-layer unidirectional configuration

4.2.5 40-Layer Unidirectional Configuration

Due to physical limitations of the test setup, as explained in section 3.2 (Test Specifications and Procedure), the 40-layer samples were unable to reach failure. However, certain inferences can be made from the data at lower displacement levels. Figure 4.12 shows the load-displacement curves of the 40-layer unidirectional samples up to 50 mm of deflection. As with some of the previous graphs, the perceived

waviness in the data is a result of data smoothing to make the lines distinguishable. Table 4.5 compares the loads at 50 mm of specimen deflection and slopes of best fit to the corresponding average values of these specimens.

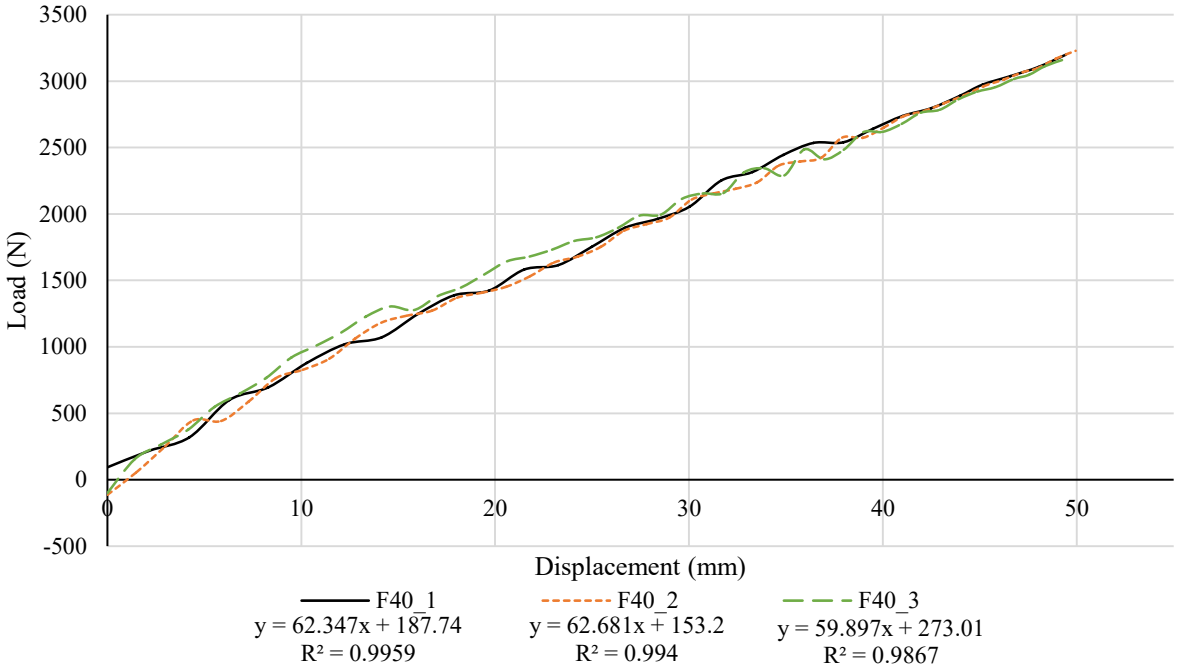

Figure 4.12: Load-displacement curves to 50 mm deflection of 40-layer unidirectional specimens

Table 4.5: Comparison of load at 50 mm displacement and slope of best fit for 40-layer unidirectional specimens

		Value	% Difference from Average
F40_1	**Load (N)**	3217.67	0.3664
	Slope (N/mm)	62.347	1.1442
F40_2	**Load (N)**	3211.78	0.1828
	Slope (N/mm)	62.681	1.6861
F40_3	**Load (N)**	3188.31	-0.5492
	Slope (N/mm)	59.897	-2.8303
Average	**Load (N)**	3205.92	N/A
	Slope (N/mm)	61.642	N/A

Figure 4.13 shows the average load-displacement curve to 50 mm compared to the MBT and CLT theoretical stiffnesses of the 40-layer unidirectional configuration. The loss in stiffness due to buffer pad debonding is clearly marked by the elbow in the curve at the 15-mm mark. Figure 4.14 shows the same data restricted to 5 mm. The difference in theoretical MBT calculation compared to experimental results is 8.2%. The difference between CLT calculation and experimental results is 53.2%.

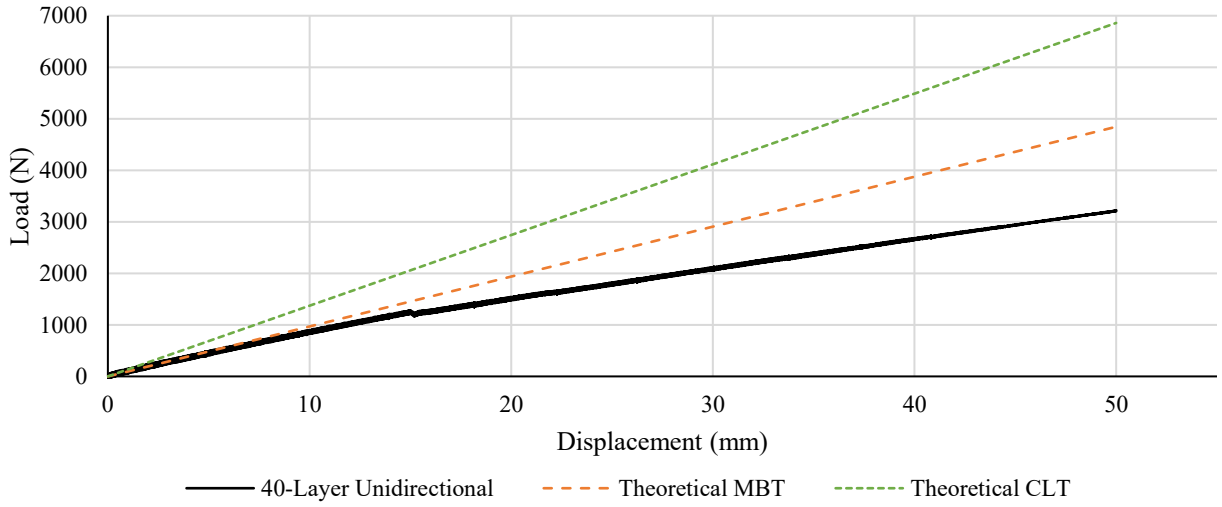

Figure 4.13: Theoretical and average load-displacement curves to 50 mm of 40-layer unidirectional configuration

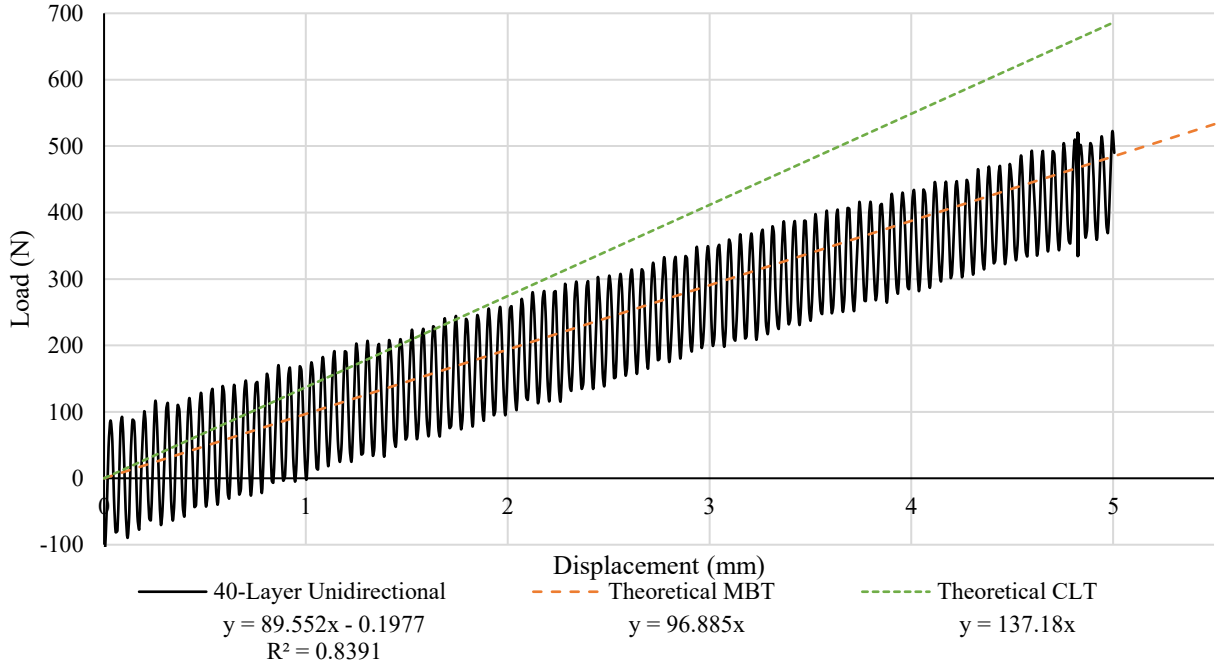

Figure 4.14: Theoretical and average load-displacement curves to 5 mm of 40-layer unidirectional configuration

4.2.6 20-Layer Unidirectional Configuration

Due to physical limitations of the test setup, the 20-layer samples did not fail. However, looking at the slopes of best fit of all three 20-layer unidirectional samples up to 50 mm of specimen deflection, shown in Figure 4.15, it is clear all three samples performed very similarly. Table 4.6 compares the slopes of best fit and the load at 50 mm of displacement between all three 20-layer unidirectional samples and the corresponding averages for further validation. Figure 4.15 only shows the slopes of best fit of the load-displacement data for all three 20-layer samples without the actual data points because the oscillation in the load cell data at this load range results in the curves being indistinguishable, and it was not possible to smooth out the noise to end up with something representative.

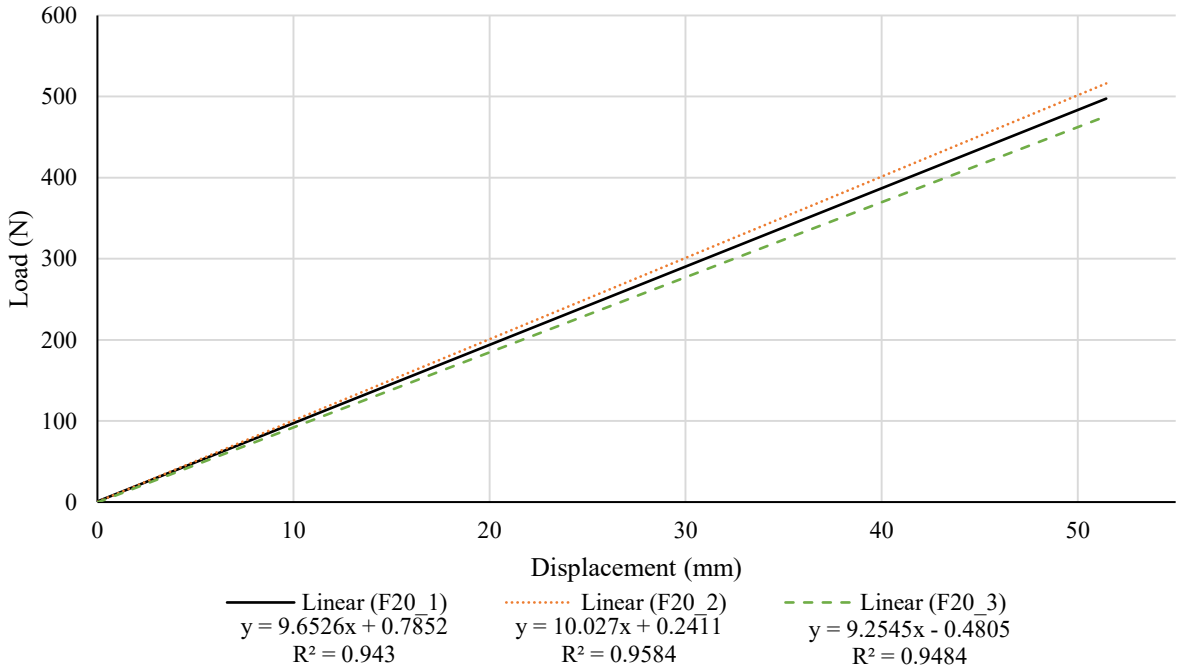

Figure 4.15: Load-displacement curves to 50 mm of 20-layer unidirectional specimens

Table 4.6: Comparison of load at 50 mm displacement and slope of best fit for 20-layer unidirectional specimens

		Value	% Difference from Average
F20_1	**Load (N)**	474.03	2.317
	Slope (N/mm)	9.653	0.086
F20_2	**Load (N)**	469.38	1.319
	Slope (N/mm)	10.027	3.965
F20_3	**Load (N)**	446.49	-3.629
	Slope (N/mm)	9.254	-4.051
Average	**Load (N)**	463.30	N/A
	Slope (N/mm)	9.645	N/A

Figure 4.16 shows the average load-displacement curve to 5 mm of the 20-layer unidirectional configuration alongside the MBT and CLT theoretical stiffnesses. It should be noted that friction in the actuator produces the apparent increased stiffness in the data range from 0 to 1 mm, charted in grey to provide contrast with the rest of the data range. To properly compare the theoretical estimates to the stiffness of the 20-layer samples without considering the effect of the actuator friction, the slope of best fit in Figure 4.16 was made to only include the data from 1 to 5 mm. The resulting difference between theoretical MBT and experimental stiffness is 9.15%. The difference becomes 42.9% when comparing experimental results to CLT calculation.

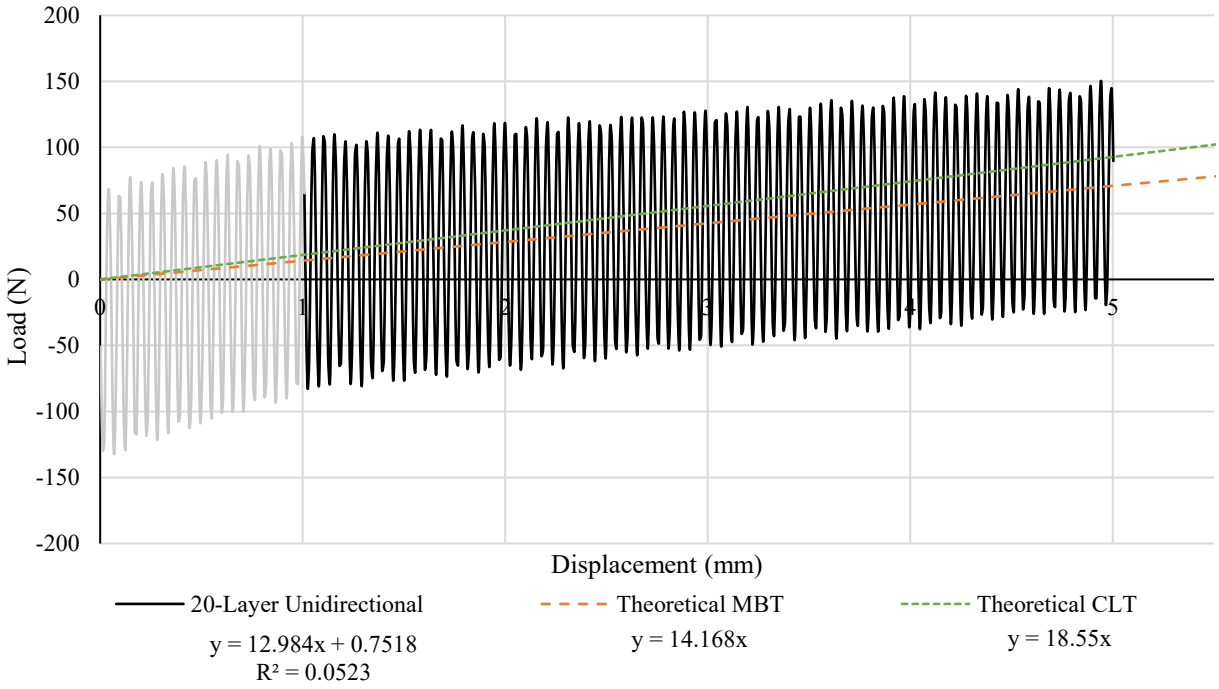

Figure 4.16: Theoretical and average load-displacement curves to 5 mm for 20-layer unidirectional configuration

4.2.7 Load-Displacement Comparison Between Configurations

Figure 4.17 below shows the average load-displacement curves for each 80-layer specimen configuration. Table 4.7 compares the failure loads, displacements, and slopes of best fit of each specimen type to the 80-layer unidirectional cantilever configuration. It is evident from Figure 4.17 that both unidirectional configurations behave almost identically, further confirmed by the numbers in Table 4.7. However, as to be expected, the cross-ply sample is about 30% less stiff, failing at a load that is 20% lower and a displacement that is 12% higher than the unidirectional cantilever configuration. For more insight, Table 4.8 lists the slopes of best fit up to 5 mm displacement for all three 80-layer specimen configurations along with the corresponding theoretical values and the associated percent differences. In all three cases, the theoretical estimates over-predict the specimen stiffness, however, the unidirectional configurations suffer much larger differences with their corresponding theoretical stiffnesses.

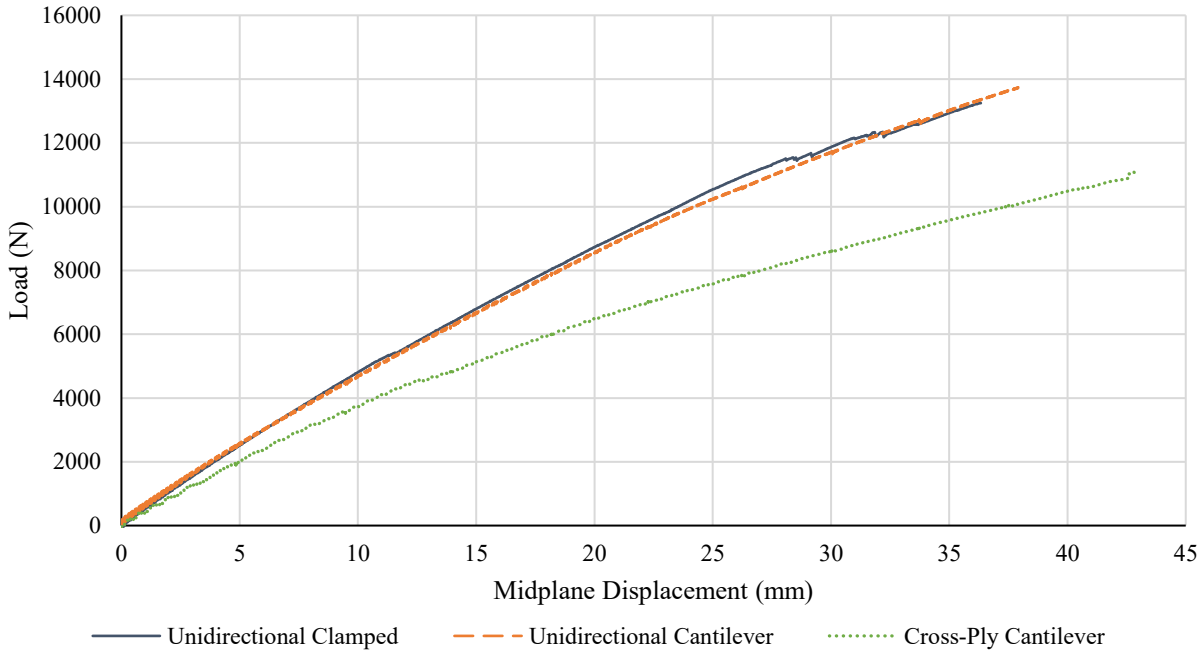

Figure 4.17: Average load-displacement curves to failure for each 80-layer specimen type

Table 4.7: Comparison of average failure load, displacement, and slope of best fit of each 80-layer specimen type

		Value	% Difference from Cantilever
Unidirectional Cantilever	**Load (N)**	13741.2	N/A
	Displacement (mm)	37.92	N/A
	Slope (N/mm)	353.82	N/A
Unidirectional Clamped	**Load (N)**	13598.3	-1.04
	Displacement (mm)	37.14	-2.06
	Slope (N/mm)	362.30	2.40
Cross-ply Cantilever	**Load (N)**	10897.2	-20.70
	Displacement (mm)	42.41	11.84
	Slope (N/mm)	245.11	-30.72

Table 4.8: Comparison of experimental and theoretical specimen stiffnesses to 5 mm displacement of all 80-layer configurations

	Experimental	Theoretical MBT	% Difference MBT	Theoretical CLT	% Difference CLT
Unidirectional Cantilever	461.19	699.47	51.7	1052.4	128.2
Unidirectional Clamped	518.15	699.47	35.0	1052.4	104.3
Cross-ply Cantilever	399	468.56	17.4	685.52	71.8

To further illustrate the decreasing accuracy of MBT and CLT theory with increasing laminate thickness, Table 4.9 compares the experimental slopes of best fit to 5 mm displacement to the theoretical stiffnesses of the 20, 40, 60, and 80-layer unidirectional cantilever configurations. Comparing the percentage differences in Table 4.9 and also considering that for the 80-layer cross-ply configuration from Table 4.8, the theory tends to be less accurate as specimen longitudinal stiffness increases for both MBT and CLT, regardless of layup sequence. However, for the 80-layer unidirectional cantilever laminate, MBT theory becomes about 2.5 times more accurate than CLT (128.2% difference with experiment for CLT compared to 51.7% difference for MBT). While for the cross-ply configuration, MBT is about 4 times more accurate than CLT (71.8% difference with experiment for CLT compared to 17.4% difference for MBT). The greater improvement in accuracy for the cross-ply configuration could be attributed to the fact that unidirectional laminates are treated as homogenous beams in theory, meaning the shear correction coefficient, when not considering the addition of buffer pads, is always $k = 1.2$, regardless of thickness. This results in a decreased ability to properly capture the shear effect with increasing laminate thickness. Conversely, the theoretical MBT calculation for the cross-ply configuration takes the laminate thickness into account, providing a more accurate picture of shear influence. It is clear that the theory is more accurate for thinner samples. However, it is interesting to note that the theory is on the same order of accuracy for 20 layers as it is for 40 layers for MBT. This could be due in part to the buffer pad properties that were used to calculate the shear correction coefficient, which were not determined experimentally. The influence of the buffer pads becomes less significant with increasing specimen thickness. As such, if the buffer pad

properties are inaccurate, it will cause a greater discrepancy between theoretical calculations and experimental results for thinner laminates. To illustrate this, Table 4.10 shows again the experimental stiffnesses compared to MBT calculations, albeit with the theoretical estimate calculated assuming the buffer pad properties to be E = 6490 MPa and G = 2596 MPa (as opposed to the original E = 11000 MPa and G = 4400 Mpa), shown in the Theoretical MBT (Modified) column. The %Difference MBT (Modified) column shows the difference between these new theoretical values compare to the experimental values. It can be seen in Table 4.10 that changing the buffer pad properties had the greatest effect on the 20-layer configuration and a decreasing effect as specimen thickness increases.

Table 4.9: Comparison of experimental and theoretical stiffnesses for all unidirectional cantilever configurations

No. Of Layers	Experimental	Theoretical MBT	% Difference MBT	Theoretical CLT	% Difference CLT
20	12.984	14.168	9.14	18.55	42.9
40	89.552	96.885	8.19	137.18	53.2
60	278.58	306.89	10.16	450.21	61.6
80	461.19	699.47	51.7	1052.4	128.2

Table 4.10: Comparison of experimental and theoretical stiffnesses for all unidirectional cantilever configurations, assuming modified buffer pad properties

No. Of Layers	Experimental	Theoretical MBT (Modified)	% Difference MBT (Modified)
20	12.984	12.978	-0.016
40	89.552	91.998	2.72
60	278.58	296.29	6.36
80	461.19	681.30	47.8

To illustrate the size effect as it relates to composite plates in bending, we can compare how the failure displacements change with increasing specimen thickness. Figure 4.18 shows the average failure

displacements for the 40, 60, and 80-layer cantilever configurations taken from the previous sections. The 80-layer cross-ply configurations is added for comparison. It is important to note that since the 40-layer configuration never reached failure, the displacement that is charted is the equivalent specimen displacement at the maximum actuator extension, however, it should be understood that the actual failure displacement would be greater than this. Regardless, an exponentially decreasing trend with increasing specimen thickness is clearly visible. The size effect implies that as specimen thickness increases, strength properties decrease. Since strength and stiffness properties are closely related, the fact that failure displacements decrease exponentially with increasing specimen thickness is evidence of the size effect.

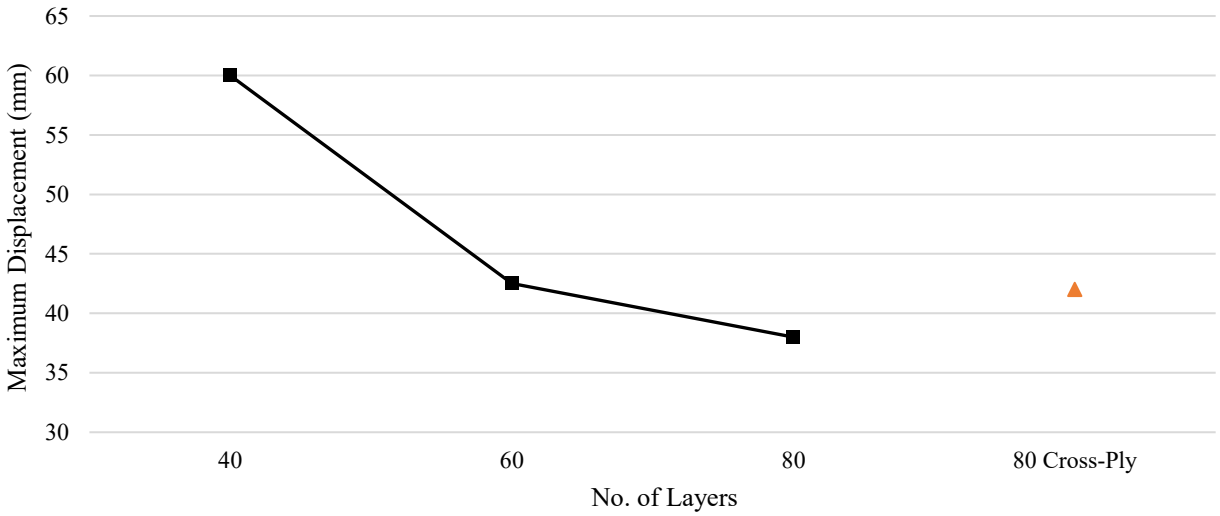

Figure 4.18: Average Maximum Displacement of 40, 60, 80-Layer, and 80-Layer Cross-Ply Cantilever Configuration

4.3 Strains Analysis at 9.45 mm Specimen Displacement

As part of this project, and to validate the ANSYS model created by Gorjipoor [38], the strains were obtained for a simulated actuator displacement of 10 mm, or 9.45 mm of specimen displacement. These simulation results were compared to the strain data recorded experimentally for the same scenario. As can be seen in Table 3.1, all samples tested had either strain gauges or made use of DIC, except FS22 which used DIC and had one stacked T-gauge at a position of X = 3.025 inches, Y = 0 inches, and Z = 50% of the thickness. This is the location where a preliminary ANSYS analysis predicted the ultimate shear

strain at 10 mm of actuator displacement. When discussing the data, the strain gauges are labeled according to the description in Figure 4.19, which is simply Figure 3.3 repeated.

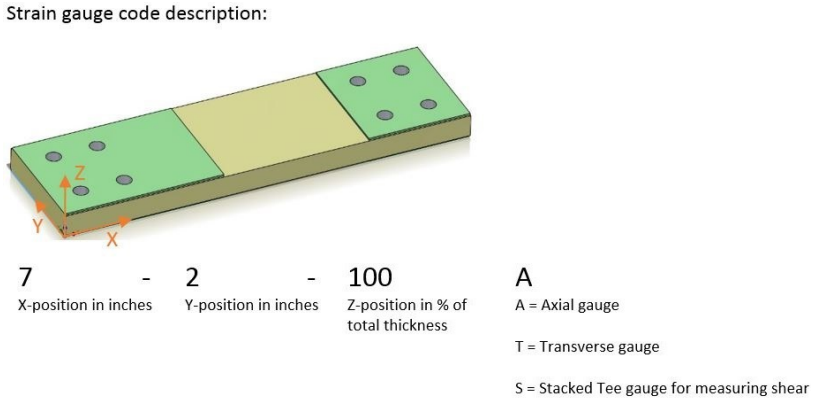

Figure 4.19: Coordinate system and strain gauge code description (Figure 3.3 repeated)

Three types of 80-layer specimens were modeled in ANSYS: unidirectional clamped, unidirectional cantilever, and cross-ply cantilever. For each of the models, two main areas were considered for comparison between strain measurements and predictions. Figure 4.20 (Figure 2.16 repeated) shows the areas of interest, the first one being on the top side of the plate (compression side) from the edge of the large buffer pads to an X-position of 9 inches on the sample, and the second area on the thickness side, around the expected location of ultimate shear strain.

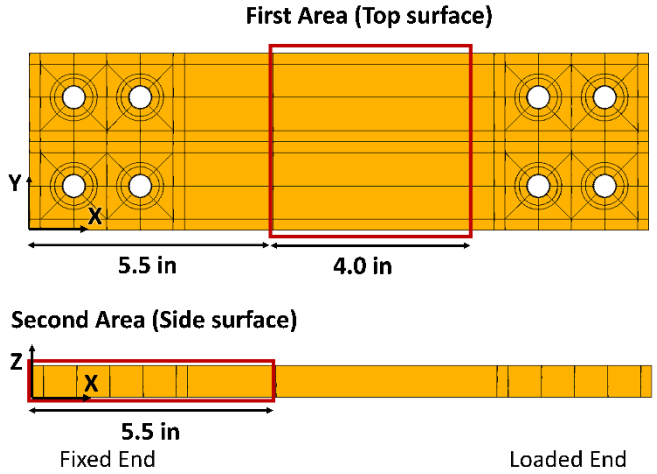

Figure 4.20: Areas of interest for comparison between DIC and ANSYS results (Figure 2.16 repeated)

4.3.1 80-Layer Unidirectional Clamped Configuration

4.3.1.1 Top surface

Figure 4.21 shows the top surface out-of-plane displacement, *W*, distributions obtained from ANSYS and DIC of sample FS22. It is clear from this figure that ANSYS correlated very well with the experimental data qualitatively with a very similar displacement distribution obtained from both approaches. To compare the results quantitatively, the distribution of the displacement along line A-B of Figure 4.21, corresponding to a position of Y = 2 inches, was extracted from ANSYS and DIC and is shown in Figure 4.22. The maximum difference between ANSYS and DIC results along line A-B is 11%, which occurs close to X = 10.5 inches.

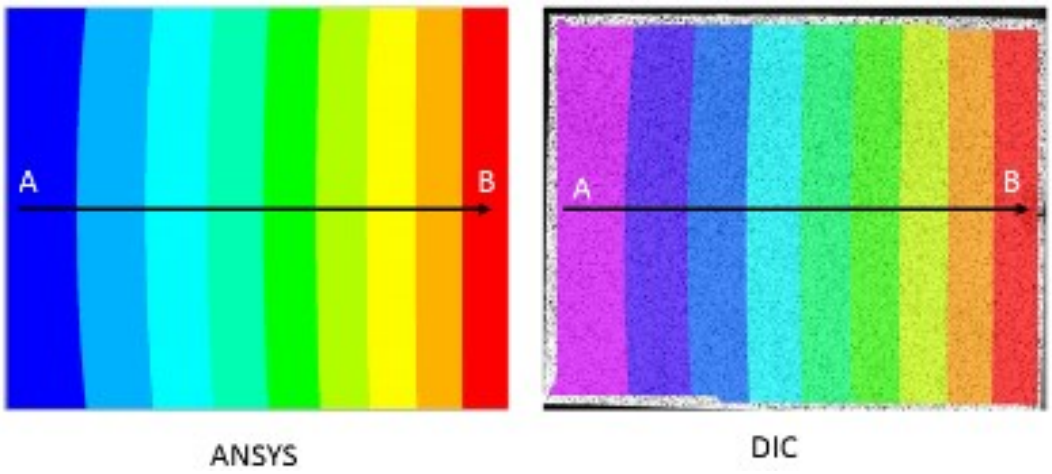

Figure 4.21: Distribution of out-of-plane displacement, W, for 80-layer unidirectional clamped configuration at 9.45 mm displacement

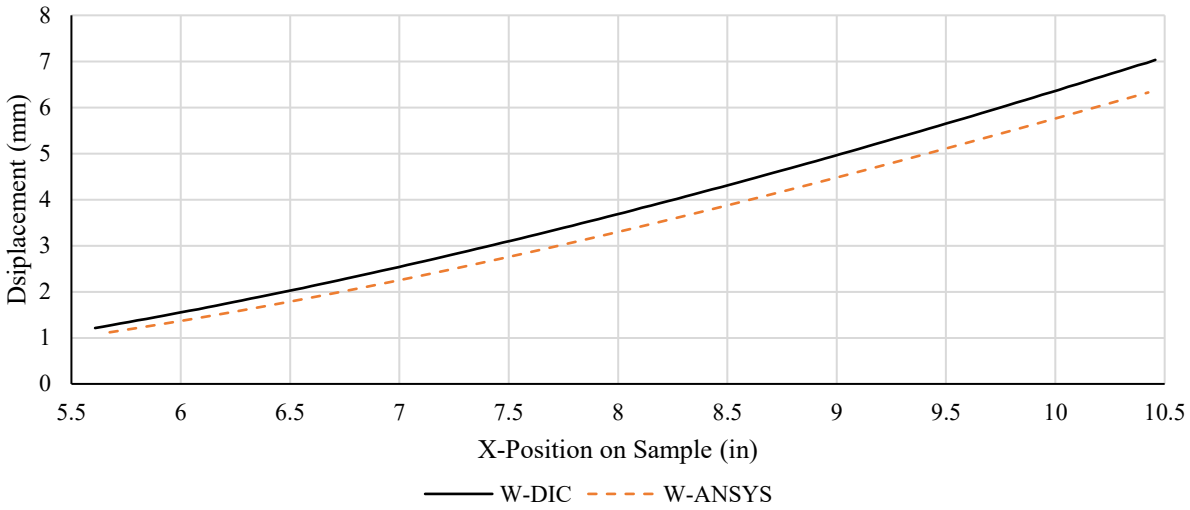

Figure 4.22: Out-of-plane displacement, W, along line A-B of Figure 4.21

The distribution of the top surface axial strain, e_{xx}, is shown in Figure 4.23 for the ANSYS analysis and the DIC results of sample FS22. The distribution of e_{xx} along line A-B of Figure 4.23, corresponding to a line along Y = 2 inches, is compared between the results of ANSYS and DIC in the graph of Figure 4.24. The graph shows a very close correlation between analysis and experiment. The maximum difference was 9% between ANSYS and DIC, found at approximately X = 9.75 inches where the strain values are quite low. The strain gauge results from samples FS3 and FS5 are shown in Figure 4.25 for further comparison. It is clear that the ANSYS results accurately predicted the strains measured on FS5. The discrepancy between FS3 and the ANSYS results can be attributed to the smaller buffer pads on FS3.

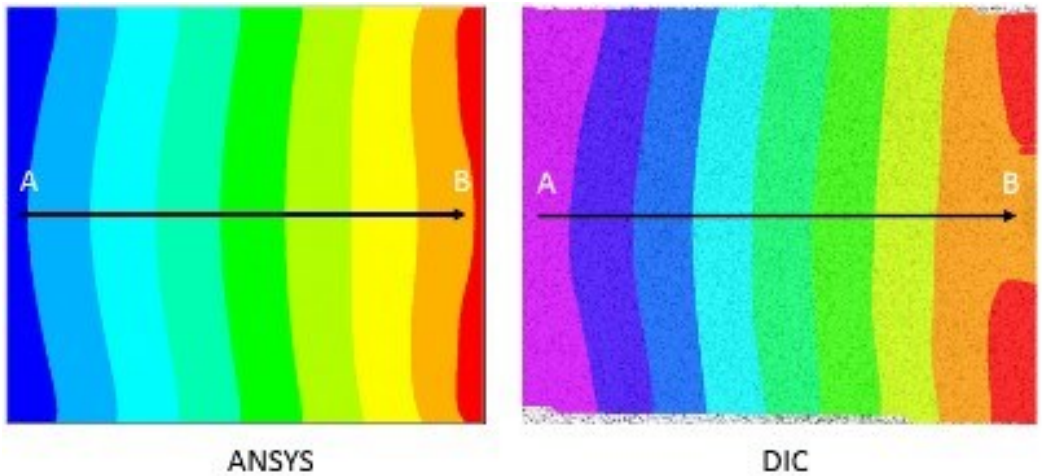

Figure 4.23: Distribution of axial strain, e_{xx}, on top surface of 80-layer unidirectional clamped configuration at 9.45 mm displacement

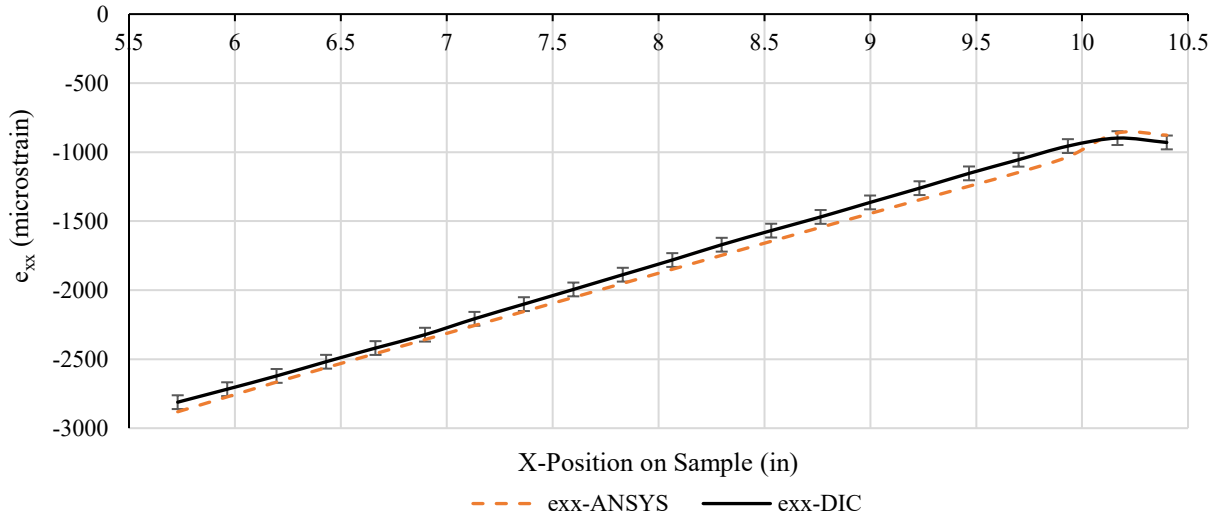

Figure 4.24: Axial strain, e_{xx}, along line A-B of Figure 4.23

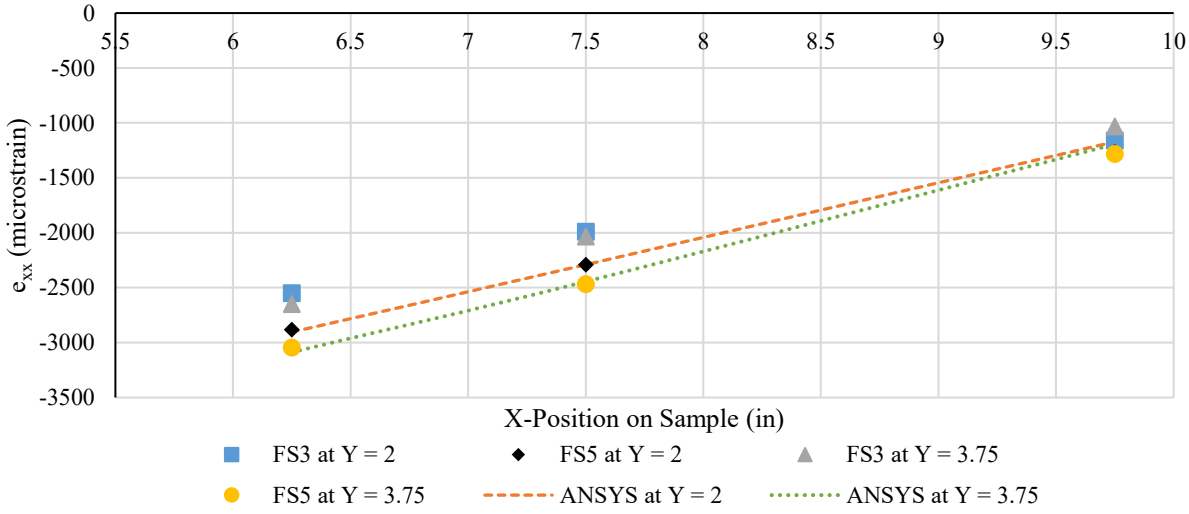

Figure 4.25: Axial strains, e_{xx}, on top surface of FS3 and FS5, measured by stain gauge, compared to ANSYS results at 9.45 mm displacement

The comparisons made in Figure 4.23 to Figure 4.25 were similarly performed for transverse strain on the top surface. Figure 4.26 qualitatively compares the transverse strain, e_{yy}, obtained from DIC on sample FS22 with ANSYS results. As it can be seen, the distribution pattern correlated relatively well between two approaches, despite some asymmetry in the DIC pattern. A quantitative comparison is shown in Figure 4.27 by the comparing the transverse strain distribution along line C-D of Figure 4.26. In this graph, the maximum difference of 146 microstrain occurs at a distance of 3.75 inches along line C-D. Although this equates to a percent difference of about 33%, the accuracy of the DIC system is ±50 microstrain, indicated by the error bars in Figure 4.27. Therefore, at low strain levels such as this, such a

difference should not be considered significant. The transverse strains of FS3 and FS5 as measured by strain gauge are compared to ANSYS data in Figure 4.28. It is interesting to note that the results of FS3 correlated well with ANSYS along Y = 2 inches, while FS5 correlated better with ANSYS along a line at Y = 3.75 inches, which is near the edge of the sample. The discrepancy between strain gauge, DIC and ANSYS results could be attributed to two factors. First, a misalignment of the sample with the supporting edge of the test fixture was discovered after several samples were already tested. DIC results showed that the samples underwent a slight rotation about the Z-axis while tightening the bolts. This meant that the sample did not rest perfectly perpendicular to the support edge. This is evidenced by the asymmetric pattern seen in the DIC image of Figure 4.26, where the hot spot in the top left of the image is not seen symmetrically in the bottom left, and the cold spot on the right is biased towards the bottom half of the image. The second factor potentially contributing to the discrepancy in data is the uneven thickness distribution as evidenced by the higher standard deviation for 80-layer unidirectional clamped specimens seen in Table 2.1. However, this fact was not able to be verified as no samples had perfectly uniform thickness.

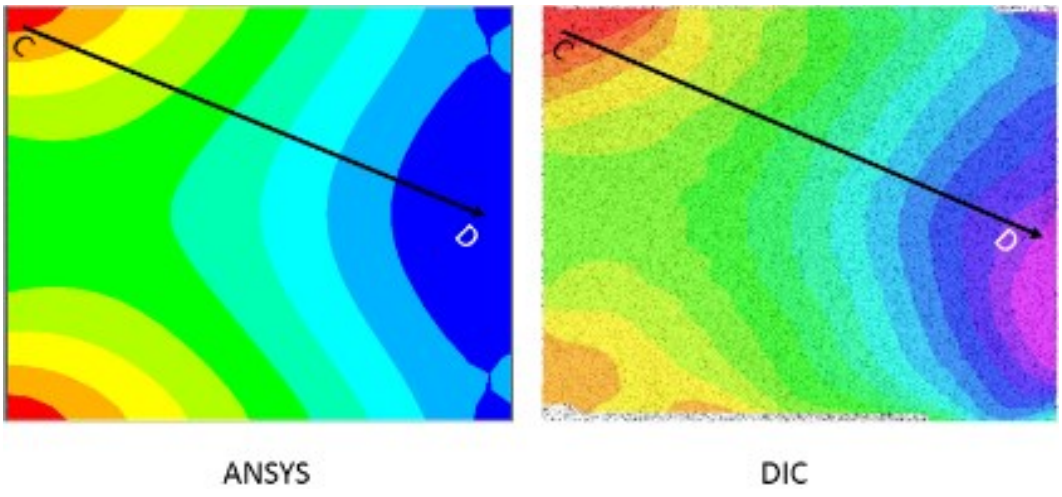

Figure 4.26: Distribution of transverse strain, e_{yy}, on top surface of 80-layer unidirectional clamped configuration at 9.45 mm displacement

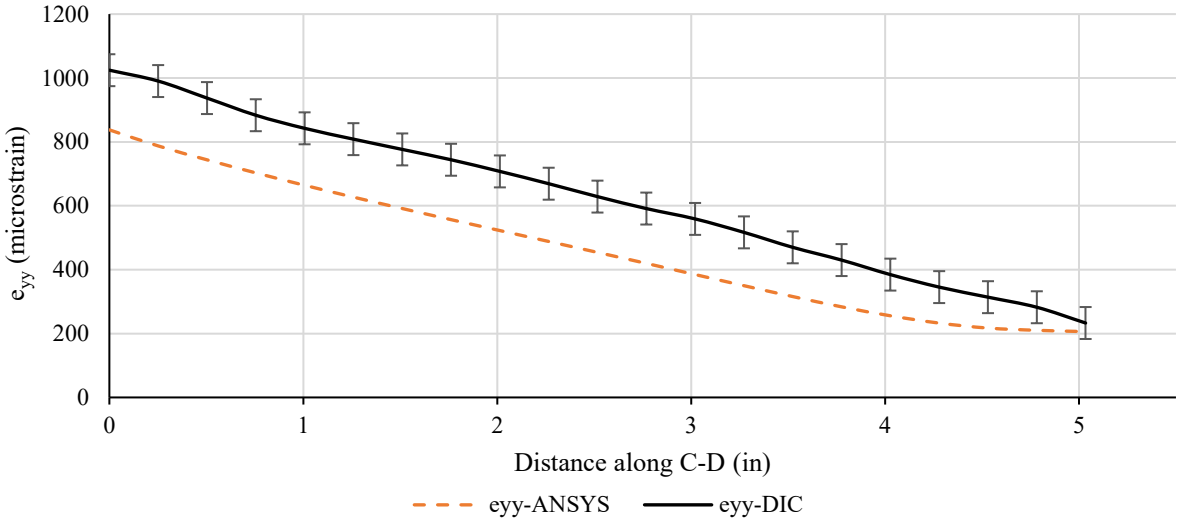

Figure 4.27: Transverse strain, e_{yy}, along line C-D of Figure 4.26

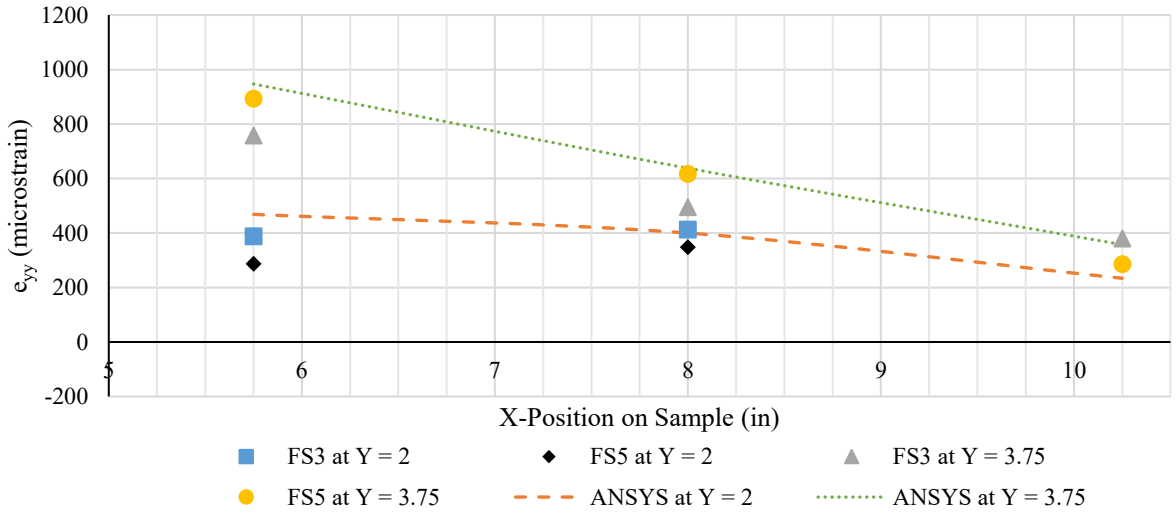

Figure 4.28: Transverse strains, e_{yy}, on top surface of FS3 and FS5, measured by stain gauge, compared to ANSYS results at 9.45 mm displacement

The in-plane shear strain distributions resulting from ANSYS simulation and the DIC measurements of FS22 are shown in Figure 4.29. The resulting distribution along line E-F of Figure 4.29 is shown in Figure 4.30. These figures illustrate that the shear strain distribution and magnitude correlate reasonably well between ANSYS and DIC. Although the transverse and in-plane shear strains obtained from ANSYS both had symmetric distribution, which is expected from the finite element model as per Figure 4.26 and Figure 4.29, some asymmetricities were observed in the corresponding DIC patterns. The difference between ANSYS and DIC at the position of ultimate strains was 2% for e_{xx}, 18% for e_{yy} and 13% for e_{xy}.

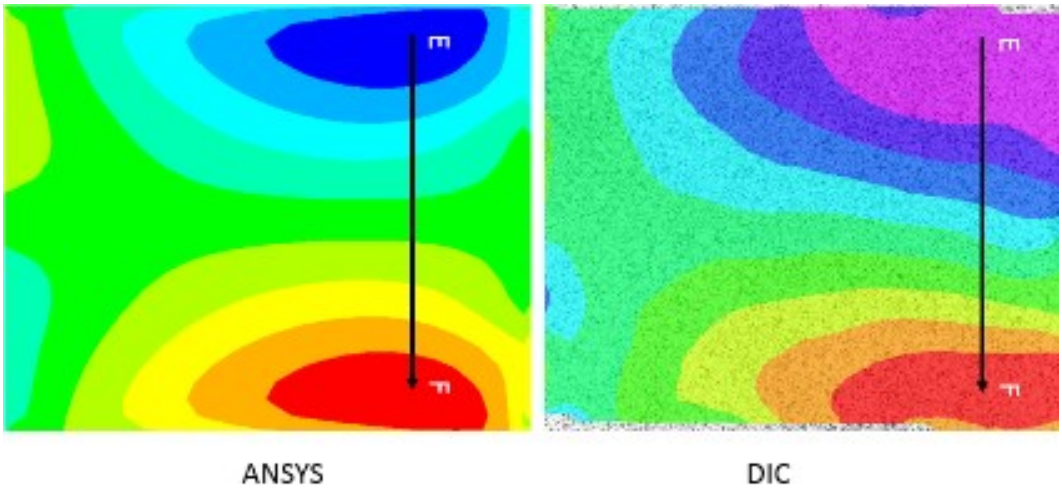

Figure 4.29: Distribution of in-plane shear strain, e_{xy}, on top surface of 80-layer unidirectional clamped configuration at 9.45 mm displacement

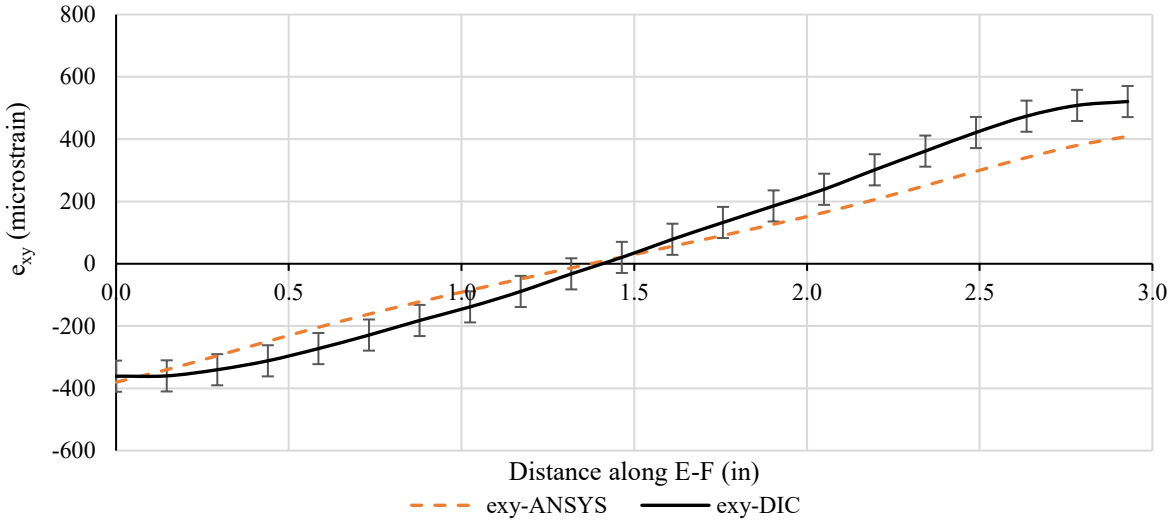

Figure 4.30: In-plane shear strain, e_{xy}, along line E-F of Figure 4.29

4.3.1.2 Side surface

The same comparison performed on the top surface strains was carried out for the thickness side. Figure 4.31 and Figure 4.33 show the thickness side distribution of axial strains, e_{xx}, and interlaminar shear strains (ILSS), e_{xz}, respectively. The area of interest was selected based on preliminary ANSYS and strain gauge results that indicated this area as the location of ultimate shear strain. As is expected for upward bending, axial compressive strains are produced at upper part and tensile strains at lower part of the laminate. The axial strain distribution along line G-H of Figure 4.31 is shown in Figure 4.32. It can be seen

that the ANSYS model is able to predict the axial strain with a reasonable accuracy, where the maximum difference of 23.8% occurs at a Z-position of 26% thickness.

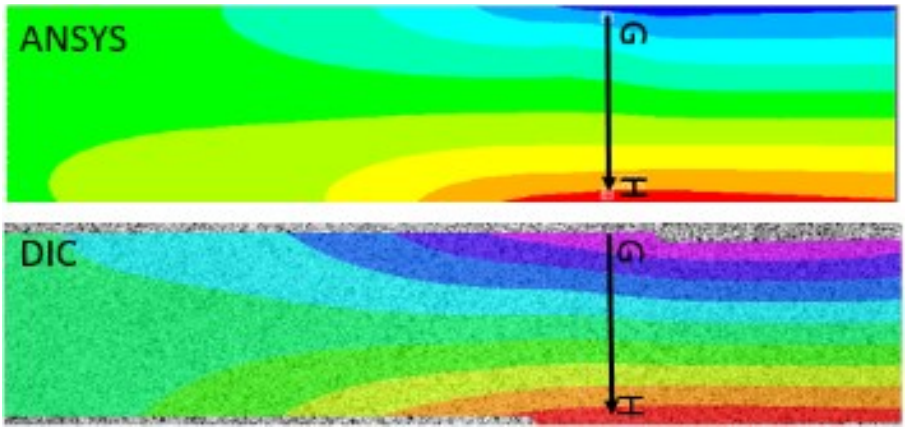

Figure 4.31: Distribution of axial strain, e_{xx}, on side surface of 80-layer unidirectional clamped configuration at 9.45 mm displacement

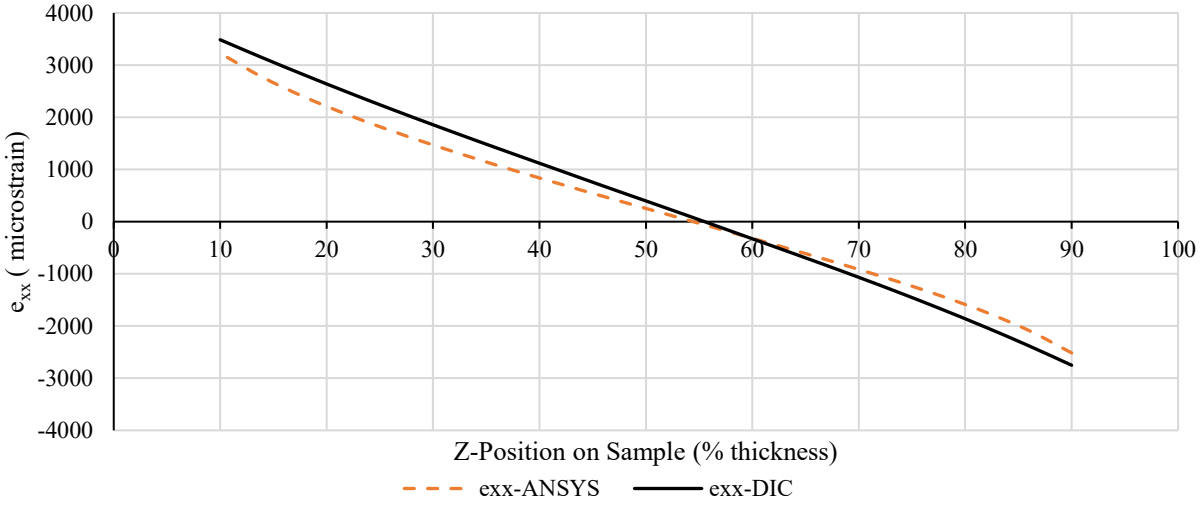

Figure 4.32: Axial strain, e_{xx}, along line G-H of Figure 4.31

The ILSS distribution on the side of the laminate is shown in Figure 4.33. Figure 4.34 shows the ILSS distribution along line I1-J1 of Figure 4.33 through the thickness of the plate, at a location corresponding to X = 3.025 inches, as this is the X-position that ANSYS predicted would have the ultimate ILSS. Furthermore, Figure 4.35 shows the distribution along line I2-J2 of Figure 4.33, along the length of the plate along a line corresponding to Z = 50% thickness. As can be seen from the data in Figure 4.34, Figure 4.35 and the distribution in Figure 4.33, the model and the experimental data match reasonably well both qualitatively and quantitatively. The ultimate ILSS calculated by ANSYS along line I1-J1 was -5497

microstrain while the value measured by DIC was -5635 microstrain, which corresponds to a difference of less than 2.45%. The difficulty in properly applying the gauges and lack of repeatability in the results meant that the data could not be fully trusted for FS3 and FS5. As such, the shear strain gauge data will not be discussed, save for one gauge that was applied to the 80-layer unidirectional clamped sample, FS22. This was the only strain gauge attached to the sample, limiting the possibility of improper application. This gauge was placed at an X-position of 3.025 inches, along the midplane, and registered an ultimate ILSS of -5947 microstrain, as shown in Figure 4.34 and Figure 4.35. This results in a maximum difference between DIC and the strain gauge of 5.2% at that location. It can be seen that the strain gauge was adequately placed for capturing the ultimate shear strain. Also, all three methods predicted and measured the same ultimate shear strain value to a statistically acceptable degree.

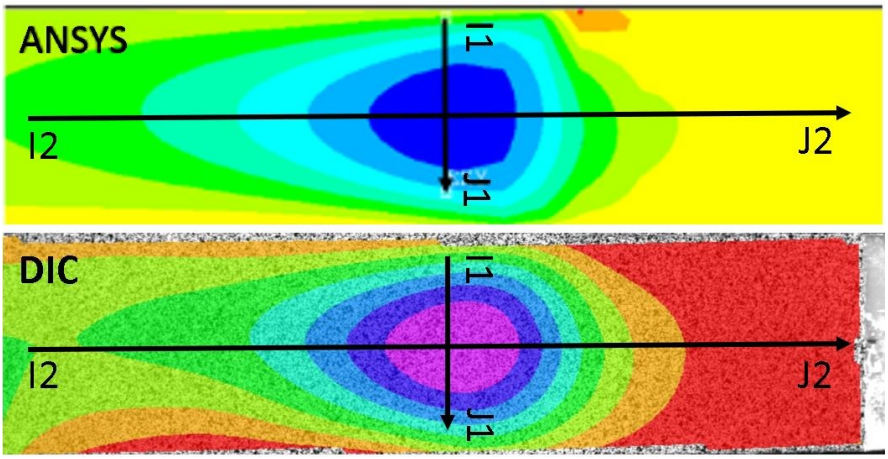

Figure 4.33: Distribution of side surface shear strain, e_{xz}, of 80-layer unidirectional clamped configuration at 9.45 mm displacement

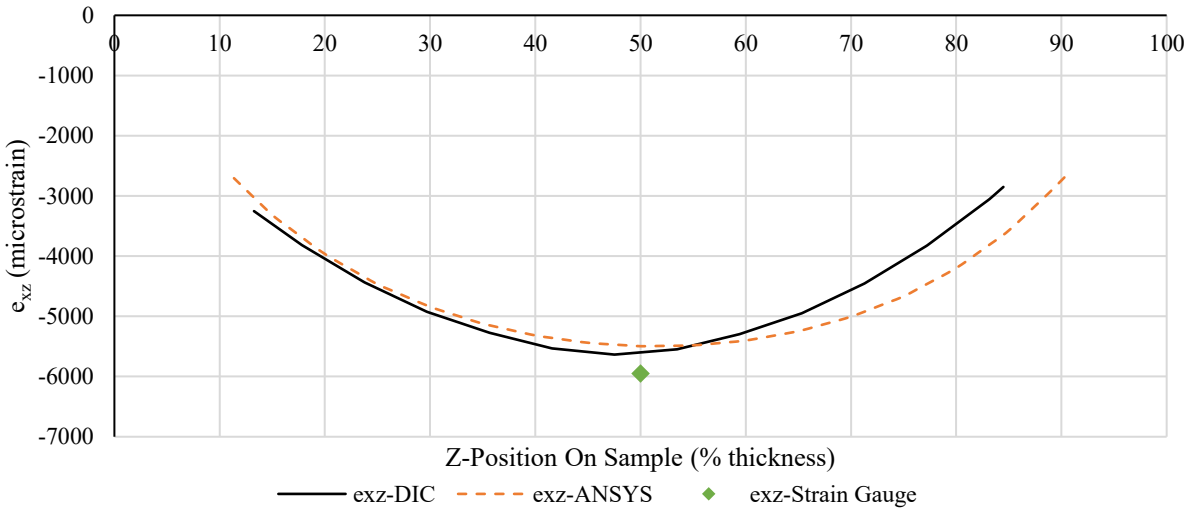

Figure 4.34: Shear strain, e_{xz}, along line I1-J1 of Figure 4.33

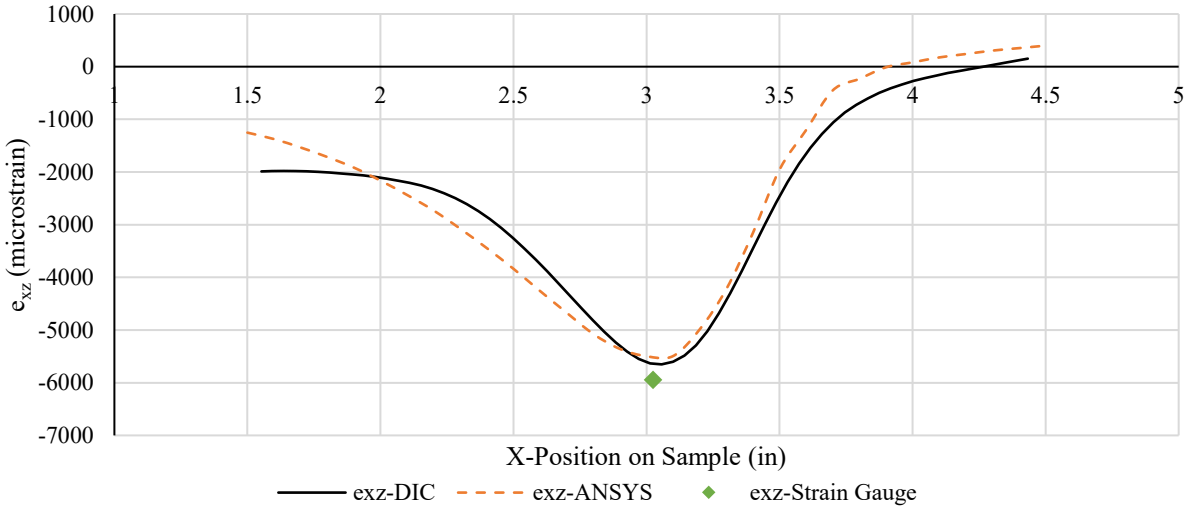

Figure 4.35: Shear strain, e_{xz}, along line I2-J2 of Figure 4.33

4.3.1.3 Ultimate strains

To further validate the ANSYS results, the ultimate strains of the top and thickness sides were obtained from DIC results and they were compared to the corresponding value of strain calculated by ANSYS at the same position. To know the exact position in the DIC images that corresponds to the position of ultimate measured strain, the DIC images were taken with a ruler in view so that a position in the image in pixels can be correlated to an XYZ position in inches. Figure 4.36 (Figure 2.17b repeated) shows a typical DIC image with the ruler in view. Table 4.11 and Table 4.12 summarize the ultimate strain values obtained from DIC with their locations at the top and thickness side surfaces and compares them to the strains

calculated by ANSYS at the same position. Also listed is the maximum difference between ANSYS and the corresponding DIC results. It is clear the differences between the results are minimal at higher strains and in areas where the strains are critical. It should be noted that, despite selecting the whole thickness of the sample to be analyzed by DIC, the program automatically adjusts the selected area for maximum confidence. As such, some of the area of interest automatically gets cut off by the DIC analysis program. This is why the maximum axial strain on the side surface appears to occur at a Z-location corresponding to 66% of the specimen thickness instead of at 100% specimen thickness.

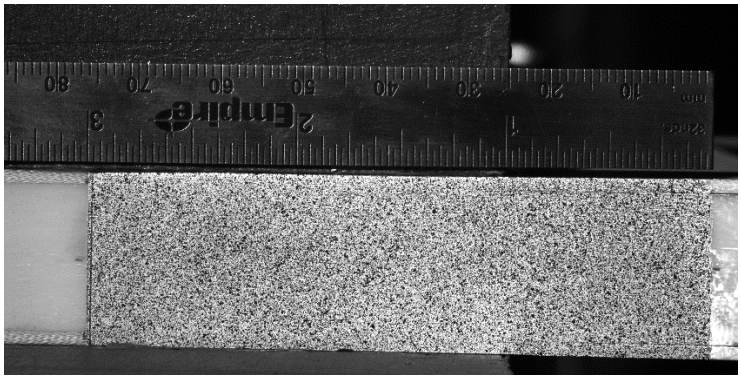

Figure 4.36: Typical DIC image with a ruler to correlate positioning (Figure 2.17b repeated)

Table 4.11: Ultimate strains, in microstrain, on the top surface of 80-layer unidirectional clamped configuration at 9.45 mm displacement

		e_{xx}				e_{yy}				e_{xy}	
		Minimum		**Maximum**		**Minimum**		**Maximum**		**Maximum**	
Position (in)		**X**	**Y**	**X**	**Y**	**X**	**Y**	**X**	**Y**	**X**	**Y**
		5.6	2.0	10.4	2.0	10.3	1.22	5.7	3.9	8.0	0.4
Strain	**DIC**	-2976		-929		188		1024		520	
	ANSYS	-2916		-877		227		838		405	
% Difference		2.02		5.6		20.7		18.2		22.1	

Table 4.12: Ultimate strains, in microstrain, on the thickness side of 80-layer unidirectional clamped configuration at 9.45 mm displacement

		e_{xx}				e_{xz}	
		Minimum		**Maximum**		**Minimum**	
Position		**X (in)**	**Z (%thickness)**	**X (in)**	**Z (%thickness)**	**X (in)**	**Z (%thickness)**
		3.6	0	3.6	66	3.054	50
Strain	**DIC**	-3090		3486		-5653	
	ANSYS	-2956		3227		-5495	
% Difference		4.3		7.4		2.8	

4.3.2 80-Layer Unidirectional Cantilever Configuration

4.3.2.1 Top surface

The same analysis performed in section 4.3.1 (80-Layer Unidirectional Clamped Configuration) was repeated for the 80-layer unidirectional cantilever configuration. Figure 4.37 to Figure 4.44 compare the axial, transverse, and shear strains both qualitatively and quantitatively, at the top surface between ANSYS and DIC. As it can be seen in Figure 4.40, the simulation and experimental test results correlated well with each other for e_{xx} at the top surface, which sees the highest axial strains. The maximum difference for e_{xx} at top surface is less than 8%. Similar to the clamped model, it seems that e_{yy} and e_{xy} have more deviation from the experimental test results, but considering the accuracy of the DIC system of ±50

microstrain, illustrated by the error bars in Figure 4.42 and Figure 4.44, the ANSYS results are in reasonable agreement with DIC for this low level of strain. Although there is seemingly a large discrepancy in top surface shear strain between ANSYS and DIC results, the strain distributions seen in the graph of Figure 4.44 follow the same trend, albeit with the DIC results asymmetric about the graphs x-axis. This asymmetry is also seen in the strain distribution of the DIC results in Figure 4.43 as evidenced by the much larger cold spot at the top right of the distribution pattern compared to the hot spot on the bottom right. This asymmetry is similar to what was seen with the clamped configuration in the previous section.

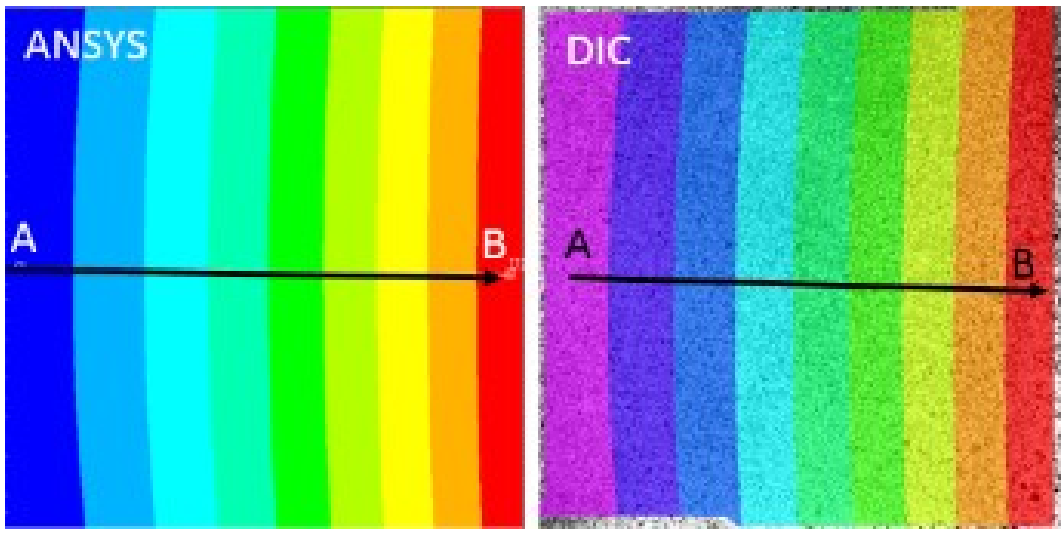

Figure 4.37: Distribution of out-of-plane displacement, *W*, for 80-layer unidirectional cantilever configuration at 9.45 mm displacement

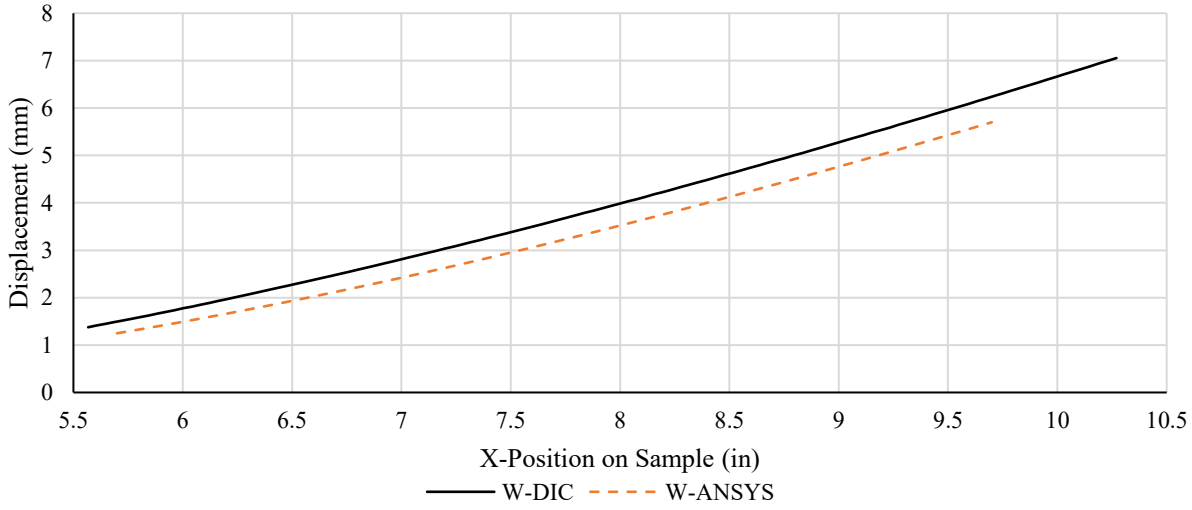

Figure 4.38: Out-of-plane displacement, *W*, along line A-B of Figure 4.37

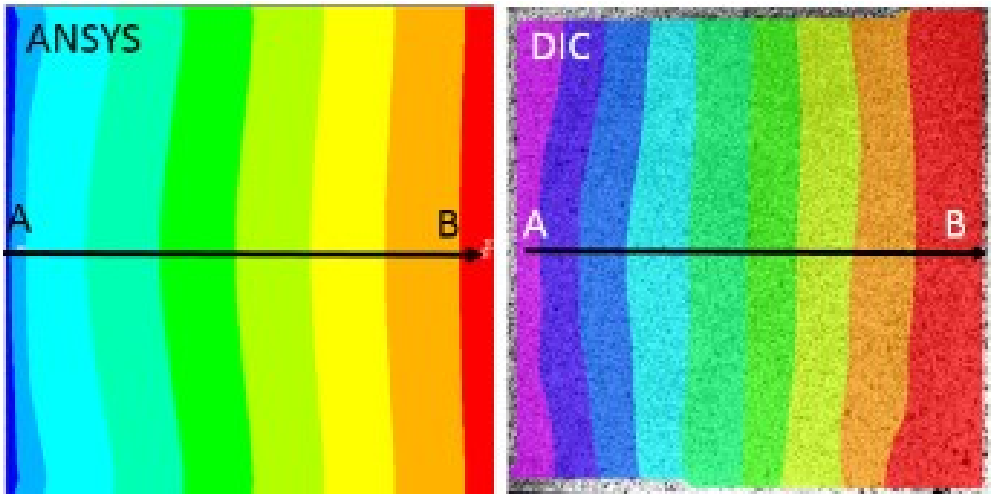

Figure 4.39: Distribution of axial strain, e_{xx}, on top surface of 80-layer unidirectional cantilever configuration at 9.45 mm displacement

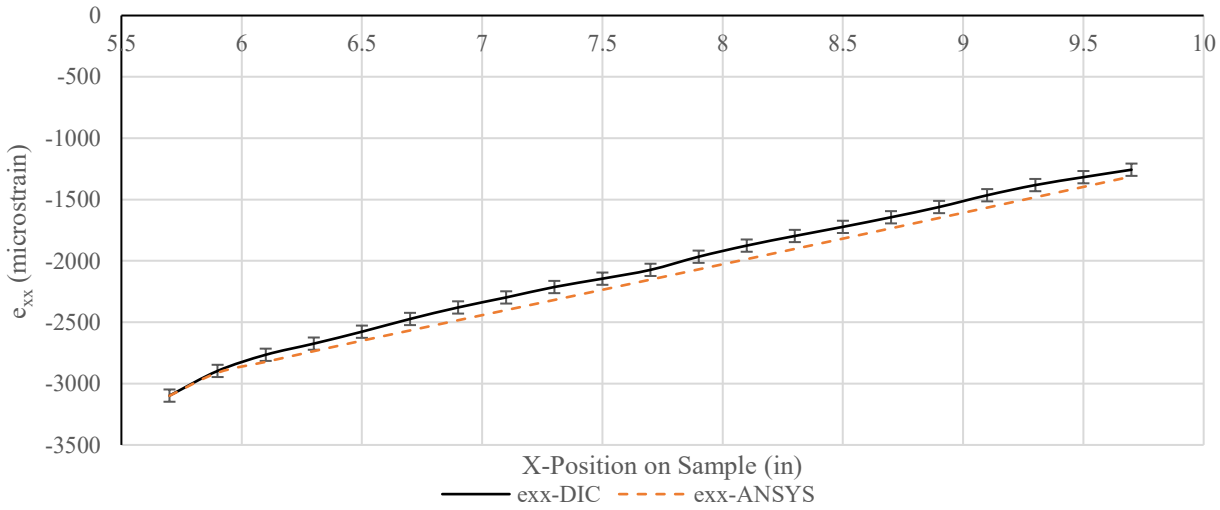

Figure 4.40: Axial strain, e_{xx}, along line A-B of Figure 4.39

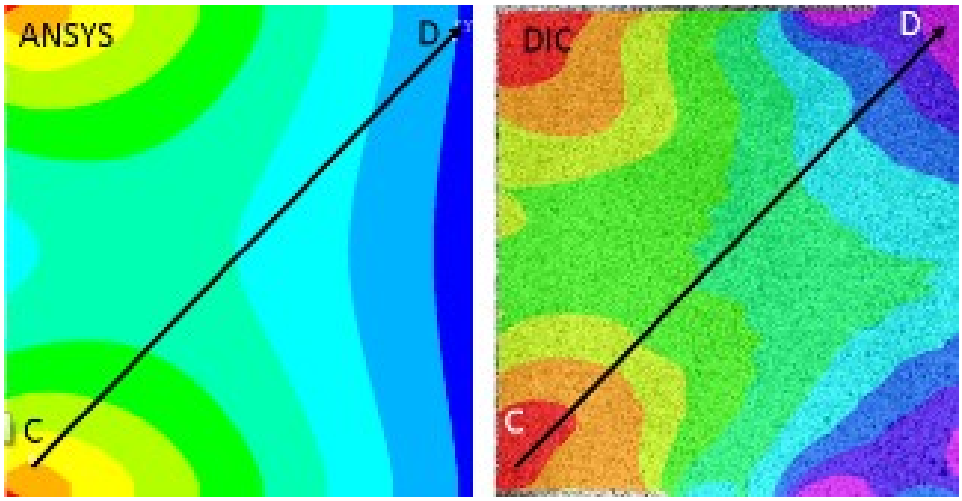

Figure 4.41: Distribution of transverse strain, e_{yy}, on top surface of 80-layer unidirectional cantilever configuration at 9.45 mm displacement

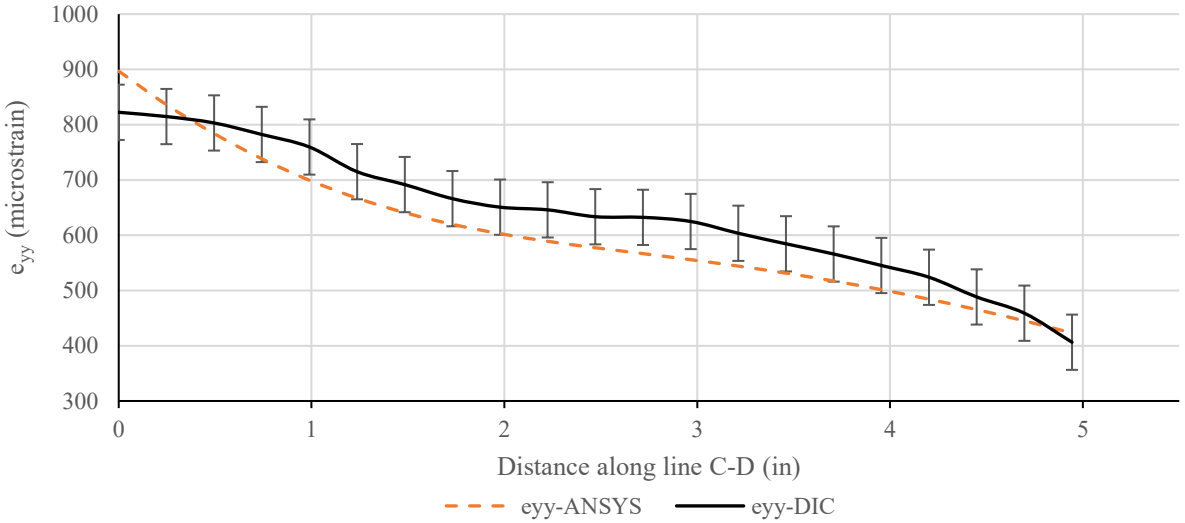

Figure 4.42: Transverse strain, e_{yy}, along line C-D of Figure 4.41

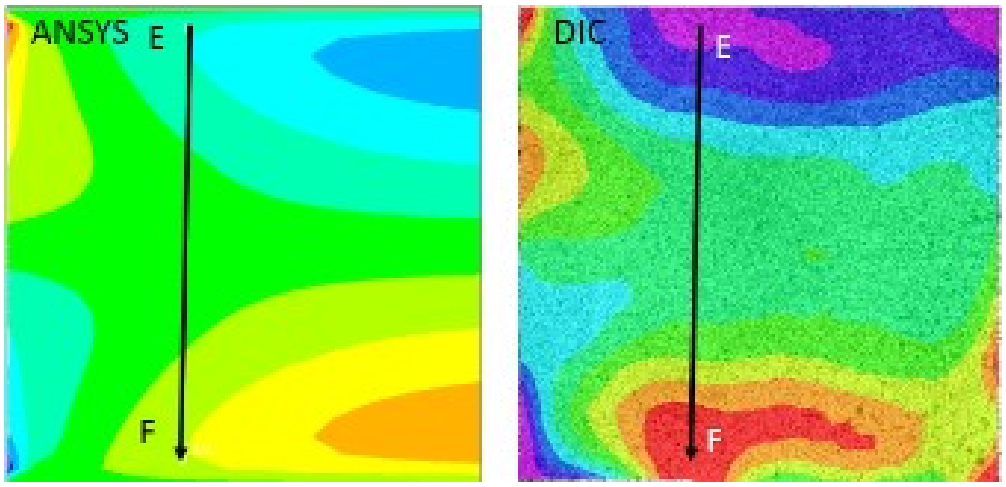

Figure 4.43: Distribution of in-plane shear strain, e_{xy}, on top surface of 80-layer unidirectional cantilever configuration at 9.45 mm displacement

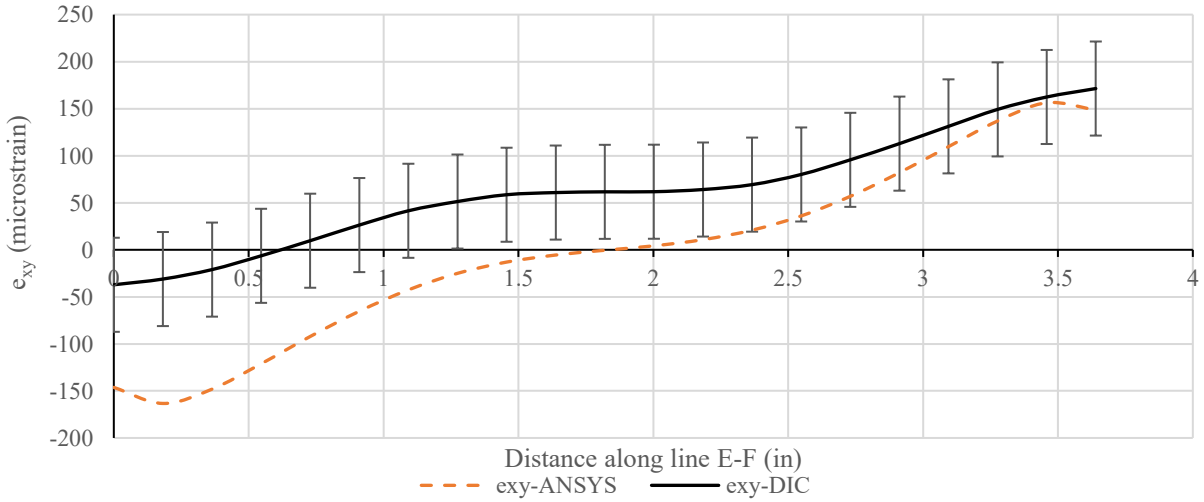

Figure 4.44: In-plane shear strain, e_{xy}, along line E-F of Figure 4.43

4.3.2.2 Side Surface

For the thickness side of the cantilever model, the axial and shear strain distributions on the surface are shown in Figure 4.45 and Figure 4.47, respectively. The corresponding axial strain distribution along line G-H of Figure 4.45 is shown in Figure 4.46, while the shear strain distribution along lines I1-J1 and I2-J2 of Figure 4.47 are shown in Figure 4.48 and Figure 4.49, respectively. As what was seen for the clamped configuration, the axial strains matched very well with experiments shown in Figure 4.45 and Figure 4.46. Furthermore, looking at the ultimate shear strain in Figure 4.48, it is clear both methods measured the same strain value at the same location. However, there is more discrepancy between ANSYS and DIC data in Figure 4.49. At the location of ultimate strain as measured by DIC around the 2.9-inch mark, the ANSYS value is almost identical with a percentage difference of only 0.78%. However, it is clear from the graph that ANSYS estimated a higher shear strain magnitude of 5507 microstrain around the 3.1-inch mark, where the corresponding difference with DIC is 16.8%. The reason for this discrepancy coud not be determined.

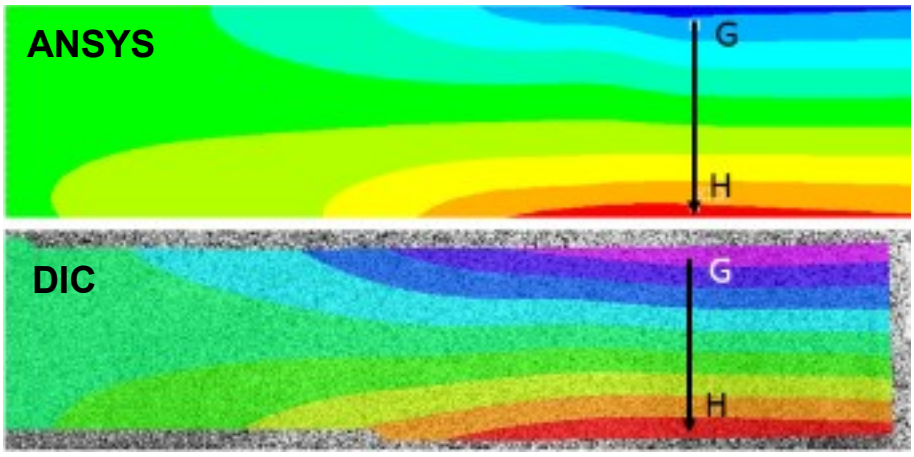

Figure 4.45: Distribution axial strain, e_{xx}, on side surface of 80-layer unidirectional cantilever configuration at 9.45 mm displacement

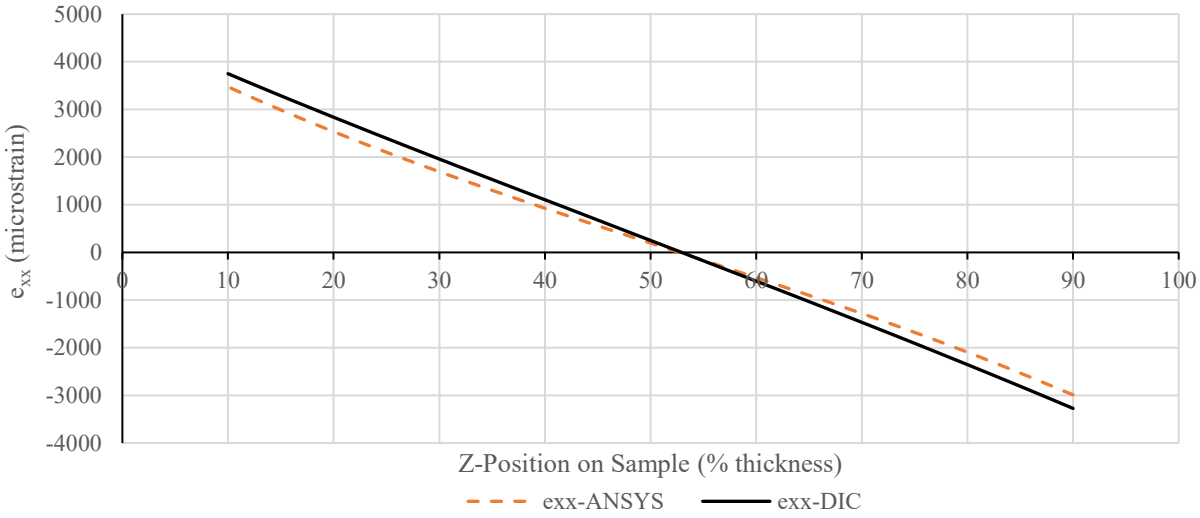

Figure 4.46: Axial strain, e_{xx}, along line G-H of Figure 4.45

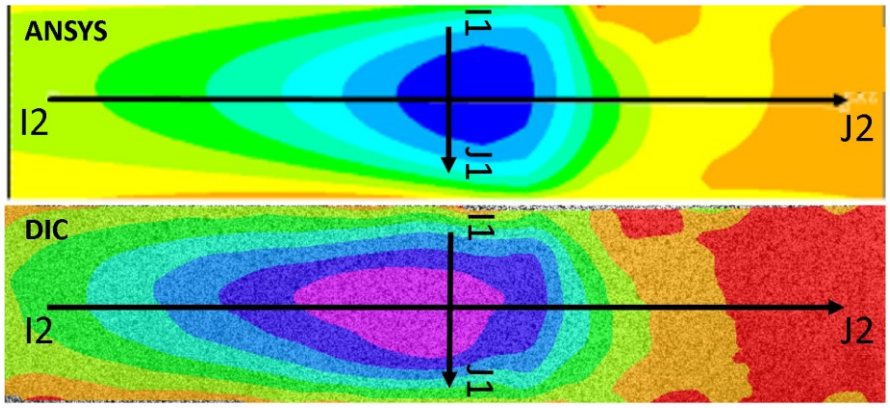

Figure 4.47: Distribution of side surface shear strain, e_{xz}, of 80-layer unidirectional cantilever configuration at 9.45 mm displacement

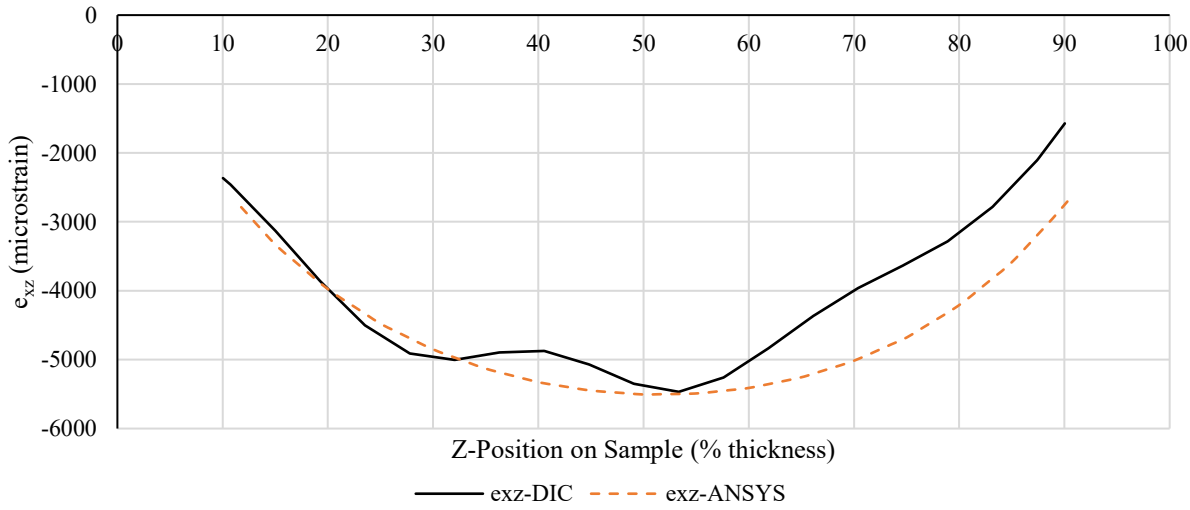

Figure 4.48: Shear strain, e_{xz}, along line I1-J1 of Figure 4.47

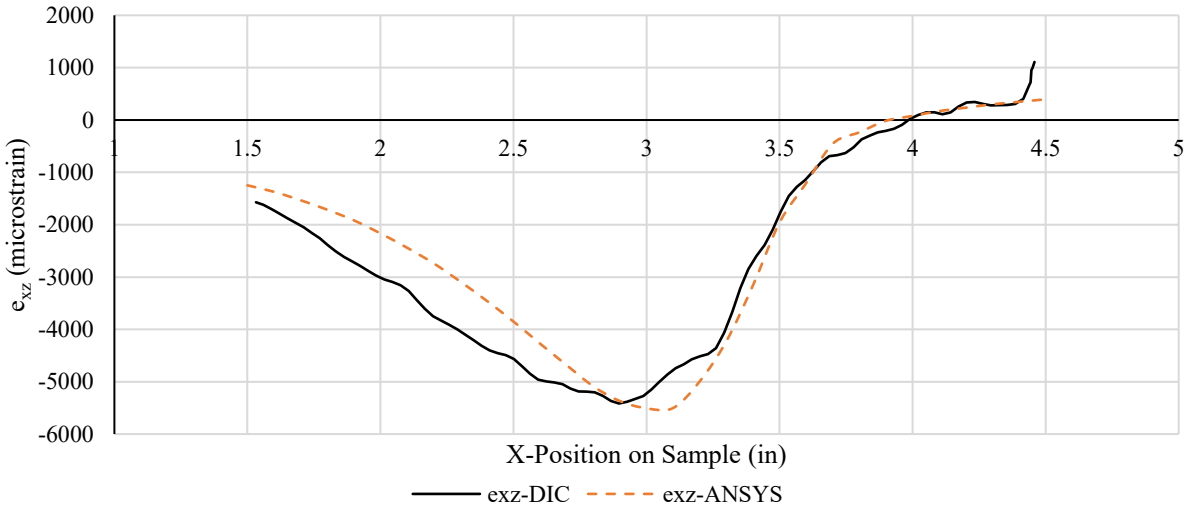

Figure 4.49: Shear strain, e_{xz}, along line I2-J2 of Figure 4.47

4.3.2.3 Ultimate strains

Table 4.13 and Table 4.14 summarize the ultimate strain results obtained from DIC for each strain and compares them to the strains calculated by ANSYS simulation at the same position for the top and side surfaces respectively. Once again, there is very good agreement at higher strain levels.

Table 4.13: Ultimate strains, in microstrain, on the top surface of 80-layer unidirectional cantilever configuration at 9.45 mm displacement

		e_{xx}				e_{yy}				e_{xy}	
		Minimum		**Maximum**		**Minimum**		**Maximum**		**Maximum**	
Position (in)		**X**	**Y**	**X**	**Y**	**X**	**Y**	**X**	**Y**	**X**	**Y**
		5.6	2.0	9.75	2.0	9.6	3.8	5.6	0.2	7.5	0.3
Strain	**DIC**	-3097		-1257		406		822		171	
	ANSYS	-3099		-1312		423		897		149	
% Difference		0.06		4.4		4.2		9.1		12.9	

Table 4.14: Ultimate strains, in microstrain, on the thickness side of 80-layer unidirectional cantilever configuration at 9.45 mm displacement

		e_{xx}				e_{xz}	
		Minimum		Maximum		Maximum	
Position		X (in)	Z (%thickness)	X (in)	Z (%thickness)	X (in)	Z (%thickness)
		3.5	10	3.5	9.7	2.9	55
Strain	DIC	-3273		3750		-5639	
	ANSYS	-2990		3473		-5426	
% Difference		8.6		7.4		3.8	

4.3.3 80-Layer Cross-Ply Cantilever Configuration

4.3.3.1 Top Surface

A cross-ply laminate configuration with a layup sequence of $[0/90]_{20s}$ was also tested as part of this study. In this section, only the top surface axial strains, and side surface axial and shear strains were compared between ANSYS and DIC results due to their higher strain values. Figure 4.50 shows the top surface axial strain distribution while Figure 4.51 shows the strain along line A-B from Figure 4.50. As with the previous configurations, the agreement between ANSYS and DIC results is very good both qualitatively and quantitatively for this type of strain.

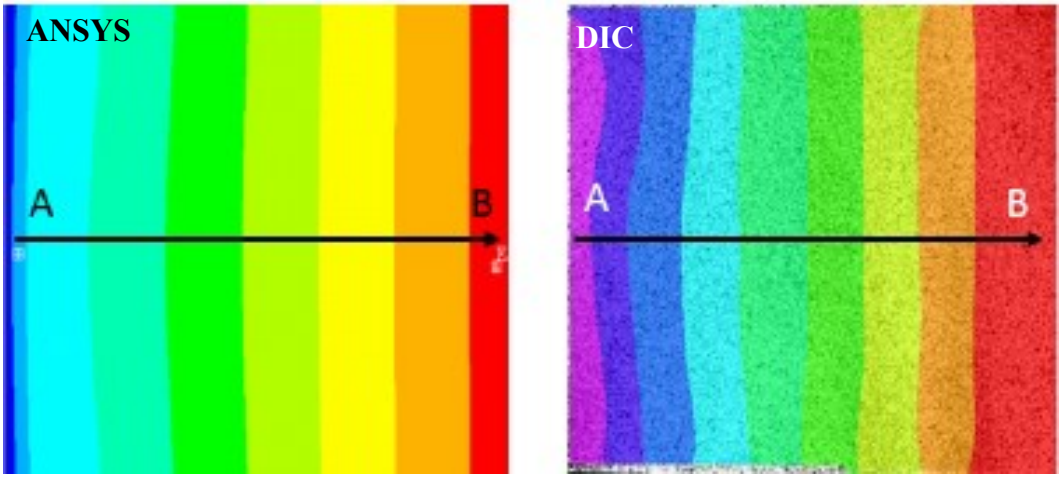

Figure 4.50: Distribution of axial strain, e_{xx}, on top surface of 80-layer cross-ply cantilever configuration at 9.45 mm displacement

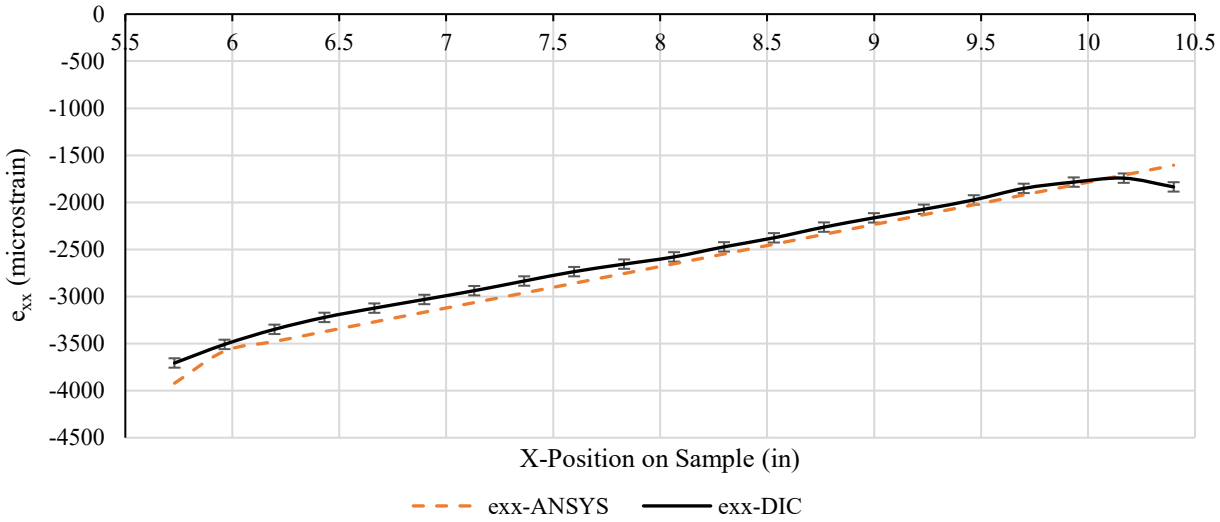

Figure 4.51: Axial strain, e_{xx}, along line A-B of Figure 4.50

4.3.3.2 Side Surface

Looking at the side surface, the axial and ILSS patterns, shown in Figure 4.52 and Figure 4.54, respectively, show very similar patterns to the other configurations. They also show good qualitative agreement between ANSYS and DIC. The axial strain along line G-H of Figure 4.52 is shown in Figure 4.53, while the shear strain along line I-J of Figure 4.54 is shown in Figure 4.55. The two methods match perfectly for the axial strain while the graph of shear strain shows relatively good qualitative agreement. Although the shear strain calculated by ANSYS is seen to diverge from the measured DIC shear strain around the most critical area, the difference between the two methods at the ultimate shear strain as measured by DIC is only 5.1%.

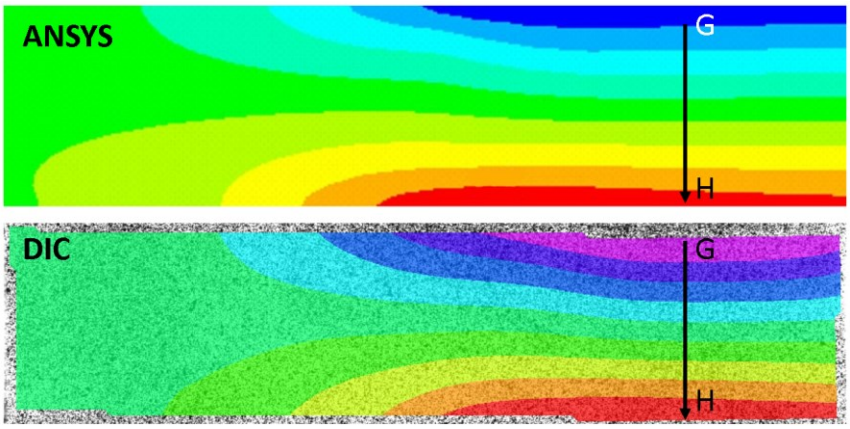

Figure 4.52: Distribution axial strain, e_{xx}, on side surface of 80-layer cross-ply cantilever configuration at 9.45 mm displacement

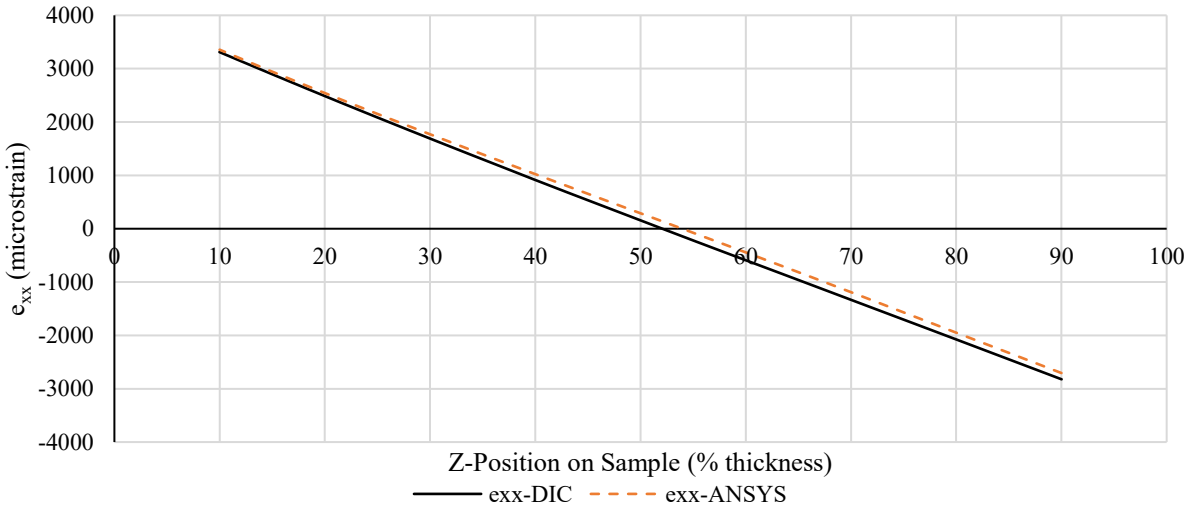

Figure 4.53: Axial strain, e_{xx}, along line G-H of Figure 4.52

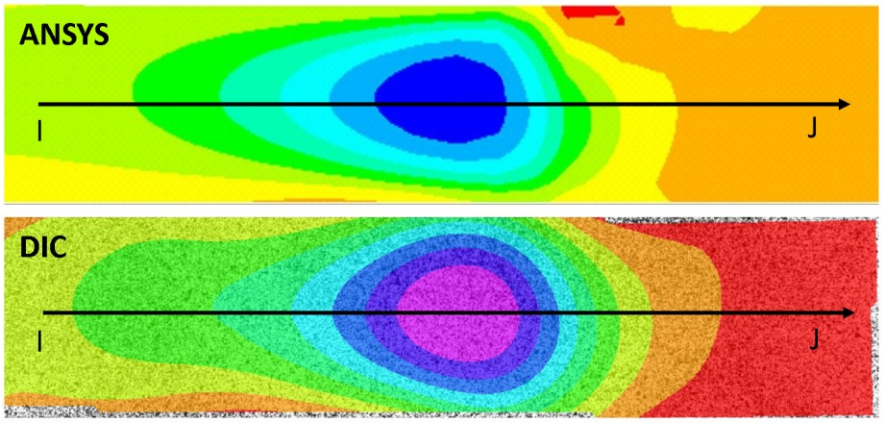

Figure 4.54: Distribution of side surface shear strain, e_{xz}, of 80-layer cross-ply cantilever configuration at 9.45 mm displacement

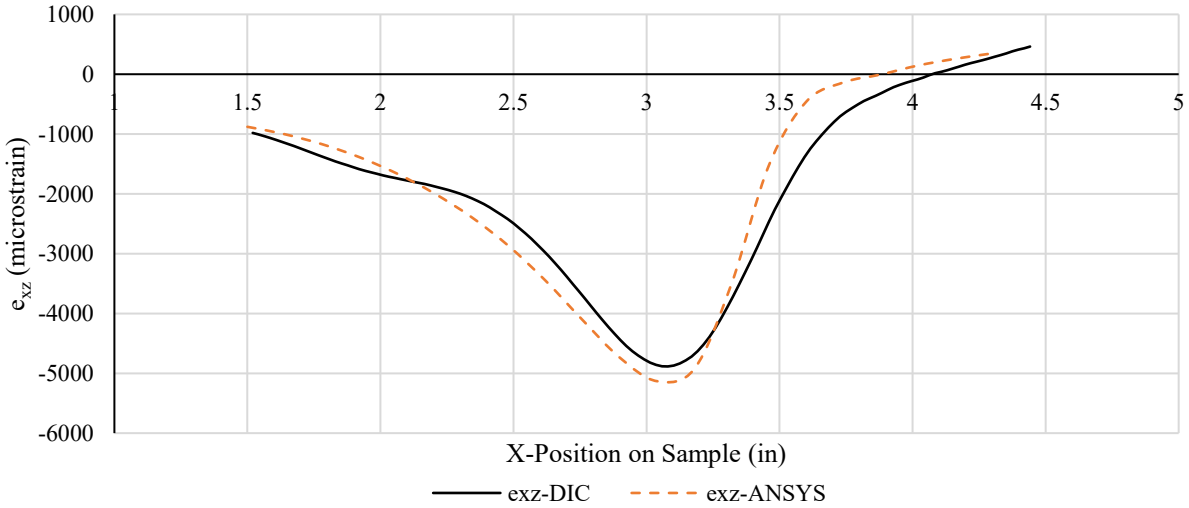

Figure 4.55: Shear strain, e_{xz}, along line I-J of Figure 4.54

4.3.3.3 Ultimate Strains

As what was done for the previous configurations, the ultimate strains as measured by DIC are compared to the strains at the same locations calculated by ANSYS in Table 4.15. It is clear that the ANSYS model can accurately predict the strains at critical locations a for cross-ply configuration.

Table 4.15: Ultimate strains, in microstrain, on the top and side surfaces of 80-layer cross-ply cantilever configuration at 9.45 mm displacement

		e_{xx} (Top)				e_{xx} (Side)				e_{xz} (Side)	
		Minimum		Maximum		Minimum		Maximum		Maximum	
Position		X (in)	Y (in)	X (in)	Y (in)	X (in)	Z (%thick)	X (in)	Z (%thick)	X (in)	Z (%thick)
		5.6	2.0	10.4	2.0	3.9	90	3.9	10	3.1	58
Strain	DIC	-3706		-1835		-2823		3311		-5197	
	ANSYS	-3921		-1605		-2705		3356		-5132	
% Difference		5.8		12.5		4.18		1.36		1.25	

4.3.4 Low Displacement Strain Comparison Between Configurations

Although the ANSYS model was not run for the thinner samples, it is useful to compare the strain distributions as measured by DIC between configurations to see how they change with changing specimen thickness or layup sequence.

4.3.4.1 Top Surface

Figure 4.56 shows the top surface axial strain, e_{xx}, at 9.45 mm of specimen displacement for each cantilever configuration, with the colour contour scale fixed to account for the maximum and minimum strain levels seen by each configuration. The scale, in microstrain, is also shown in the figure. Although the strain patterns for each thickness looked similar to what was seen in Figure 4.23, Figure 4.39, and Figure 4.50, when the colour contour scale was set to auto-adjust based on each configuration's strain level, with the colour contour scale fixed, it can be seen how the maximum and minimum strain levels change with increasing specimen thickness.

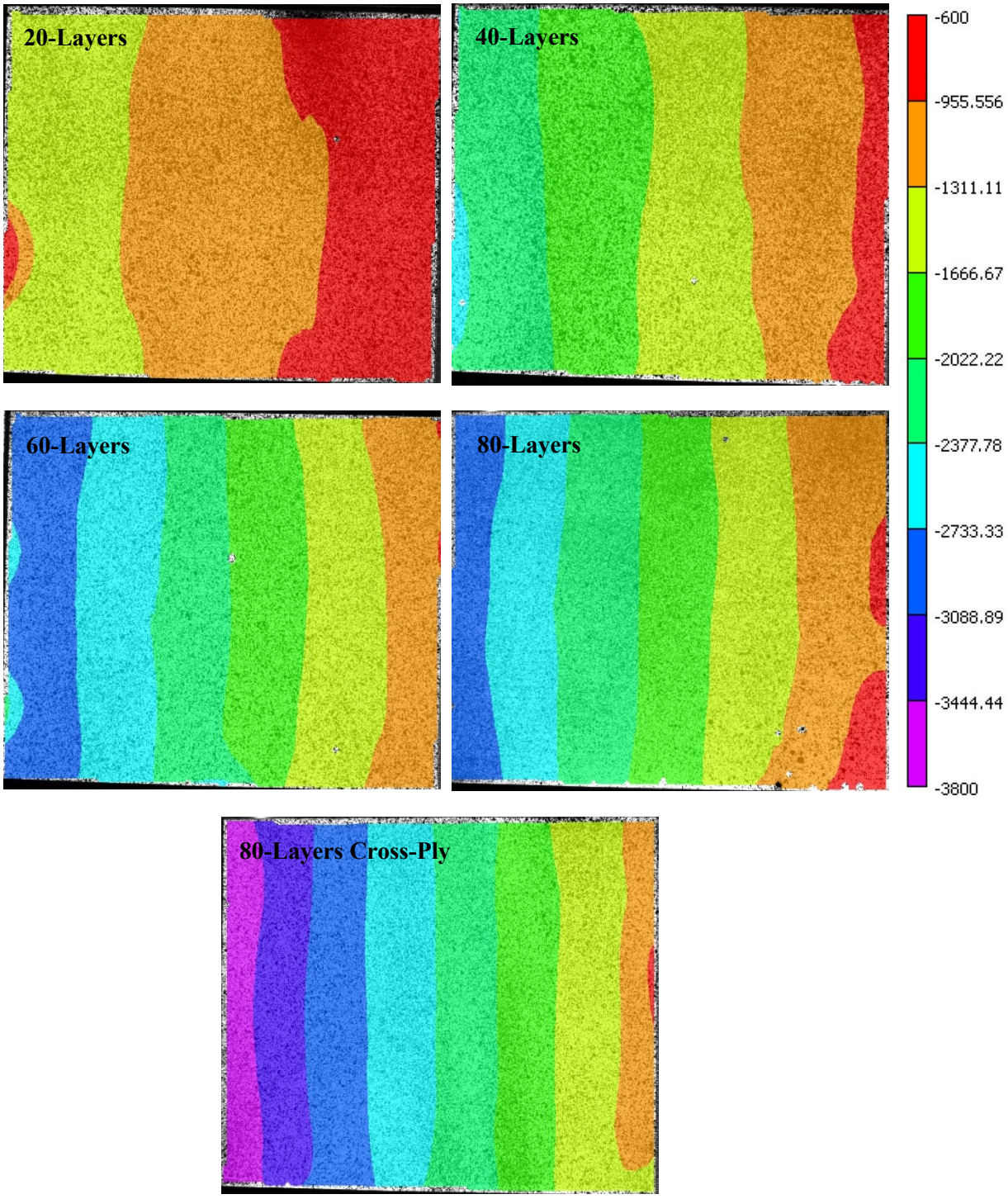

Figure 4.56: Top surface axial strain distribution, e_{xx}, for each cantilever specimen configuration at 9.45 mm displacement with fixed colour contour scale

It is interesting to note how similarly the 60- and 80-layer configurations behaved with regards to axial strain. That being said, it is important to note that the load applied to the 60-layer configuration is almost 2000 N less than what is applied to the 80-layer configuration at this displacement, despite strain

levels being so similar. Also, the cross-ply configuration saw higher levels of axial strain as compared to the unidirectional configuration. This is to be expected since the 90-degreee layers in the cross-ply configuration do not provide much stiffness axially, thereby allowing the top surface of the sample to undergo greater deformation in compression for a given specimen deflection. Figure 4.57 shows the same data graphically. The graph represents the strain distribution along a line passing through the mid-width of each configuration. Again, the similarity between the 60- and 80-layer configurations is apparent, as is the higher strain levels experienced by the cross-ply configuration.

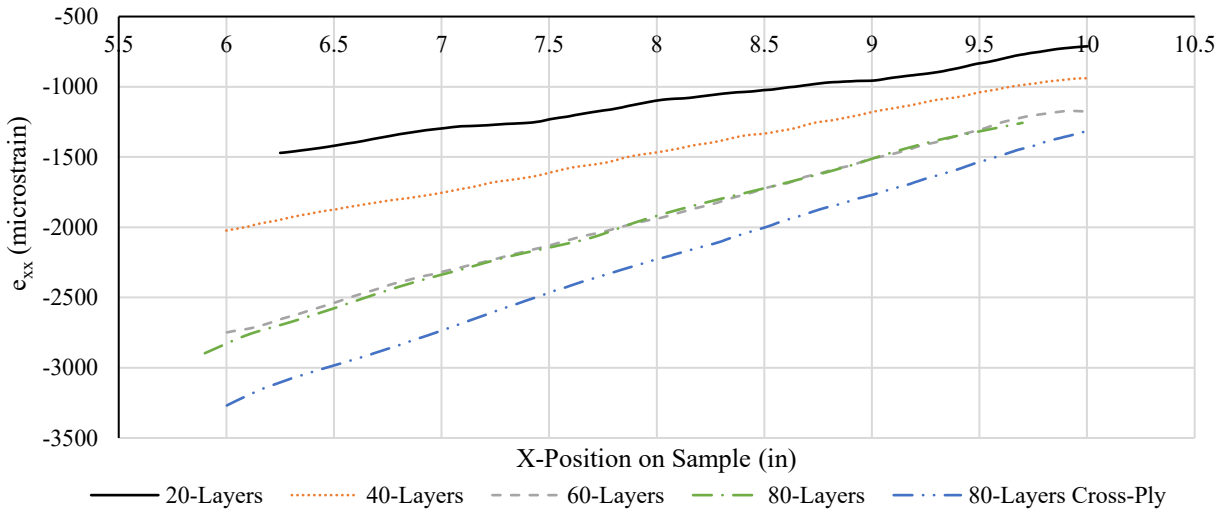

Figure 4.57: Top surface axial strain, e_{xx}, along the mid-width of each cantilever specimen configuration at 9.45 mm displacement

4.3.4.2 Side Surface

Despite the similarity in top surface axial strain distribution between the 60- and 80-layer unidirectional configurations, comparing the side surface axial and shear strains shows a different story. Figure 4.58 shows the side surface fixed scale axial strain distribution for each cantilever specimen configuration. Remembering that in these images, the fixed end of the specimen is towards the left, the 80-layer unidirectional and cross-ply configurations tend to behave very similarly, with the major difference between the two being how deep into the clamped portion of the specimen the axial strain propagates, illustrated by the longer colour contours of the unidirectional configuration. It is interesting to note that the colour scale rainbow tends to grow with increasing specimen thickness, while the thickness of the colour bands remains relatively the same. This indicates that the side surface axial strain is proportional to

thickness. Figure 4.59 graphs the through thickness axial strain distribution for each unidirectional cantilever configuration along a line passing through X=3.75 inches, which would be just passed the fixed end support on the specimen. The similarity in strain values between the 80-layer unidirectional and cross-ply configurations is also apparent in this figure.

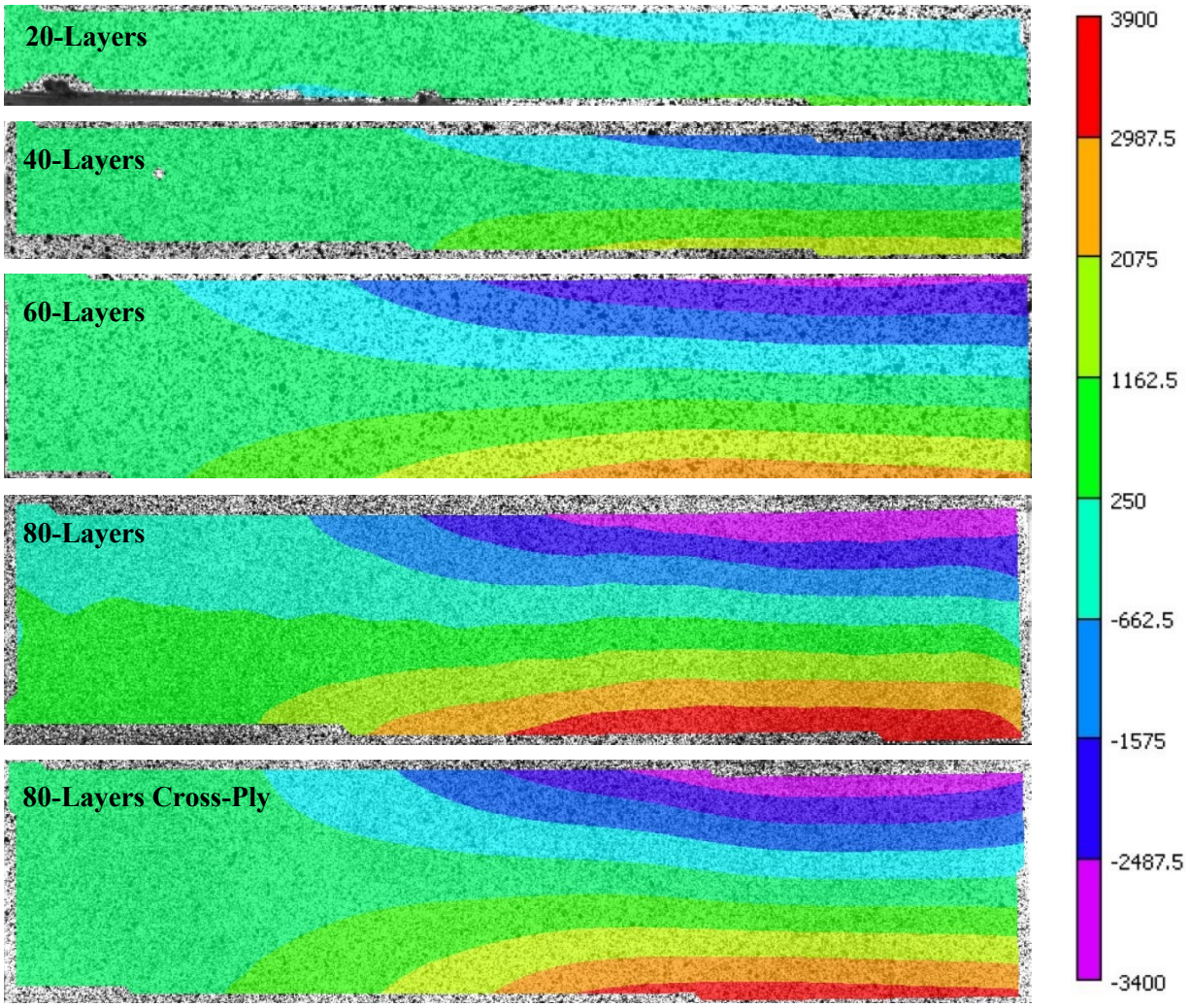

Figure 4.58: Side surface axial strain distribution, e_{xx}, for each cantilever specimen configuration at 9.45 mm displacement with fixed colour contour scale

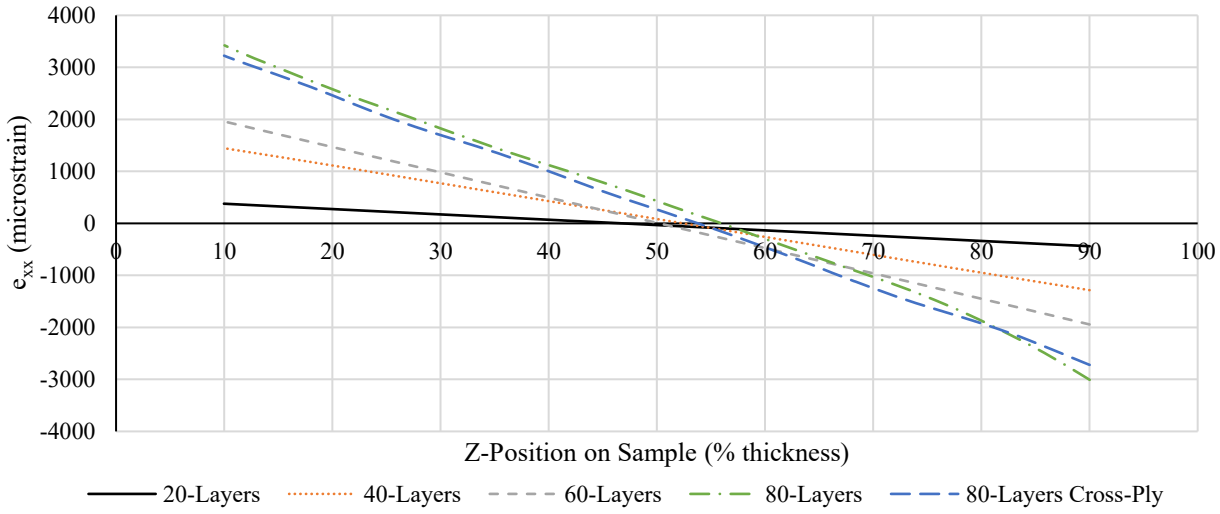

Figure 4.59: Side surface axial strain, e_{xx}, along X = 3.75 inches for each cantilever specimen configuration at 9.45 mm displacement

Figure 4.60 shows the fixed scale side surface shear strain distribution for each cantilever configuration. The two most notable trends that can be seen in these images are how the location of maximum shear strain tends to move closer to the fixed end of the specimen as thickness increases, as well as how the magnitude and size of the area around the maximum shear strain increases with increasing thickness. Alternatively, the cross-ply configuration sees almost the same level of maximum shear strain as the 80-layer unidirectional configuration, albeit over a much smaller area. This is to be expected since the reduced stiffness in the 90-degree layers of the cross-ply configuration does not allow the ILSS to propagate as much along the length of the specimen compared to the unidirectional configuration. These same trends can be seen in the graphical data of Figure 4.61, which shows the side surface shear strain distribution along the midplane of each cantilever configuration. It can also be seen in this figure that the strain distribution along the midplane follows a similar trend, albeit at different magnitudes for each specimen thickness.

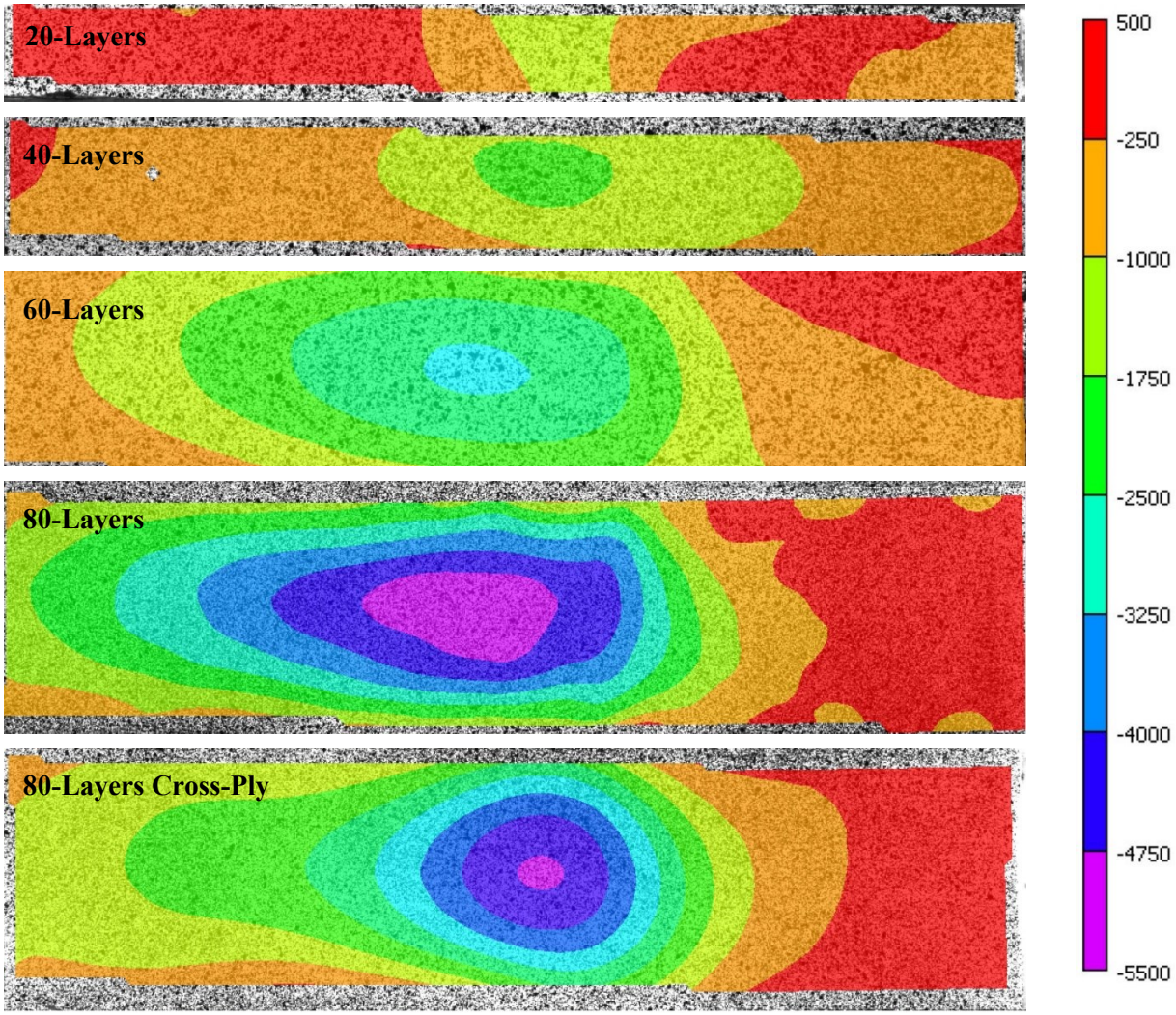

Figure 4.60: Side surface shear strain distribution, e_{xz}, for each unidirectional cantilever specimen configuration at 9.45 mm displacement with fixed colour contour scale

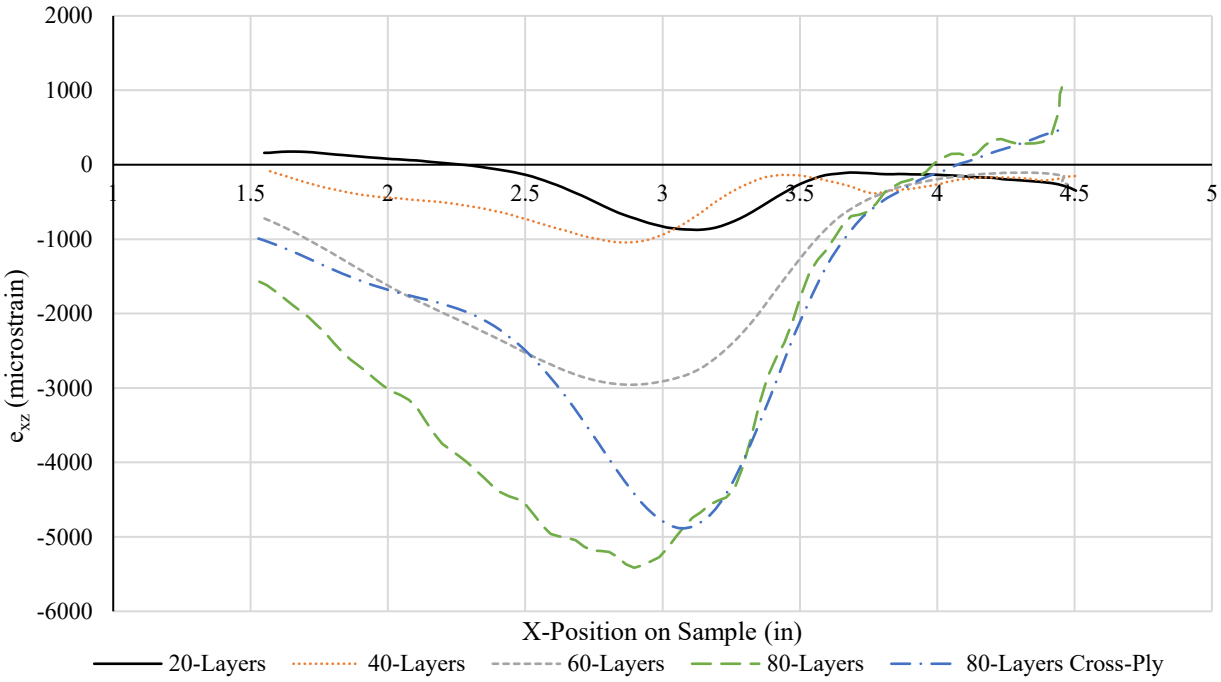

Figure 4.61: Side surface shear strain, e_{xz}, along the midplane for each cantilever specimen configuration at 9.45 mm displacement

4.4 Strain Analysis to Failure

The next step in analyzing the bending behaviour of composite laminates requires observation of how the specimens behave up to failure. As mentioned previously, the 20- and 40-layer configurations were unable to fail. As such, the 20-layer configuration will not be discussed in this section. However, to 40-layer configuration data can still be used to make certain deductions when compared to the thicker configurations. Since the ILSS is of greatest interest, that will be the focus of this section.

4.4.1 DIC Validation to Failure

To fully validate the use of DIC for strain measurement, it is important to confirm its accuracy all the way to specimen failure. Figure 4.62 shows the top surface axial strain as measured by a strain gauge located at X = 6.25 inches and Y = 2 inches for 80-layer unidirectional clamped specimens FS3 and FS5. The graph also includes the corresponding DIC measurements on sample FS22. It is clear from the proximity of the results that the DIC system was able to accurately capture the top surface axial strains all the way to specimen failure. Similar proximity between strain gauge and DIC results can be seen in Figure 4.63 showing the top surface transverse strains at a location corresponding to X = 5.75 inches and Y = 3.75

inches, despite the DIC data beginning to oscillate near failure. This oscillation was caused by glare from the lab lighting reflecting into the DIC camera as the specimen deflected under load. Lastly, for the strain of most interest, Figure 4.64 shows a comparison of side surface shear strain on sample FS22 as measured by DIC and strain gauge at a location corresponding to X = 3.025 inches and Z = 50% thickness. Once again, it is clear the DIC system was very accurate in capturing the critical strain up to failure.

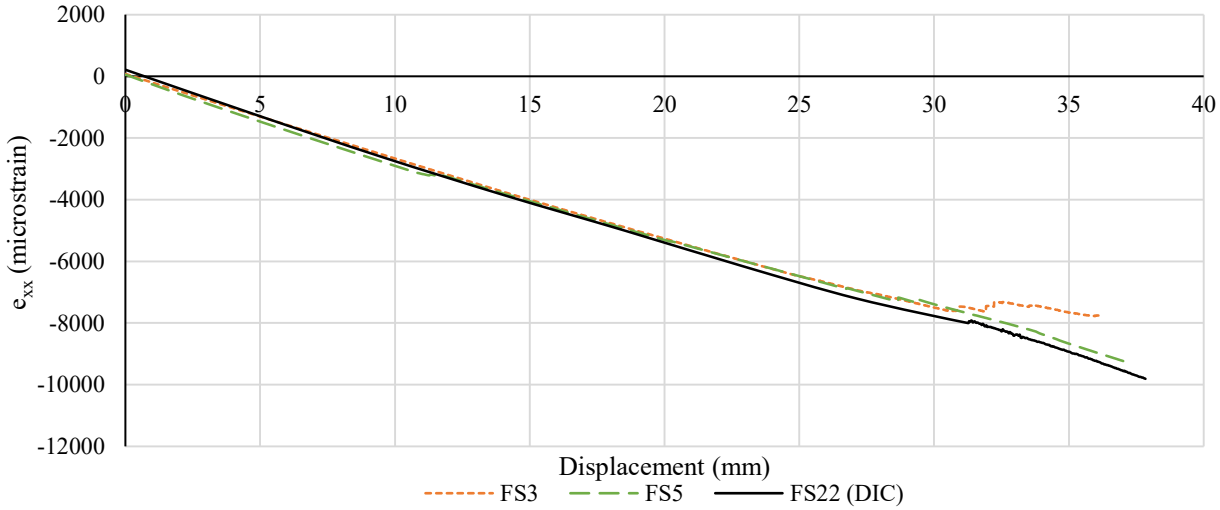

Figure 4.62: Top surface axial strain, e_{xx}, at X = 6.25 inches and Y = 2 inches as measured by strain gauge and DIC for the 80-layer unidirectional clamped specimens vs. displacement to failure

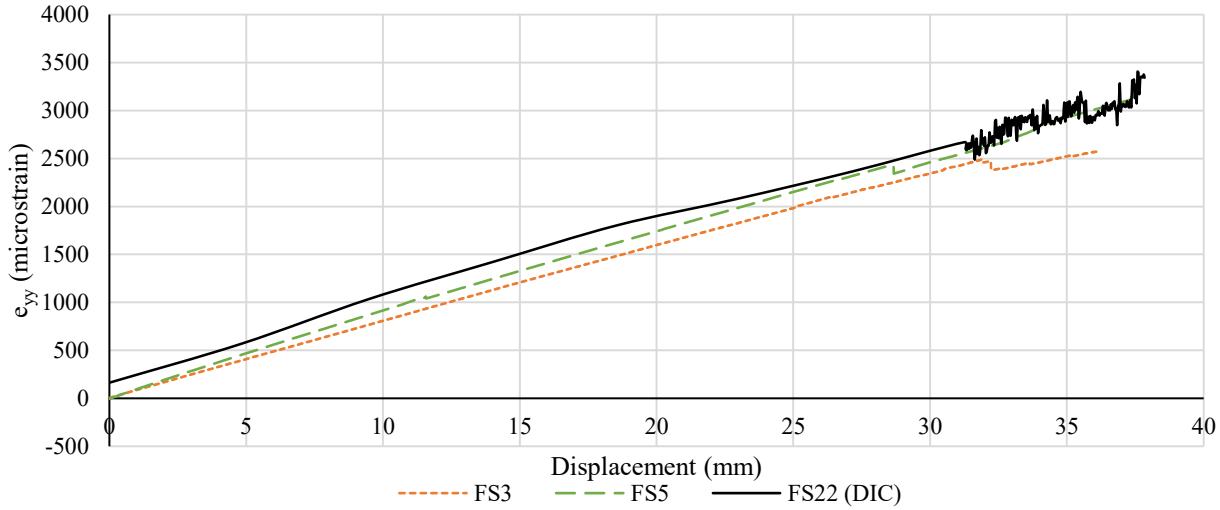

Figure 4.63: Top surface transverse strain, e_{yy}, at X = 5.75 and Y = 3.75 inches as measured by strain gauge and DIC for the 80-layer unidirectional clamped specimens vs. displacement to failure

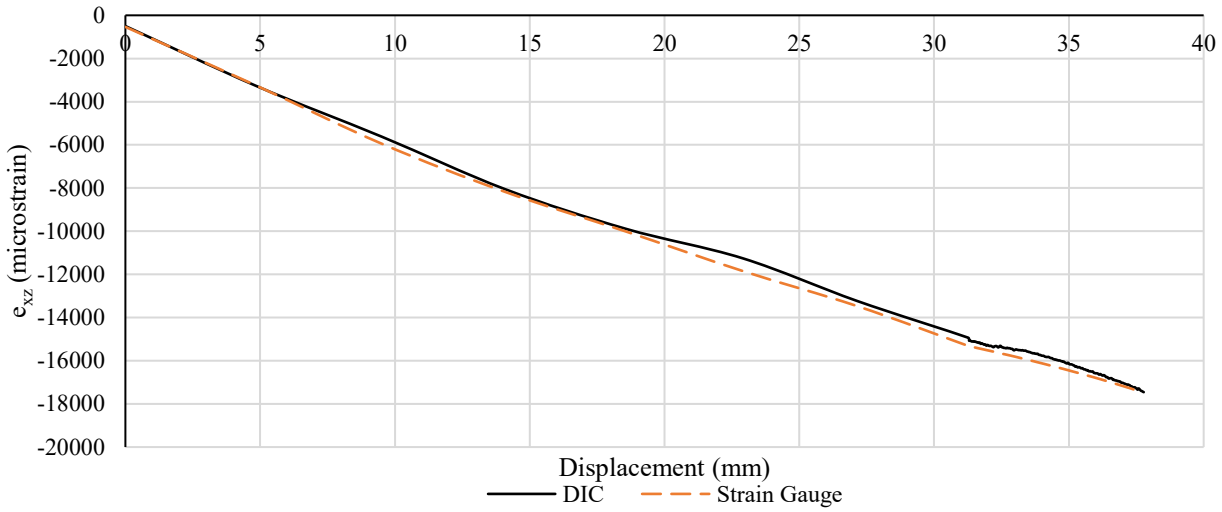

Figure 4.64: Side surface shear strain, e_{xz}, at X = 3.025 inches and Z = 50% thickness as measured by strain gauge and DIC for the 80-layer unidirectional clamped specimen, FS22 vs. displacement to failure

4.4.2 80-Layer Configuration Comparison

As was seen in section 4.3 (Strains Analysis at 9.45 mm Specimen Displacement), at low displacement levels the 80-layer configurations experienced similar critical ILSS magnitudes. Table 4.16 lists the corresponding shear strains for each 80-layer configuration with the corresponding position on the side surface at 9.45 mm of specimen displacement. The locations along the length of the specimens where these critical strains appear is quite similar between configurations, however, the positions through the thickness are different. As the specimens progress towards failure, the difference between their behaviours becomes more apparent. Table 4.17 shows the same information as Table 4.16 except the data was captured at the corresponding failure displacements for each 80-layer configuration. It is interesting to note that, despite experiencing similar strains at low displacements, the 80-layer unidirectional clamped configuration fails with significantly higher ILSS than the 80-layer unidirectional cantilever configuration. This means that at failure, the clamped configuration is slightly less stiff in shear than its cantilever counterpart. One might expect that clamping the loaded end of the specimen would cause the specimen to behave more stiffly even in shear, however, this strain data contradicts that notion.

Table 4.16: Critical side surface shear strains, in microstrain, for the 80-layer configurations at 9.45 mm displacement

	Unidirectional Clamped		Unidirectional Cantilever		Cross-Ply Cantilever	
Position	**X (in)**	**Z (%thick)**	**X (in)**	**Z (%thick)**	**X (in)**	**Z (%thick)**
	3.054	50	2.9	55	3.1	58
Strain	-5653		-5639		-5197	

Table 4.17: Critical side surface shear strains, in microstrain, for the 80-layer configurations at failure

	Unidirectional Clamped		Unidirectional Cantilever		Cross-Ply Cantilever	
Failure Displacement	**37 mm**		**38 mm**		**42 mm**	
Position	**X (in)**	**Z (%thick)**	**X (in)**	**Z (%thick)**	**X (in)**	**Z (%thick)**
	2.67	50	2.50	50	2.94	50
Strain	-18,675		-17,155		18,201	

To illustrate the data graphically, Figure 4.65 plots the side surface ILSS distribution along the midplane of each 80-layer configuration at their corresponding failure displacements. A couple interesting things to note about this data are that, first, the ILSS of the cross-ply configuration rises to its maximum magnitude over a much shorter length along the specimen as compared to the unidirectional configurations. The shear strain quickly dissipates as it moves away from the critical location. Second, despite failing at similar displacement and load levels, the two 80-layer unidirectional configurations see very different maximum ILSS magnitudes, but almost identical strain distributions. This means that clamping the loaded end of the specimen causes an increase in ILSS at high displacement levels, and, based on the positions shown in Table 4.17, causes the critical shear strain location to move closer to the loaded end of the specimen (higher X-position).

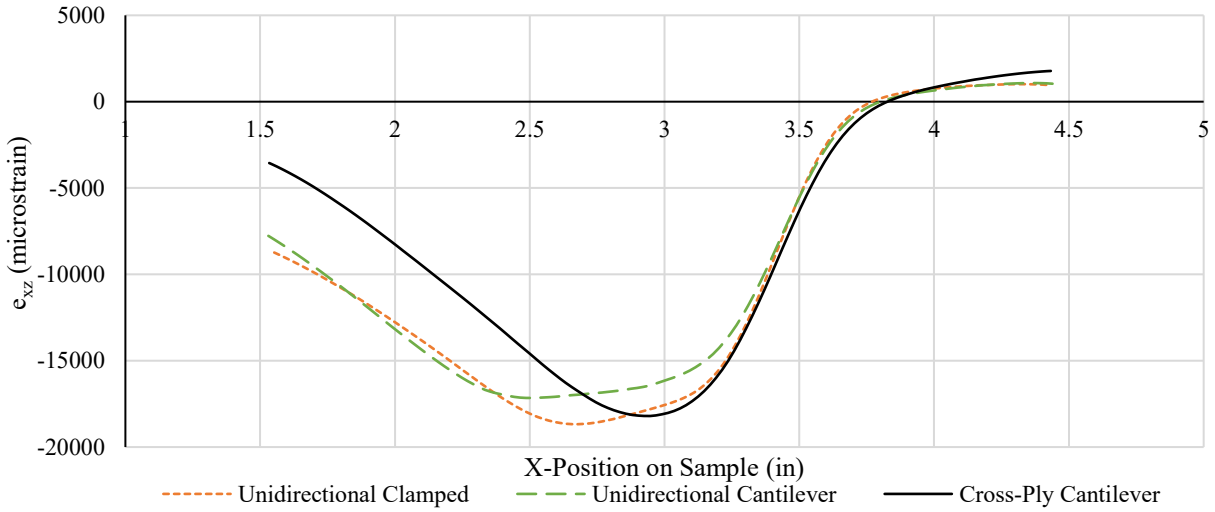

Figure 4.65: Side surface shear strain, e_{xz}, along the midplane for each 80-layer specimen configuration at failure

4.4.3 Unidirectional Cantilever Configuration Comparison

With regards to the 40-layer configuration, despite not being able to fail, the results will be presented at maximum actuator extension, which results in a specimen displacement of 59 mm. However, before analyzing the strains at failure, the critical side surface ILSS at 9.45 mm of specimen displacement are presented in Table 4.18 for the 40-, 60-, and 80-layer unidirectional cantilever configurations, along with their corresponding locations on the specimen surface. It is interesting to see that, regardless of specimen thickness, the maximum ILSS occur at almost the same location for each configuration, except for the small difference in through-thickness position for the 80-layer configuration. The same data is shown in Table 4.19 except at each configuration's respective maximum displacements.

Table 4.18: Critical side surface shear strains, in microstrain, for 40-, 60-, and 80-layer unidirectional cantilever configurations at 9.45 mm displacement

	40 Layers		60 Layers		80 Layers	
Position	**X (in)**	**Z (%thick)**	**X (in)**	**Z (%thick)**	**X (in)**	**Z (%thick)**
	2.86	50	2.88	50	2.9	55
Strain	-1044		-2956		-5197	

Table 4.19: Critical side surface shear strains, in microstrain, for 40-, 60-, and 80-layer unidirectional cantilever configurations at maximum displacement

	40 Layers		60 Layers		80 Layers	
Failure Displacement	**59 mm**		**45 mm**		**38 mm**	
Position	**X (in)**	**Z (%thick)**	**X (in)**	**Z (%thick)**	**X (in)**	**Z (%thick)**
	3.13	50	2.91	50	2.50	50
Strain	-13,302		-16,342		-17,155	

Figure 4.66 shows the side surface ILSS along the midplane of the 40-, 60-, and 80-layer unidirectional cantilever configurations at their respective maximum displacements. It is interesting to see how the location of maximum ILSS magnitude moves further from the loaded end of the specimen as specimen thickness increases. This means that for a tapered specimen, the critical locations for ILSS is farther from the tapered section in thicker specimens. Also, the area over which the shear strain is largest increases with increasing specimen thickness. This makes sense since the effect of shear properties increases with increasing specimen thickness.

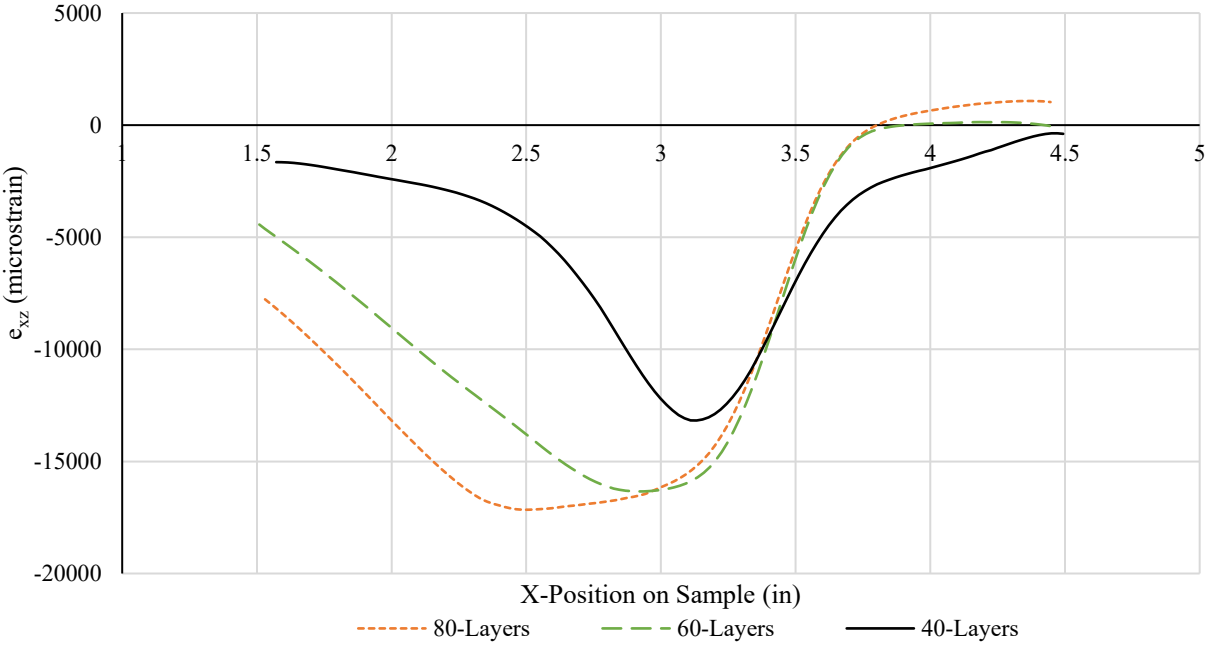

Figure 4.66: Side surface shear strain, e_{xz}, along the midplane for 40-, 60-, and 80-layer unidirectional cantilever specimen configuration at maximum displacement

4.5 Failure Analysis

A Progressive Damage Model (PDM) was developed in conjunction with this study as part of this project to predict failure initiation and propagation in the plate. PDM, as applied to finite element analysis, starts with the stress analysis of an initial model to compute the stresses in each element. In this approach, the Hashin failure criterion was used to find the elements which failed at each load step. Figure 4.67 shows the PDM model that is utilized in this study. The Hashin failure criterion also provides the mode of failure. Table 4.20 summarizes the Hashin failure criteria. In the present model each element is checked according to each of the Hashin failure modes.

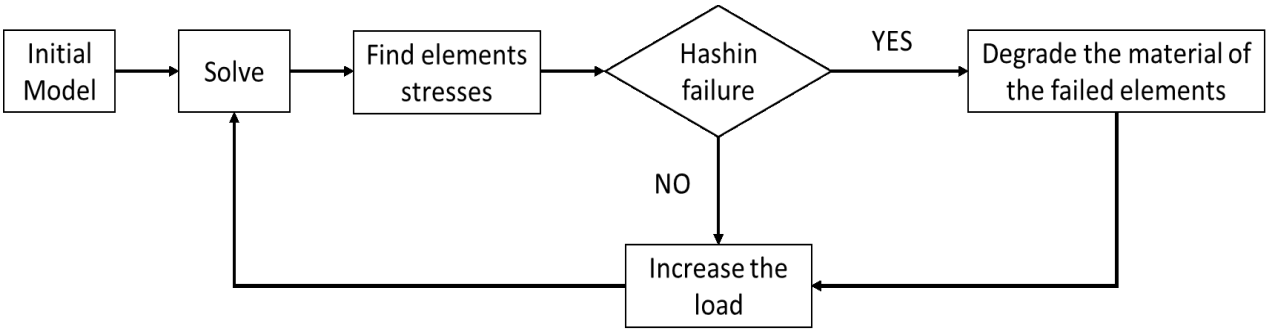

Figure 4.67: The Progressive Damage Model process

Table 4.20: Hashin failure criteria

Failure Modes and Criteria	
Matrix Tensile Cracking 1) $(\frac{\sigma_{yy}}{Y_T})^2 + (\frac{\sigma_{xy}}{S_{xy}})^2 + (\frac{\sigma_{yz}}{S_{yz}})^2 \geq 1$	Fiber-Matrix Shear Out 5) $(\frac{\sigma_{xx}}{X_C})^2 + (\frac{\sigma_{xy}}{S_{xy}})^2 + (\frac{\sigma_{xz}}{S_{xz}})^2 \geq 1$
Matrix Compressive Cracking 2) $(\frac{\sigma_{yy}}{Y_C})^2 + (\frac{\sigma_{xy}}{S_{xy}})^2 + (\frac{\sigma_{yz}}{S_{yz}})^2 \geq 1$	Delamination Tensile 6) $(\frac{\sigma_{zz}}{Z_T})^2 + (\frac{\sigma_{xz}}{S_{xz}})^2 + (\frac{\sigma_{yz}}{S_{yz}})^2 \geq 1$
Fiber Tensile Failure 3) $(\frac{\sigma_{xx}}{X_T})^2 + (\frac{\sigma_{xy}}{S_{xy}})^2 + (\frac{\sigma_{xz}}{S_{xz}})^2 \geq 1$	Delamination Compressive 7) $(\frac{\sigma_{zz}}{Z_C})^2 + (\frac{\sigma_{xz}}{S_{xz}})^2 + (\frac{\sigma_{yz}}{S_{yz}})^2 \geq 1$
Fiber Compressive Failure 4) $(\frac{\sigma_{xx}}{X_C}) \geq 1$	X: Fiber Direction Y: Transverse to fibers Z: Thickness direction

After verification at the end of each load step, the material properties of the failed elements are degraded according to the failure mode. The degradation scenario also decides a degrading percentage, which is controlled by the designer. In this study, four degradation scenarios were defined:

1. Matrix degradation: was applied to criteria 1 and 2, reduced E_y, G_{xy}, and G_{yz}
2. Fiber degradation: was applied to criteria 3 and 4, reduced all material properties
3. Shear out degradation: was applied to criterion 5, reduced G_{xy}
4. Delamination degradation: was applied to criteria 6 and 7, reduced E_z, G_{xz}, and G_{zy}

Degradation scenarios 1, 3 and 4 are not able to be overwritten by each other, meaning that only one can be applied to a given element. However, scenario 2 can be applied to an element which has already been degraded due to scenarios 1, 3 or 4. In other words, it can be said that if one element fails due to matrix failure, shear out or delamination it can fail again due to fiber failure and subsequently have its properties further degraded. During the experimental tests, it was observed that from a failure point of view, the fixed end of the sample is more critical due to load introduction at the bolted joint. Therefore, to reduce the failure analysis time, which required running the model for 20 to 30 load steps, it was decided to only consider the fixed end of the plate up to the edge of buffer pad for failure analysis. Figure 4.68 (Figure 3.12 repeated) shows the section of the specimen modeled to perform the failure analysis.

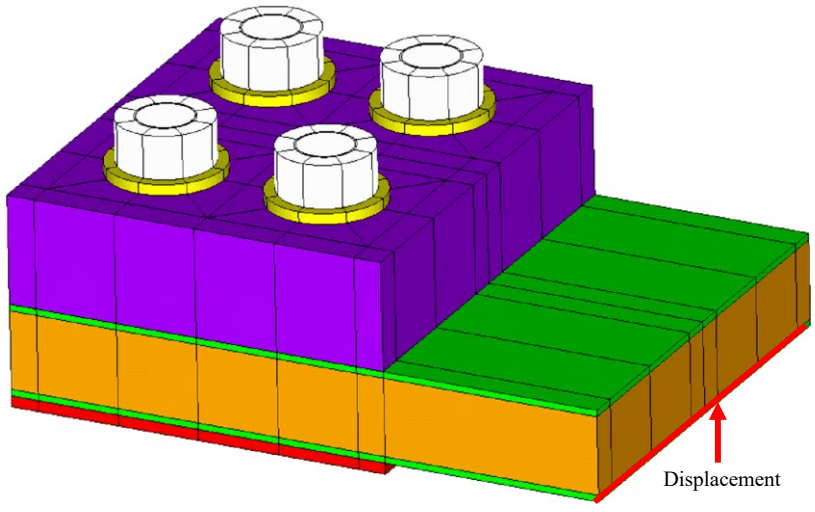

Figure 4.68: Reduced cantilever model for failure analysis (Figure 3.12 repeated)

In order to find the relationship between the displacement of the actuator and the displacement at the edge of the buffer pad, two analyses were performed using the full cantilever ANSYS model of Figure 3.11. It was found that at 10 mm actuator displacement, the displacement at the edge of buffer pad is 1.104 mm and at 25 mm of actuator displacement, the displacement at buffer edge is 2.346 mm. Assuming that the relationship between these two displacements is linear, it was obtained that the displacement at the buffer pad edge is equal to an actuator displacement multiplied by 0.0961. This value was used to map the displacement of the buffer pad edge to the actuator displacement.

4.5.1 ANSYS Failure Analysis Results

The results of failure analysis for the reduced cantilever model were obtained for actuator displacements of 10 to 68 mm at increments of 2 mm on the unidirectional model only. Figure 4.69 shows the failure propagation from side and isometric views at the indicated actuator displacement levels. It was observed that the first failed elements appeared at the edge of the bolt holes furthest from the specimen's fixed end at 12 mm of actuator displacement. The failure propagates around the bolt holes until an actuator displacement of 22 mm, at which point the elements along the edge of the top steel plate failed due to the stress concentration at that position. Then these two failed areas propagate in the region between the bolt holes and the steel plate edge. At an actuator displacement of 46 mm, which corresponds to the experimental failure displacement of the 80-layer unidirectional cantilever configuration, the first failed elements appeared at the thickness side of the plate around the region of critical ILSS. DIC also confirmed the appearance of the failure crack on the side surface of the specimen at this displacement. The position of the failed elements across the thickness corresponds very well with the cracks observed during experiment.

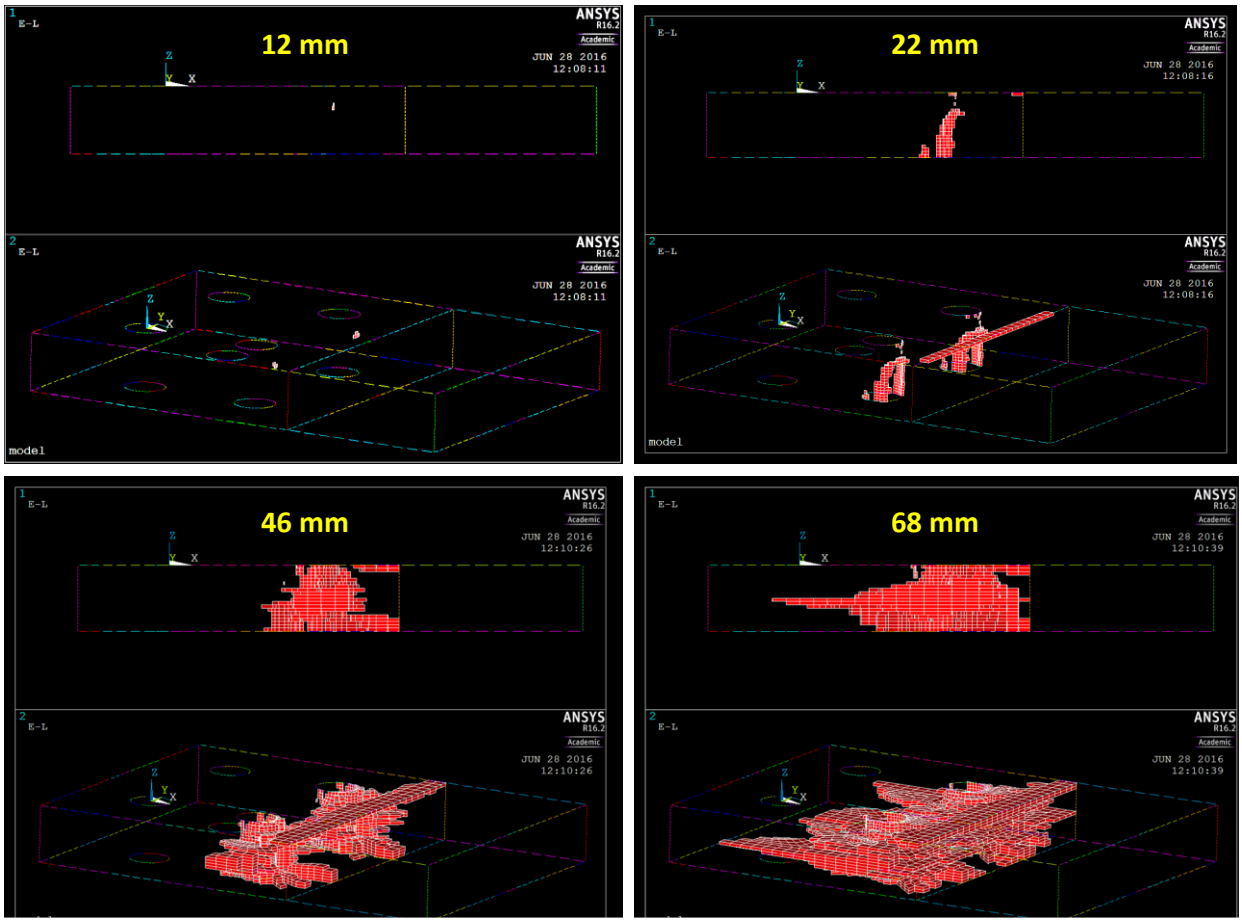

Figure 4.69: Failed elements from ANSYS simulation at various critical actuator displacement levels

4.5.2 Failure Comparison Between ANSYS and Experiment

To compare the failure analysis results with experimental results, the failed samples were sectioned across their width at 0.75-inch intervals. A low viscosity ink was used to make the cracks more visible. The cross-sections were then used to model the crack surfaces in CATIA. Figure 4.70 shows the characteristic transverse and shear-out crack surfaces for a unidirectional sample along with the delamination surface, shown separately for clarity. It should be noted that regardless of sample configuration, the unidirectional samples all exhibited similar crack surfaces. Figure 4.71 shows the delamination crack surface for a cross-ply sample. As to be expected, the cross-ply samples had the failure delamination completely contained between the middle two 90-degree plies, as the mismatch of orientation between plies would prevent the formation of through thickness cracks. All three cross-ply samples showed a change of delamination plane at about X = 3 inches, which corresponds to the location just in front of the most highly stressed bolt holes,

where the delamination crack shifts from the upper middle 90-degree ply to the lower one. This shift is shown in Figure 4.72.

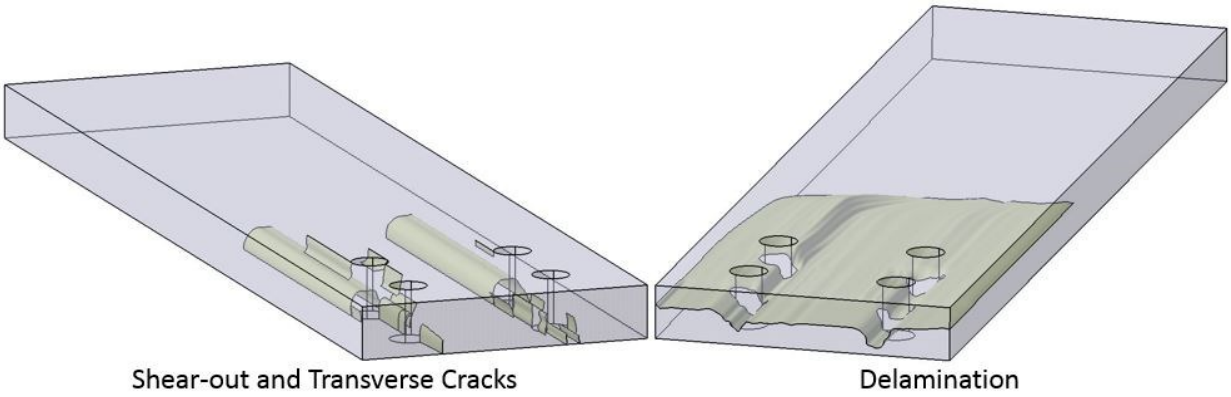

Figure 4.70: Characteristic shear-out and transverse cracks (left) and failure delamination (right) of unidirectional samples

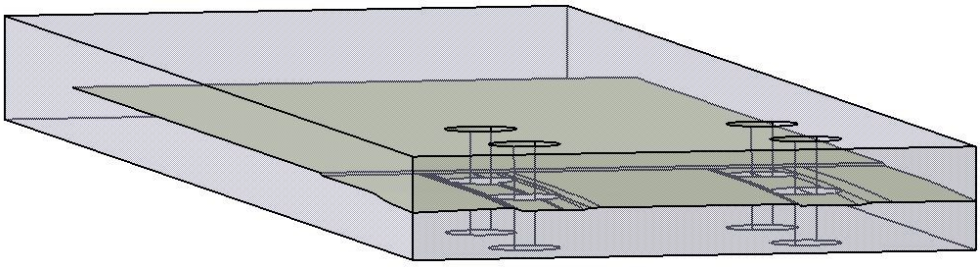

Figure 4.71: Characteristic failure delamination of a cross-ply sample

Figure 4.72: Cross-ply failure delamination plane shift on the side surface

Although the ANSYS model continued up to a simulated actuator displacement of 68 mm, the experimental 80-layer unidirectional cantilever configuration failed at an actuator displacement of 46 mm, which corresponds to the appearance of failed ANSYS elements on the side surface of the model. It is understood that despite the damage growing progressively in the ANSYS model, in reality cracks propagate catastrophically. This resulted in the thin surface-like cracks seen in Figure 4.70 as opposed to the larger simulated damage area shown in Figure 4.69. The following factors caused the discrepancy between the development of the failed area at an actuator displacement of 46 mm between ANSYS and experiments:

1. The model has been modified to reduce the number of elements and running time. The relationship between actuator displacement and displacement at the buffer pad edge was assumed to be linear. This assumption is more valid at lower displacements because the deformation of the specimen is minimal. At higher displacements it is not possible to correlate these two displacements linearly. Using a more powerful computer would help to consider the complete cantilever or clamped model for failure analysis, negating the need to correlate the above two displacements.
2. During failure simulation, only the elements positioned below the steel plate were analyzed, while in the experiment it was observed that the failure will propagate beyond that region toward the loaded end. This difference is noticeable in the modeled crack surfaces of Figure 4.70 extending well beyond the bolt holes. It is possible to perform the failure analysis over the whole of the plate, but that will increase the processing time.
3. In the simulation, the steel plate has a sharp edge which will cause a high stress concentration, while the real steel plate does not have a sharp edge. Therefore, the failure due to stress concentration at the steel plate edge was not observed during tests. Changing the shape of the steel plate edge in ANSYS can be an option to rectify this discrepancy, but for the proposed model it is not a good option because it will affect the meshing method of the steel plate, which would make it impossible to keep the harmony of the meshing pattern in the contact areas.

As a result, it was decided to continue running the failure model to develop the failure over a larger region. As such, the analysis continued up to 68 mm of actuator displacement (based on the linear correlation between buffer edge and actuator displacements). Figure 4.73 and Figure 4.74 compare the failure propagation pattern between ANSYS (at an assumed actuator displacement of 68 mm) and the experimental results at the sections illustrated in the figures. It is interesting to note how the delamination cracks do not occur at the midplane of the specimens. Instead, they appear to reach the side surface in the range of 65% to 75% thickness. They also appear to originate from in between the bolt holes and propagate towards the edge. This means that despite ILSS appearing to be the critical strains, the stress concentration introduced by the bolt holes is the source of failure. This is also evidenced by the failed elements

representing the delamination region through the thickness of the ANSYS cross-section being evenly distributed in the 25% to 75% thickness range, while still coinciding with experimental results.

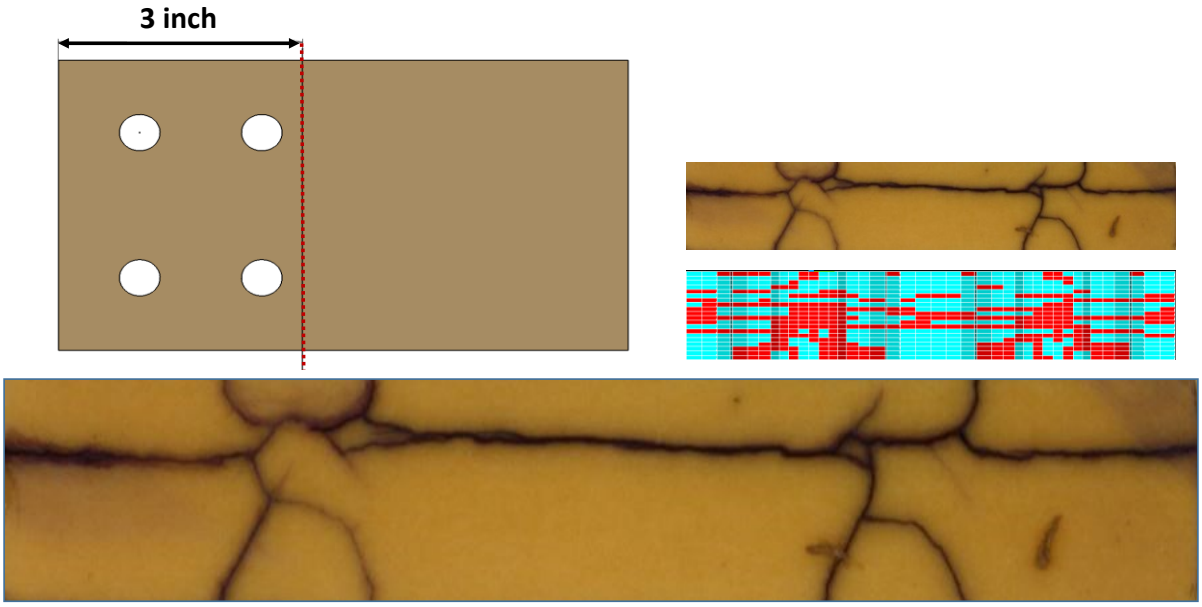

Figure 4.73: Comparison of the failure propagation at the section X = 3 inches

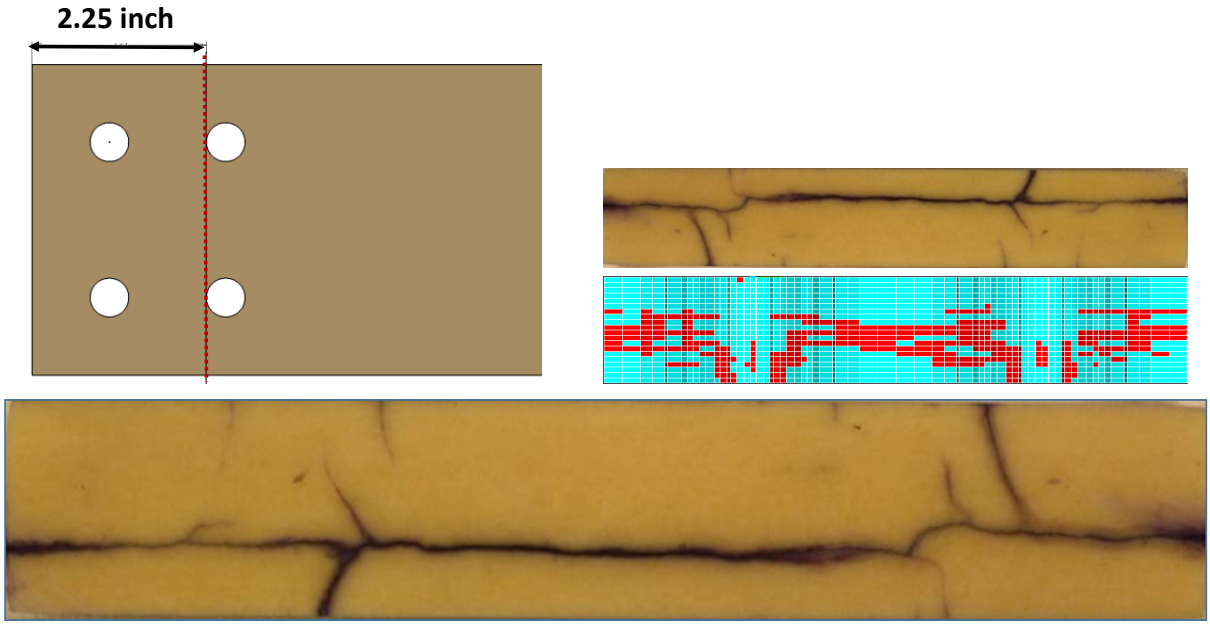

Figure 4.74: Comparison of the failure propagation at the section X = 2.25 inches

CHAPTER 5 CONCLUSIONS

In this study, glass/epoxy composite plates were manufactured and tested in flexural bending. Specimens of 20, 40, 60, and 80 unidirectional layers, and 80 cross-ply layers were tested in a cantilever-type configuration, where the loaded end of the specimen was clamped between cylindrical faces of a loading fixture to allow rotation of the specimen end. Specimens of 80 unidirectional layers were also tested in a clamped configuration where the loaded end of the specimen was clamped between steel plates. The specimens were prepared with buffer pads between the laminate and fixtures to reduce stress concentrations at the fixture edges. The 80-layer clamped specimens were fabricated to the specifications provided by the industrial partner, as this was the configuration of greatest interest to them. The other configurations were added to this study to allow correlation with theoretical analysis, as clamping of the loaded end of the specimen makes theoretical calculation very difficult. The manufacturing process was vetted for consistency by performing TGA and DSC analysis on the cured samples, measuring their thicknesses and calculating the fibre volume fraction and void content. The quality assurance analysis showed good manufacturing consistency.

The experimental load-displacement results were compared to theoretical results calculated using classical laminate theory as well as a monodimensional beam theory, which adds a shear correction factor to classical laminate theory to account for shear influence in calculating the deflection of a cantilever beam. To calculate the shear correction coefficient of a composite beam with a layup sequence in the form of $[0/90]_{\Omega s}$, where Ω can be any integer, the equations from the monodimensional approach presented by Gay *et al.* [30] were simplified as closely as possible to analytical form. As part of the theoretical calculations, the shear correction coefficient was charted versus laminate thicknesses up to 120 cross-ply layers to show the asymptotic nature of the shear correction coefficient trending towards the homogenous beam value of $k = 1.2$. Calculations were also presented to show the importance of material properties towards the accuracy of MBT. By reducing the buffer pad properties by about half, the error between theoretical deflection calculations for the 20-layer unidirectional configuration reduced from 9% to effectively 0%.

However, when specimen thickness increased beyond a certain level, the influence of material properties on the accuracy of the theory was reduced, resulting in a change in error for the 80-layer unidirectional configuration from 52% to 48%. Results showed diverging correlation between theory and experiment as specimen thickness increased for both MBT and CLT. This is a commonly understood limitation of the theories; they become less accurate as specimen thickness increases due to its inability to properly account for the increasing influence of shear properties. However, when specimen layup sequence was changed from unidirectional to cross-ply, the MBT calculation was considerably more accurate than the CLT calculation. This was due in part to the fact that MBT, which is an extension of first order shear deformation theory, assumes a fixed shear correction coefficient for unidirectional beams (i.e. beams with a homogenous cross-section), regardless of specimen thickness. Conversely, the calculation of the shear correction coefficient for a cross-ply laminate does take the specimen thickness into account.

By charting the maximum displacements of the unidirectional cantilever specimens versus specimen thickness, the existence of a size effect, as it relates to composite plates in bending, was seen in the resulting nonlinear relationship. All configurations except the 80-layer unidirectional cantilever one, showed good repeatability between samples in the load-displacement curves. It was discovered while testing the 80-layer unidirectional cantilever specimens, that the cantilever fixture was the source of discrepancy between specimen results as it originally did not grip the specimens tight enough to prevent excess rotation about the specimen end, which skewed the displacement results. The load-displacement behaviour of both the 80-layer unidirectional clamped and cantilever configurations was very similar. The clamping of the loaded end under a steel plate had little effect on the ultimate loads and displacements of this configuration, although, at low displacement levels, the clamped configuration appeared to behave about 12% more stiffly than the cantilever configuration. The cross-ply samples behaved expectedly less stiffly than the unidirectional counterparts by about 30%. Comparing the load-displacement curves to maximum displacement of the unidirectional cantilever configurations for each thickness revealed that the specimens behaved less linearly as thickness increased. This is evidence of the increasing influence of shear properties with increasing thickness.

In the early stages of the study, the specimens were tested with a strain gauge array to capture top surface axial and transverse strains, and side surface shear strains. After some trials, this method was abandoned for digital image correlation (DIC), which allowed for full field strain measurement of the specimen surfaces. As part of this study, a finite element model was created in ANSYS for strain calculation. DIC results were compared to both strain gauge data and ANSYS results for validation. In areas of high strain, the results showed good correlation between strain gauge, DIC, and ANSYS. In these critical areas that were not near edges that may reduce the accuracy of DIC measurements, the difference between DIC and ANSYS was less than 10%. Also, around the area where ILSS is the highest, the difference between DIC and strain gauge was only 5%, which is a significant achievement in terms of correlation with experiments. DIC also provides the benefit of full field strain measurement over the spot measurements provided by strain gauges. For the regions with lower strain (less than 500 microstrain), the correlation is not as good compared to the other areas. However, by considering the accuracy of the DIC (about +/- 50 microstrain) the ANSYS results are still in an acceptable agreement with DIC. The ANSYS model's accuracy in terms of strain prediction is higher for critical strains (ex. axial strain, e_{xx}, and interlaminar shear strain, e_{xz}). The model was able to predict the strain in both cantilever and clamped boundary conditions. In addition, it was validated in both unidirectional and cross-ply layup sequences. However, the model required some simplifications in terms of geometry and load application to be able to be run within a reasonable time frame. These must be taken into consideration when analyzing the results, especially for failure. Despite thickness measurements of the specimens being within an acceptable level of variance, due to the nature of the sample manufacturing process (i.e. vacuum bagging parts instead of cavity moulding), the samples did not have perfectly parallel surfaces as a result of resin bleeding from the corners. This may be a source of discrepancy between ANSYS, DIC, and strain gauge results. Also, while bolting the samples to the test setup, it was discovered after several samples had already been tested that the samples rotated about the Z-axis. Although several efforts were made to mitigate this rotation, it was not completely avoidable. Loading the samples while they were not perfectly perpendicular to the support edge caused a slight twisting of the samples. This is another source of discrepancy between experimental and finite

element results. Despite some discrepancies between theoretical and experimental results, the strain gauge data allowed for the validation of DIC up to specimen failure for critical strains. At low displacement levels, the 80-layer unidirectional configurations experienced similar maximum ILSS, while the cross-ply configuration saw a maximum ILSS magnitude about 8% lower. DIC also showed that the area over which these strains are critical is smaller for the cross-ply configuration. At failure, clamping of the loaded end of the specimen resulted in an ILSS that was about 8% higher than for the cantilever configuration, but only 2.5% higher than the cross-ply configuration. When comparing the failure strains for the different unidirectional cantilever thicknesses, it was seen that the area over which the shear strains are critical grows larger with increasing specimen thickness. However, the location of maximum ILSS is about the same for all unidirectional cantilever configurations.

To finalize the ANSYS model, it was expanded to model the failure of the composite beams by employing a progressive damage model approach. The elements that failed a Hashin Failure Criteria test were highlighted after each load step and their properties were degraded before moving to the next load step. All unidirectional specimens failed with the same failure crack patterns. These included shear-out cracks initiating on the tension side of the specimens from the more highly loaded bolt holes and propagating towards the loaded end, through-thickness transverse cracks that propagate on the compression side of the samples from the highly loaded bolt holes towards the loaded end and on the tension side of the specimen from the bolt holes towards the fixed end of the specimen, and delamination cracks that appeared on the side surface in the range of 65% to 75% thickness. The failure model was able to predict where failure would occur as well as the displacement at which the failure cracks would reach the side surface of the specimen, coinciding with the catastrophic failure of experimental tests. However, since cracks occur catastrophically in reality and because of the progressive nature of the model, it is not possible to correlate the appearance of failed elements exactly with the initiation of cracks heard during testing. The cross-ply specimens failed predictably with a delamination at the middle 90-degree layers. What was interesting about the failure was the shift in delamination plane that coincides with the edge of the bolt holes that were the source of stress concentration. The sources of discrepancy include the simplifications made in determining

the displacement to apply to the reduced cantilever ANSYS model, the limited number of elements that were analyzed for failure, and the sharp edge stress concentration included in the steel plates of the model that does not reflect the fileted edges of the steel plates used in experiments.

CHAPTER 6 CONTRIBUTION AND FUTURE WORK

From the experimental work performed on glass/epoxy composite plates in quasi-static flexural bending, the following contributions have been made:

1) A simplified method was developed for calculating the shear correction coefficient of a cross-ply symmetric laminate with a layup sequence of the form $[0/90]_{\Omega s}$ based on the monodimentional approach presented by Gay *et al.* [30].
2) The load-displacement curves to failure were presented for laminates of 60 and 80 unidirectional layers, as well as 80 cross-ply layers in a cantilever type configuration, and 80 unidirectional layers with the loaded end clamped. This data can be used to validate failure models for these types of laminates. This data also provided the ultimate loads used to calculate the various fatigue load levels in [25]. The load-displacement curves up to a high displacement level were also presented for unidirectional laminates of 20 and 40 layers in a cantilever type configuration.
3) The bolted joint provides insight into the effect this type of connection has on the bending behaviour of composite laminates. It was the source of catastrophic failure initiation of the samples and created similar crack patterns in all failed specimens.
4) The load-displacement data at small displacement levels for all cantilever configurations tested was compared to theoretical calculations from a monodimensional beam theory and classical laminate theory. The results illustrated some of the limitations of the theories. The experimental results can be used to validate more accurate theories.
5) The maximum displacements of the 40-, 60-, and 80-layer unidirectional cantilever configurations were used to illustrate how the size effect affects composite laminates in bending.
6) Digital image correlation was validated for full-surface strain measurement up to very high strain and displacement levels. The measured strains were used to validate a fully parametric ANSYS model in [38] that can be used for more diverse and detailed studies without the expense involved in mechanical testing.

7) The failed crack surfaces helped validate the progressive damage model of the ANSYS simulation.

For further investigation related to this work, the following aspects can be considered:

1) The load-displacement analysis can be extended to include the failures of thinner and thicker samples to provide more experimental data that can be used to validate higher order theories.
2) The existing ultimate loads can be used to design further fatigue experiments.
3) Other layup sequences can be tested to expand the data base of experimental results. Moreover, the boundary conditions can be changed to either eliminate the bolted connection at the fixed end to be closer to pure cantilever bending, or to add a bolted connection to the loaded end of more configurations which would be of greater interest to industry, as bolted connections are a common method of fixing composite parts to larger components and are an important source of stress concentration.
4) Strain calculations can be made to compare to the measurements collected. This would provide a more insight into the limits of different strain calculation theories.
5) The experimental data can be used to help develop a failure theory for composite plates in bending.

REFERENCES

1. Hoa, S.V. "Principles of the Manufacturing of Composite Materials." Lancaster, USA: DEStech Publications Inc., 2009. p. 174-175. ISBN: 978-1-932078-26-8.
2. Stringer, L.G. "Optimization of the wet lay-up/vacuum bag process for the fabrication of carbon fibre epoxy composites with high fibre fraction and low void content." *Composites*, 1989. 20(5): p. 441-452. https://doi.org/10.1016/0010-4361(89)90213-9.
3. Kardos, J.L., *et al*. "Void formation and transport during composite laminate processing: an initial model framework." *ASTM Special Technical Publication*, 1983. 797: p. 96-109.
4. Koushyar, H., *et al*. "Effects of variation in autoclave pressure, temperature, and vacuum-application time on porosity and mechanical properties of a carbon fiber/epoxy composite." *Journal of Composite Materials*, 2012. 46(16): p. 1985-2004. https://doi.org/10.1177/0021998311429618.
5. Bogetti, T.A. and Gillespie, J.W. "Two-dimensional cure simulation of thick thermosetting composites." *Journal of Composite Materials*, 1991 25(3): p. 239-273. https://doi.org/10.1177/002199839102500302.
6. Young, W. "Compacting pressure and cure cycle for processing of thick composite laminates." *Composites Science and Technology*, 1995. 53(3): p. 299-306. https://doi.org/10.1016/0266-3538(95)00067-4.
7. Xin, C., *et al*. "Online monitoring and analysis of resin pressure inside composite laminate during zero-bleeding autoclave process." *Polymer Composites*, 2011. 32(2): p. 314-323. DOI: 10.1002/pc.21048.
8. Hojjati, M. and Hoa, S.V. "Model laws for curing of thermosetting composites." *Journal of Composite Materials*, 1995. 29(13): p. 1741-1761. https://doi.org/10.1177/002199839502901305.
9. Kim, J.S. and Lee, D.G. "Development of an autoclave cure cycle with cooling and reheating steps for thick thermoset composite laminates." *Journal of Composite Materials*, 1997. 31(22): p. 2264-2282. https://doi.org/10.1177/002199839703102203.
10. Oh, J.H. and Lee, D.G. "Cure Cycle for Thick Glass/Epoxy Composite Laminates." *Journal of Composite Materials*, 2002. 36.1: p. 19-45. https://doi.org/10.1177/0021998302036001300.
11. Olivier, P. and Cavarero, M. "Comparison between longitudinal tensile characteristics of thin and thick thermoset composite laminates: influence of curing conditions." *Computers and Structures*, 2000. 76(1-3): p. 125-137. https://doi.org/10.1016/S0045-7949(99)00161-3.
12. Rai, N. and Pitchumani, R. "Rapid cure simulation using artificial neural networks." *Composites Part A: Applied Science and Manufacturing*, 1997. 28(9-10): p. 847-859. https://doi.org/10.1016/S1359-835X(97)00046-8.
13. Zhang, Z. and Friedrich, K. "Artificial neural networks applied to polymer composites: a review." *Composites Science and Technology*, 2003. 63(14): p. 2029-2044. https://doi.org/10.1016/S0266-3538(03)00106-4.
14. Bheemreddy, V., *et al*. "Process modeling of cavity molded composite flex beams." *Finite Element in Analysis and Design*, 2014. 78: p. 8-15. https://doi.org/10.1016/j.finel.2013.09.003.
15. Bheemreddy, V., *et al*. "Process optimization of composite flex beams using neural networks." *SAMPE 2013 Conference and Exhibition: Education and Green Sky - Materials Technology for a Better World*. Society for the Advancement of Material and Process Engineering, 2013. p. 2447-2461. https://www.researchgate.net/publication/267632820_Process_Optimization_of_Composite_Flex_Beams_using_Neural_Networks.
16. Ruiz, E. and Trochu, F. "Numerical analysis of cure temperature and internal stresses in thin and thick RTM parts." *Composites Part A: Applied Science and Manufacturing*, 2005. 36(6) (2005): 806-826. https://doi.org/10.1016/j.compositesa.2004.10.021.

17. Mamani, S. and Hoa, S.V. "Temperature measurement in autoclave manufacturing process for thick glass/epoxy composite laminate." *Proceedings of International Workshop on Mechanical Behavior of Thick Composites*. Montreal, Canada: DEStech Publications Inc., 2016.
18. Reddy, J.N. and Chao, W.C. "Non-linear bending of thick rectangular, laminated composite plates." *International Journal of Non-Linear Mechanics*, 1981. 16(3-4): p. 291-301. https://doi.org/10.1016/0020-7462(81)90042-1.
19. Kapania, R.K. and Raciti, S. "Recent Advances in Analysis of Laminated Beams and Plates, Part I: Shear Effects and Buckling." *AIAA Journal*, 1989. 27(7): p. 923-934. DOI: 10.2514/3.10202.
20. Kant, T. and Swaminathan, K. "Estimation of Transverse/Interlaminar Stresses in Laminated Composites - A Selective Review and Survey of Current Developments." *Composite Structures*, 2000. 49(1): p. 65-75. https://doi.org/10.1016/S0263-8223(99)00126-9.
21. Mittelstedt, C. and Wilfried, B. "Interlaminar Stress Concentrations in Layered Structures: Part I - A Selective Literature Survey on the Free-Edge Effect since 1967." *Journal of Composite Materials*, 2004. 38(12): p. 1037-1062. https://doi.org/10.1177/0021998304040566.
22. Plagianakos, T.S and Saravanos, D.A. "Higher-order layerwise laminate theory for the prediction of interlaminar shear stresses in thick composite and sandwich composite plates." *Composite Structures*, 2009. 87(1): p. 23-35. https://doi.org/10.1016/j.compstruct.2007.12.002.
23. Whitney, J.M. and Pagano, N.J. "Shear deformation in heterogeneous anisotropic plates." *Journal of Applied Mechanics*, 1970. 37(4): p. 1031-1036. DOI: 10.1115/1.3408654.
24. Lalonde, S. *Investigation into the Static and Fatigue Behaviour of A Helicopter Main Rotor Yoke Made of Composite Materials*. Master Thesis. McGill University. Montreal, Canada, 2000. http://digitool.Library.McGill.CA:80/R/-?func=dbin-jump-full&object_id=30256&silo_library=GEN01.
25. Xiong, W. *Manufacturing and Fatigue Behaviour of Thick Glass/Epoxy Composite Beams*. Master Thesis. Concordia University. Montreal, Canada, 2016. https://spectrum.library.concordia.ca/981394/1/Xiong_MSc_F2016.pdf.
26. Zweben, C. "Designer's corner: Is there a size effect in composites?" *Composites*, 1994. 25(6): p. 451-454. https://doi.org/10.1016/0010-4361(94)90102-3.
27. Sutherland, L.S., Shenoi, R.A., and Lewis, S.M. "Size and scale effects in composites: I. Literature review." *Composites Science and Technology*, 1999. 59(2): p. 209-220. https://doi.org/10.1016/S0266-3538(98)00065-7.
28. Wisnom, M.R. "Size effects in the testing of fibre-composite materials." *Composites Science and Technology*, 1999. 59(13): p. 1937-1957. https://doi.org/10.1016/S0266-3538(99)00053-6.
29. Reddy, J.N. *Mechanics of Laminated Composite Plates and Shells Theory and Analysis*. Second Edition. Boca Raton: CRC Press LLC, 2004. ISBN: 0-8493-1592-1.
30. Gay, D., Hoa, S.V. and Tsai, S.W. *Composite Materials Design and Applications*. Boca Raton: CRC Press LLC, 2003. ISBN: 1-58716-084-6.
31. Lim, T.S., Kim, B.C., and Lee, D.G. "Fatigue characteristics of the bolted joints for unidirectional composite laminates." *Composite Structures*, 2006. 72(1): p. 58-68. https://doi.org/10.1016/j.compstruct.2004.10.013.
32. Kashaba, U.A., *et al*. "Effect of washer size and tightening torque on the performance of bolted joints in composite structures." *Composite Structures*, 2006. 73(3): 310-317. https://doi.org/10.1016/j.compstruct.2005.02.004.
33. Gorjipoor, A., *et al*. "Stress Analysis of a Thick Composite Laminate With a Bolted Joint." *Proceedings of the Tenth Joint Canada-Japan Workshop of Design, Manufacturing and Applications of Composites*. Vancouver, Canada: DEStech Publications Inc., 2015.
34. ASTM Standard D2584-11." *Standard Test Method for Ignition Loss of Cured Reinforced Resins*. ASTM International, 2000.
35. ASTM Standard D2734-09." *Standard Test Methods for Void Content of Reinforced Plastics*. ASTM International, 2009.
36. Sartorius. User Manual. *Density Determination Kit*. Available at www.sartorius.com.

37. Heer, C.S. *Flexural Test Setup*. Master of Engineering Report. Concordia University. Montreal, Canada, 2013.
38. Gorjipoor, A., Hoa, S.V., and Ganesan, R. "Numerical model for investigation of the strain distribution in thick composite plates subjected to bolt loads." *Aerospace Science and Technology*, 2016. 59: 94-102. https://doi.org/10.1016/j.ast.2016.10.008.
39. Gorjipoor, A., *et al*. "Computational and experimental strain analysis of flexural bending of thick glass/epoxy laminates." *Composite Structures*, 2017. 176(15): p. 526-538. https://doi.org/10.1016/j.compstruct.2017.05.066.
40. Hamidi, H. "Material Characterization Results for Orthotropic Material Properties." Internal Project Document CRIAQ COMP-509. Concordia University, 2015.
41. "ANSYS Workbench 16.0 Material Library." ANSYS.
42. "CYCOM E773 Epoxy Prepreg Technical Data Sheet." CYTEC Solvay Group. http://www.cytec.com/sites/default/files/datasheets/CYCOM_E773_032112.pdf.
43. *Industrial Laminate Specifications Glass-Based Phenolics NEMA G-3, G-5, G-7, G-9, G-10, G-11 Grades*. Boedeker Plastics Inc. http://www.boedeker.com/ilamg_p.htm.
44. Speck, J.A. *Mechanical Fastening, Joining, and Assembly*. Boca Raton: CRC Press, 2015. ISBN: 978-1-4822-7655-8.

APPENDIX A

The following steps show the derivation of the simplified method for calculating the shear correction coefficient, k, from the monodimensional approach presented in [30] that has been previously shown in section 1.3 (Theoretical Deflection of a Cantilever Composite Beam). This simplified method applies to cross-ply beams of any number of layers with a layup sequence in the form of $[0/90]_{\Omega s}$ and a rectangular cross-section of width b and layers of equal thickness, h, as seen in Figure A.1, below.

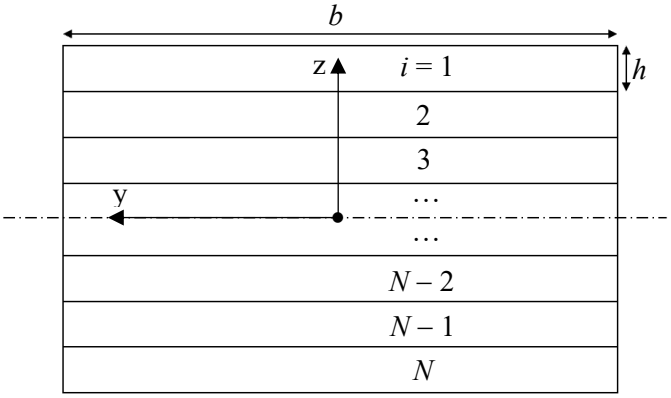

Figure A.1: Cross-section of a cross-ply laminate of *N* layers

We must first begin with the equivalent shear stiffnesses in Equation 1.3a, which is defined by:

$$\langle GS \rangle = \int_D G_i dS = \sum_{i=1}^{N} G_i S_i$$

Where N is the total number of layers and $i = 1$ corresponds to the top layer in the laminate. If we expand the summation above for a general layup sequence, we get:

$$\langle GS \rangle = \sum_{i}^{N} G_i S_i = G_1 S_1 + G_2 S_2 + G_3 S_3 \ldots + G_{N-1} S_{N-1} + G_N S_N$$

Understanding that for a $[0/90]_{\Omega s}$ laminate, all layers have the same shear stiffness, G_{12}, and cross-section area, $S = bh$, the above equation simplifies to Equation 1.6:

$$\langle GS \rangle = NbhG_{12}$$

Next, looking at the general equation for equivalent longitudinal stiffness from Equation 1.3b and expanding it for a general layup sequence, we get:

$$\langle EI_y \rangle = \sum_i E_i I_{yi} = E_1 I_{y1} + E_2 I_{y2} + E_3 I_{y3} \ldots + E_{N-1} I_{y(N-1)} + E_N I_{yN}$$

Now, for a symmetric cross-ply laminate with layers of alternating longitudinal stiffnesses E_1 and E_2, the equation becomes:

$$\begin{aligned}\langle EI_y \rangle = \sum_i E_i I_{yi} &= E_1 I_{y1} + E_2 I_{y2} + E_1 I_{y3} \ldots + E_2 I_{y(N-1)} + E_1 I_{yN} \\ &= E_1 \left(I_{y1} + I_{y3} \ldots + I_{y(N-2)} + I_{yN}\right) + E_2 \left(I_{y2} + I_{y4} \ldots + I_{y(N-3)} + I_{y(N-1)}\right) \\ &= E_1 \left[\left(I_{y1} + I_{yN}\right) + \left(I_{y3} + I_{y(N-2)}\right) \ldots + \left(I_{y\left(\frac{N}{2}-1\right)} + I_{y\left(\frac{N}{2}+2\right)}\right)\right] \\ &+ E_2 \left[\left(I_{y2} + I_{y(N-1)}\right) + \left(I_{y4} + I_{y(N-3)}\right) \ldots + \left(I_{y\frac{N}{2}} + I_{y\left(\frac{N}{2}+1\right)}\right)\right]\end{aligned}$$

To further simplify the equation, we must understand how to combine the second moment areas for symmetric plies. Figure A.2 shows how we can calculate the combined second moment area of plies 2 and N−1 by subtracting the second moment area of the darker shaded rectangle from the lighter one.

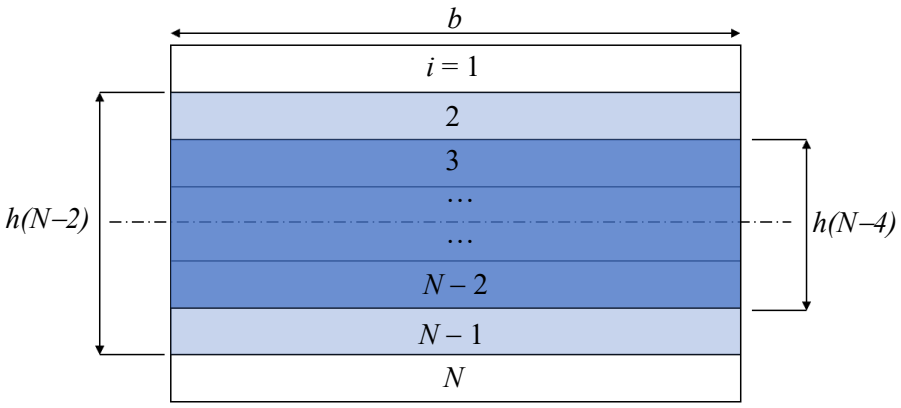

Figure A.2: Second moment area of symmetric plies

Using this combined area method, the combined second moment area of plies 2 and N−1 can be calculated by:

$$I_{y2} + I_{y(N-1)} = I_2 = \frac{b[h(N-2)]^3}{12} - \frac{b[h(N-4)]^3}{12} = \frac{bh^3}{12}\left[(N-2)^3 - (N-4)^3\right]$$

For any two symmetric plies, the equation becomes:

$$I_{yi} + I_{y(N-i+1)} = I_i = \frac{b[h(N-2i+2)]^3}{12} - \frac{b[h(N-2i)]^3}{12} = \frac{bh^3}{12}\left[(N-2i+2)^3 - (N-2i)^3\right]$$

Which is valid for $1 \leq i \leq \frac{N}{2}$ and is the same as what was shown in Equation 1.7. Applying this, the equation for longitudinal stiffness becomes:

$$\langle EI_y \rangle = \sum_i E_i I_{yi} = E_1 \left(I_1 + I_3 \ldots + I_{\frac{N}{2}-1} \right) + E_2 \left(I_2 + I_4 \ldots + I_{\frac{N}{2}} \right)$$

We now introduce a new variable $X = N/2 = 2\Omega$, and begin calculating the equivalent longitudinal stiffness for various values of X:

For a $[0/90]_s$ laminate ($N = 4$, $X = 2$),

$$\langle EI_y \rangle = E_1 \left[\frac{bh^3}{12} (4^3 - 2^3) \right] + E_2 \left[\frac{bh^3}{12} (2^3) \right] = \frac{bh^3}{12} (2^3)[E_1(2^3 - 1^3) + E_2(1^3)] = \frac{2bh^3}{3} [7E_1 + E_2]$$

For a $[0/90]_{2s}$ laminate ($N = 8$, $X = 4$),

$$\langle EI_y \rangle = E_1 \left[\frac{bh^3}{12} (8^3 - 6^3 + 4^3 - 2^3) \right] + E_2 \left[\frac{bh^3}{12} (6^3 - 4^3 + 2^3) \right]$$

$$= \frac{bh^3}{12} (2^3)[E_1(4^3 - 3^3 + 2^3 - 1^3) + E_2(3^3 - 2^3 + 1^3)] = \frac{2bh^3}{3} [44E_1 + 20E_2]$$

We can already see a pattern begin to emerge in the brackets that multiply E_1 and E_2. By following the pattern, we can tabulate the resulting coefficients that multiply E_1 and E_2 (let's call them $C(X)$ and $D(X)$) as X increases:

X	***C(X)***	***D(X)***
2	7	1
4	44	20
6	135	81
8	304	208
10	575	425
12	972	756
	…	

To see if $C(X)$ and $D(X)$ can be described by analytical equations, we employ the finite difference method to first see if they can be described by polynomial equations. This would simplify the equation of equivalent longitudinal stiffness to the form:

$$\langle EI_y \rangle = \frac{2bh^3}{3}[C(X)E_1 + D(X)E_2]$$

Applying the finite difference method to the values of *C(X)* looks like:

X	***C(X)***							
2	7							
		>	37					
4	44			>	54			
		>	91			>	24	
6	135			>	78			
		>	169			>	24	
8	304			>	102			
		>	271			>	24	
10	575			>	126			
		>	397					
12	972							
			m = 1		m = 2		m = 3	

As we can see, the difference between adjacent cell values becomes constant in the third round at m = 3. This means *C(X)* can be define by a polynomial of order 3. Or in general:

$$C(X) = aX^3 + bX^2 + cX + d, \qquad c = d = 0$$

Using the values for *C(X)* to find the coefficients of the equation, we can see that:

$$C(X) = \frac{X^3}{2} + \frac{3X^2}{4}$$

Using the same method, we find that *D(X)* can be described by:

$$D(X) = \frac{X^3}{2} - \frac{3X^2}{4}$$

Remembering that *X = N/2*:

$$C(N) = \frac{N^3 + 3N^2}{16}$$

$$D(N) = \frac{N^3 - 3N^2}{16}$$

And thus, we end up with the same equation for equivalent longitudinal stiffness as what was shown in Equation 1.8:

$$\langle EI_y \rangle = \frac{2bh^3}{3}[C(N)E_1 + D(N)E_2] = \frac{2bh^3}{3}\left[E_1\left(\frac{N^3+3N^2}{16}\right) + E_2\left(\frac{N^3-3N^2}{16}\right)\right]$$

Now that we can calculate the equivalent stiffnesses for any value of N that is an integer multiple of 4 (i.e. $N = 4, 8, 12, 16$, etc.), we can move on to the warping function, g_o, and its coefficients. The warping function was defined in section 1.3 (Theoretical Deflection of a Cantilever Composite Beam) as being the solution to the problem:

$$\begin{cases} \nabla^2 \mathrm{g}_o = -\dfrac{E_i}{G_i}\dfrac{\langle GS \rangle}{\langle EI_y \rangle} \times z \text{ in the domain } D \\ \dfrac{\partial \mathrm{g}_o}{\partial n} = 0 \text{ on the boundary } \partial D \end{cases}$$

The internal continuity of the warping function must be maintained. This means that the following conditions must be satisfied at each layer boundary:

$$\left.\begin{array}{c} \mathrm{g}_{oi} = \mathrm{g}_{oj} \\ G_i \dfrac{\partial g_{oi}}{\partial n} = G_j \dfrac{\partial g_{oj}}{\partial n} \end{array}\right\} \text{ along internal boundaries } l_{ij}$$

Taking into account the antisymmetry of the warping function with respect to z for a symmetric cross-ply laminate, the general solution for g_{oi} is:

$$\mathrm{g}_{oi} = -\frac{E_i}{G_i}\frac{a}{6}{z_i}^3 + A_i z_i + B_i$$

Where

$$a = \frac{\langle GS \rangle}{\langle EI_y \rangle}$$

$$B_{\frac{N}{2}} = 0$$

$$B_{N-i+1} = -B_i$$

$$z_i = h(X - i + 1)$$

Beginning with g_{o1}, if we apply the boundary conditions stated above, we get:

$$\frac{\partial \mathrm{g}_{o1}}{\partial z} = 0 \; at \; z_1 = hX \; (the \; upper \; boundary)$$

$$0 = -\frac{E_1}{G_{12}}\frac{a}{2}(hX)^2 + A_1$$

$$A_1 = \frac{E_1}{G_{12}}\frac{a}{2}(hX)^2$$

Now applying the next boundary condition, we get

$$G_{12}\frac{\partial g_{o1}}{\partial z} = G_{12}\frac{\partial g_{o2}}{\partial z} \; at \; z_2 = h(X-1)$$

$$-\frac{E_1}{G_{12}}\frac{a}{2}[h(X-1)]^2 + A_1 = -\frac{E_2}{G_{12}}\frac{a}{2}[h(X-1)]^2 + A_2$$

Replacing A_1, we get

$$-E_1\frac{a}{2}[h(X-1)]^2 + E_1\frac{a}{2}(hX)^2 = -E_2\frac{a}{2}[h(X-1)]^2 + G_{12}A_2$$

$$A_2 = \frac{ah^2}{2G_{12}}\{E_1[X^2 - (X-1)^2] + E_2(X-1)^2\}$$

It can be seen that calculating each subsequent A_i depends on the value of the previous one, until the last A_i is calculated for the middle ply. Continuing in this fashion, by applying the boundary conditions and solving for coefficients A_i, we get the following results:

$$A_3 = \frac{ah^2}{2G_{12}}\{E_1[X^2 - (X-1)^2 + (X-2)^2] + E_2[(X-1)^2 - (X-2)^2]\}$$

$$A_4 = \frac{ah^2}{2G_{12}}\{E_1[X^2 - (X-1)^2 + (X-2)^2 - (X-3)^2] + E_2[(X-1)^2 - (X-2)^2 + (X-3)^2]\}$$

And so on. We can already see a pattern beginning to emerge. Tabulating the results for the polynomials that multiply E_1 for increasing values of i, we get the following:

i	Polynomial Expression	Expanded Polynomial
1	X^2	X^2
2	$X^2 - (X-1)^2$	$2X - 1$
3	$X^2 - (X-1)^2 + (X-2)^2$	$X^2 - 2X + 3$
4	$X^2 - (X-1)^2 + (X-2)^2 - (X-3)^2$	$4X - 6$
5	$X^2 - (X-1)^2 + (X-2)^2 - (X-3)^2 + (X-4)^2$	$X^2 - 4X + 10$
6	$X^2 - (X-1)^2 + (X-2)^2 - (X-3)^2 + (X-4)^2 - (X-5)^2$	$6X - 15$
7	$X^2 - (X-1)^2 + (X-2)^2 - (X-3)^2 + (X-4)^2 - (X-5)^2 + (X-6)^2$	$X^2 - 6X + 21$

Now looking at the expanded polynomials, they all match the form $Q_iX^2 + R_iX + S_i$. Tabulating coefficients Q_i, we get

i	Q_i
1	1
2	0
3	1
4	0
5	1
6	0
7	1

The coefficients a_i can be described by the following function of i:

$$Q(i) = \frac{1 + (-1)^{i-1}}{2}$$

Now tabulating the values for R_i, we get

i	R_i
1	$0 = -1 + 1$
2	$2 = 2 + 0$
3	$-2 = -3 + 1$
4	$4 = 4 + 0$
5	$-4 = -5 + 1$
6	$6 = 6 + 0$
7	$-6 = -7 + 1$

Therefore, the coefficients R_i can be described by the following function of i:

$$R(i) = (-1)^i i + \left[\frac{1 + (-1)^{i-1}}{2}\right]$$

Finally, looking at the values of S_i, we get the following table:

i	S_i
1	0
2	-1
3	3
4	-6
5	10
6	-15
7	21

If at first, we only consider the absolute values of S_i and we apply the finite difference method as was done previously, we find that

$$S_{abs}(i) = \frac{i^2}{2} - \frac{i}{2} = \frac{i}{2}(i-1)$$

Now accounting for the alternating negative signs in the values of S_i, we find the following function of i to describe S_i

$$S(i) = (-1)^{i-1}\left[\frac{i}{2}(i-1)\right]$$

Therefore, the polynomial that multiplies E_1 in the values of A_i can be expressed with the following general equation:

$$\left[\frac{1+(-1)^{i-1}}{2}\right]X^2 + \left\{(-1)^i i + \left[\frac{1+(-1)^{i-1}}{2}\right]\right\}X + (-1)^{i-1}\left[\frac{i}{2}(i-1)\right]$$

Following the same procedure for the polynomial that multiplies E_2, we find the following general equation:

$$\left[\frac{1+(-1)^{i}}{2}\right]X^2 - \left\{(-1)^i i + \left[\frac{1+(-1)^{i-1}}{2}\right]\right\}X - (-1)^{i-1}\left[\frac{i}{2}(i-1)\right]$$

Thus, we arrive at the same equation to describe A_i as what was shown in Equation 1.10:

$$A_i(X) = \frac{ah^2}{2G_{12}}\{E_1[Q(i)X^2 + R(i)X + S(i)] + E_2[T(i)X^2 - Q(i)X - R(i)]\}$$

where

$$Q(i) = \frac{1 + (-1)^{i-1}}{2}$$

$$R(i) = (-1)^i i + \left[\frac{1 + (-1)^{i-1}}{2}\right]$$

$$S(i) = (-1)^{i-1}\left[\frac{i}{2}(i-1)\right]$$

$$T(i) = \frac{1 + (-1)^i}{2}$$

The above equation for $A_i(X)$ is valid for $1 \leq i \leq X$. Written another way, coefficients A_i can be expressed as A_{X-j}, where $0 \leq j \leq X - 1$. To find $A_{X-j}(X)$, we start by calculating A_i at $i = X$. Knowing that X will always be an even number, we get the following:

$$A_X = \frac{ah^2}{2G_{12}}\left[E_1\left(\frac{X^2}{2} + \frac{X}{2}\right) + E_2\left(\frac{X^2}{2} - \frac{X}{2}\right)\right]$$

$$A_{X-1} = \frac{ah^2}{2G_{12}}\left[E_1\left(\frac{X^2}{2} + \frac{X}{2} + 1\right) + E_2\left(\frac{X^2}{2} - \frac{X}{2} - 1\right)\right]$$

$$A_{X-2} = \frac{ah^2}{2G_{12}}\left[E_1\left(\frac{X^2}{2} + \frac{X}{2} - 3\right) + E_2\left(\frac{X^2}{2} - \frac{X}{2} + 3\right)\right]$$

$$A_{X-3} = \frac{ah^2}{2G_{12}}\left[E_1\left(\frac{X^2}{2} + \frac{X}{2} + 6\right) + E_2\left(\frac{X^2}{2} - \frac{X}{2} - 6\right)\right]$$

And so on. Once again, a pattern emerges in the polynomials that multiply E_1 and E_2. The first two terms in the polynomials are clearly always the same. The third coefficient in the polynomial multiplying E_1 follows the same pattern as $S(i)$. Therefore, following a similar procedure as what was done for deriving $S(i)$, we can find the following:

$$A_{X-j}(X) = \frac{ah^2}{2G_{12}}\left[E_1\left(\frac{X^2}{2} + \frac{X}{2} + S(j)\right) + E_2\left(\frac{X^2}{2} - \frac{X}{2} - S(j)\right)\right]$$

Where

$$S(j) = (-1)^{j+1}\left[\frac{j}{2}(j+1)\right]$$

Now that we know how to calculate all values of the coefficient A_i of the warping function, the next step is to calculate the coefficients B_i. As per the method presented in [30], the calculation of A_i involves the application of the boundary condition $G_i \frac{\partial g_{oi}}{\partial n} = G_j \frac{\partial g_{oj}}{\partial n}$ from one ply to the next. The B_i coefficient are thus eliminated by the derivative of the warping function. Once the value for A_X (the A_i coefficient of the middle ply) is obtained, subsequent application of the boundary conditions $g_{oi} = g_{oj}$ and $B_{\frac{N}{2}} = B_X = 0$ will lead to the calculation of B_{X-1}, B_{X-2},…B_{X-j}, and so on, until finally B_1 is calculated. Following the method in [30], and understanding that the middle ply will always have longitudinal stiffness E_2, we get the following:

$$g_{oX} = g_{o(X-1)} \; at \; z_X = h$$

$$-\frac{E_2}{G_{12}}\frac{a}{6}{z_X}^3 + A_X z_X = -\frac{E_1}{G_{12}}\frac{a}{6}{z_X}^3 + A_{X-1} z_X + B_{X-1}$$

$$-\frac{E_2}{G_{12}}\frac{a}{6}h^3 + \frac{ah^3}{2G_{12}}\left[E_1\left(\frac{X^2}{2}+\frac{X}{2}\right) + E_2\left(\frac{X^2}{2}-\frac{X}{2}\right)\right]$$

$$= -\frac{E_1}{G_{12}}\frac{a}{6}h^3 + \frac{ah^2}{2G_{12}}\left[E_1\left(\frac{X^2}{2}+\frac{X}{2}+1\right) + E_2\left(\frac{X^2}{2}-\frac{X}{2}-1\right)\right] + B_{X-1}$$

Resulting in

$$B_{X-1} = -\frac{ah^3}{3G_{12}}(E_1 - E_2)$$

Moving on to the next adjacent ply, we have

$$g_{o(X-1)} = g_{o(X-2)} \; at \; z_{X-1} = 2h$$

Once again, substituting variables, we find that

$$B_{X-2} = \frac{7ah^3}{3G_{12}}(E_1 - E_2)$$

And then, if we continue

$$B_{X-3} = -\frac{20ah^3}{3G_{12}}(E_1 - E_2)$$

We see that the only thing that changes is the coefficient that multiplies $\frac{ah^3}{3G_{12}}(E_1 - E_2)$ (let's call the coefficient $U_{X\text{-}j}$). As such, we can define $B_{X-j} = U_{X-j}\frac{ah^3}{3G_{12}}(E_1 - E_2)$. Unfortunately, the finite difference method does not work to be able to define $U_{X\text{-}j}$ as a polynomial function of j. However, if we tabulate the values, we can still see a pattern:

j	$U_{X\text{-}j}$	
1	-1	$= -1^3$
2	7	$= -1^3 + 2^3$
3	-20	$= -1^3 + 2^3 - 3^3$
4	44	$= -1^3 + 2^3 - 3^3 + 4^3$
5	-81	$= -1^3 + 2^3 - 3^3 + 4^3 - 5^3$
6	135	$= -1^3 + 2^3 - 3^3 + 4^3 - 5^3 + 6^3$

We can see the pattern can be defined as follows:

$$U_{X-j} = \sum_{1}^{j}(-1)^j j^3$$

Finally, we arrive to the same equation as what was shown in Equation 1.12

$$B_{X-j} = \left(\sum_{1}^{j}(-1)^j j^3\right)\frac{ah^3}{3G_{12}}(E_1 - E_2)$$

Now that we have a method for calculating the coefficients of the warping function for each layer, we can apply these to the calculation of k using Equation 1.13.